PROTON ANTIPROTON PHYSICS

J. D. Dowell

University of Birmingham, Birmingham, B15 2TT, England.

ABSTRACT

Results from the 1981-1983 operation of the collider at 540 GeV obtained in experiments UA1, UA2, UA3, UA4 and UA5 are presented. After a brief discussion of the accelerator performance and the details of the experimental apparatus the results on elastic and total cross sections are given, as well as those for particle production at low transverse momenta, largely as experimental facts. The main emphasis of the lectures concerns the study of jets and the consequent tests of QCD, the production and decay of the W and Z bosons in comparison with the standard electroweak theory and the observation of a variety of new and intriguing phenomena, some of which suggest physics beyond the standard model. The lectures conclude with a brief review of the future prospects. They rely on material presented at this school by C. Jarlskog, R. Petronzio and D. Haidt concerning Gauge Theories, QCD and their experimental tests, and by J. Iliopoulos on Supersymmetry.

CONTENTS

1. ACCELERATOR PERFORMANCE AND DETAILS OF EXPERIMENTS

The CERN proton-antiproton collider[1] first operated in July 1981 with a centre of mass energy $\sqrt{s}$ = 540 GeV, almost ten times higher than the highest energy, 63 GeV, previously obtained at the CERN Intersecting Storage Rings, and is the first machine to provide sufficient energy to produce the W and Z particles, the carriers of the weak force[2]. So far there have been three data taking periods, each with improved luminosity which reached 1.6×10^{29} $cm^{-2}s^{-1}$ in 1983. The integrated luminosities for each of the periods are:-

Period	$\int Ldt$ (nb^{-1})
Dec. 1981	0.023
Oct. - Dec. 1982	28
Apr. - Jul. 1983	150

The collider operates with 3 proton and 3 antiproton bunches, each 30 cm long and 1 mm high at the collision points, which are stored for 15 - 20 hours at 270 GeV, the energy limit being determined by the power dissipation.

The time between successive bunch crossings, 7.6 μsec, is used to receive data from the detectors and is sufficient to allow a trigger decision to be made whether or not to record the current event on magnetic tape (only a few of the 10^4 events per second can be written). The collider experiments are housed in two underground areas at long straight sections LSS4 and LSS5 and there is also an experiment using a gas jet target.

Experiment	Purpose	Participating Institutions
UA1	General purpose detector (W, Z, jets etc.)	Aachen, Annecy (LAPP), Birmingham, CERN, Harvard, Helsinki, Kiel, Queen Mary College London, NIKHEF Amsterdam, Paris (College de France), Riverside, Roma, Rutherford Appleton Laboratory, Saclay (CEN), Vienna, Wisconsin.
UA2	- ditto -	Bern, CERN, Copenhagen (NBI), Orsay, Pavia, Saclay (CEN).
UA3	Monopole search	Annecy, (LAPP), CERN.
UA4	Elastic scattering and total cross sections	Amsterdam (NIKHEF), CERN, Genova, Napoli, Pisa.
UA5	Streamer chamber (particle production characteristics)	Bonn, Bruxelles, Cambridge, CERN, Stockholm.
UA6	Gas jet target	CERN, Lausanne, Michigan, Rockefeller.

UA6 is a fixed target exeriment designed to compare pp and $p\bar{p}$ reactions[3]. The gas jet may be polarised. As the experiment has not yet run it will not be discussed further.

The highest luminosity is achieved with "low β" quadrupoles energized in order to focus the beam strongly to give the smallest possible size. This is not ideal for elastic scattering studies which require a low angular spread and therefore "high β". As the product of angular divergence times beam size is conserved (Liouville's theorem), in each plane, this implies low luminosity. Consequently there is an element of incompatibiilty between elastic scattering studies and W, Z physics. In addition to UA4, UA1 is equipped to study elastic scattering. Details of the various experiments are summarised in the following paragraphs, also in Figures 1 - 9 and Tables 1 - 3.

Throughout these lectures θ is defined as the polar angle of a particle with respect to the beam direction and φ the azimuthal angle around the beam. The rapidity of a particle is defined as

$$y = \tfrac{1}{2} \ln \frac{E + p_l}{E - p_l}$$

where E is the particle energy and p_l its longitudinal momentum. It can be approximated by the "pseudo-rapidity" η given by

$$\eta = -\ln \tan \theta/2$$

Intervals of rapidity or pseudo-rapidity are Lorentz invariant which is convenient in

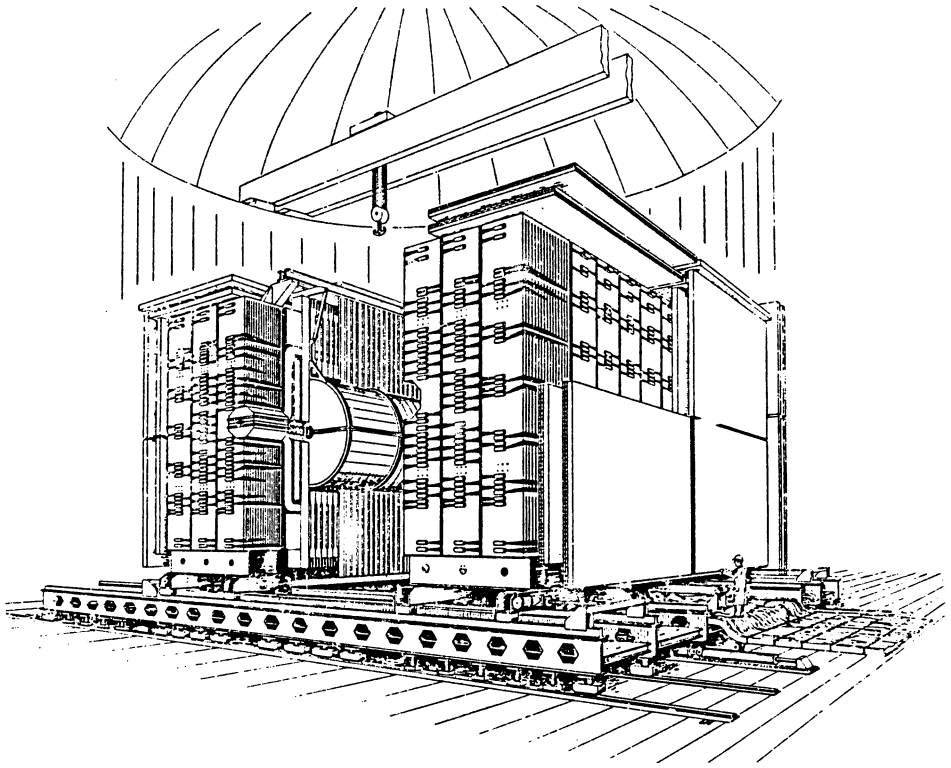

Figure 1 A general view of the UA1 detector

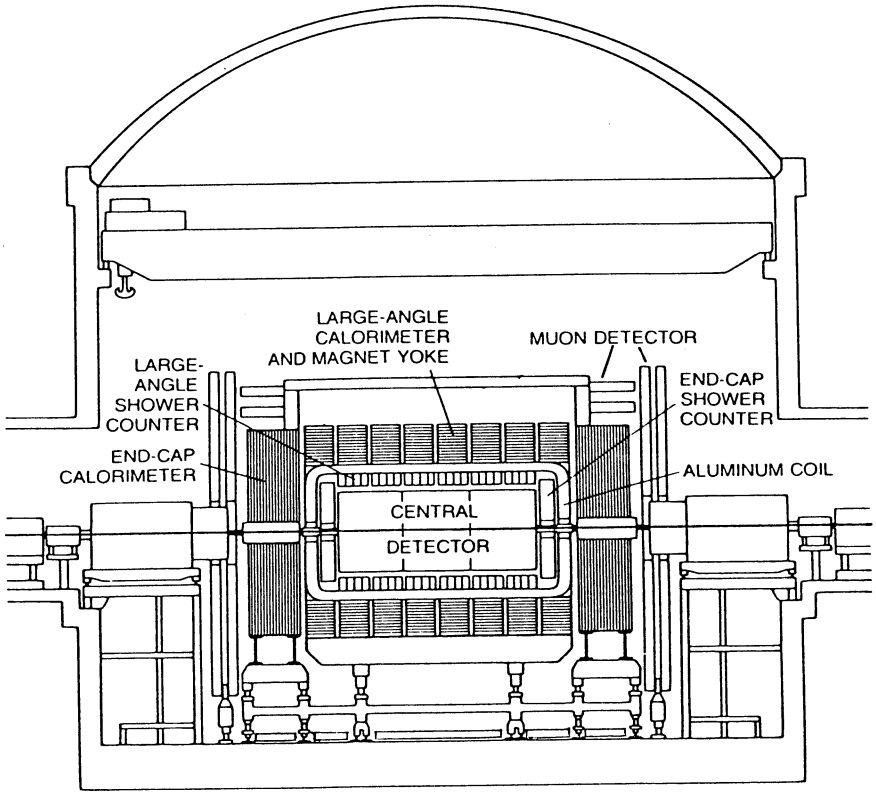

Figure 2 A side view of the UA1 detector.

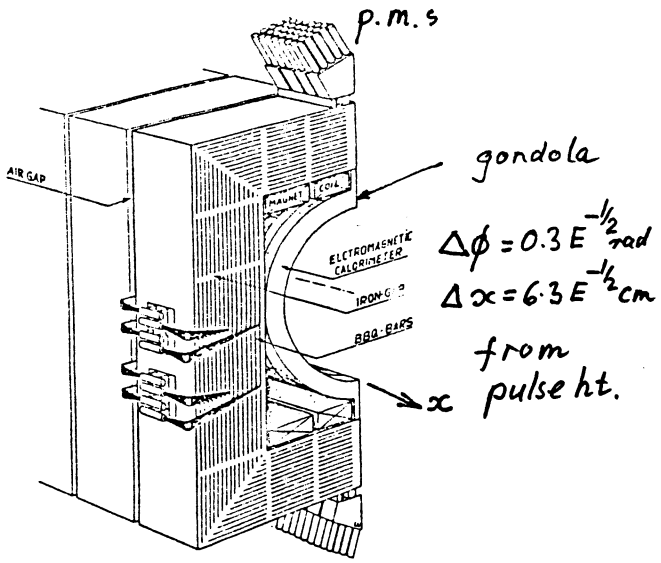

Figure 3 Arrangement of the large angle calorimeters in UA1 showing the 'gondolas' and 'Cs'.

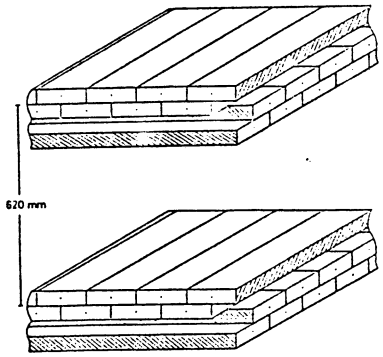

Figure 4 Layout of the muon drift tubes in UA1.

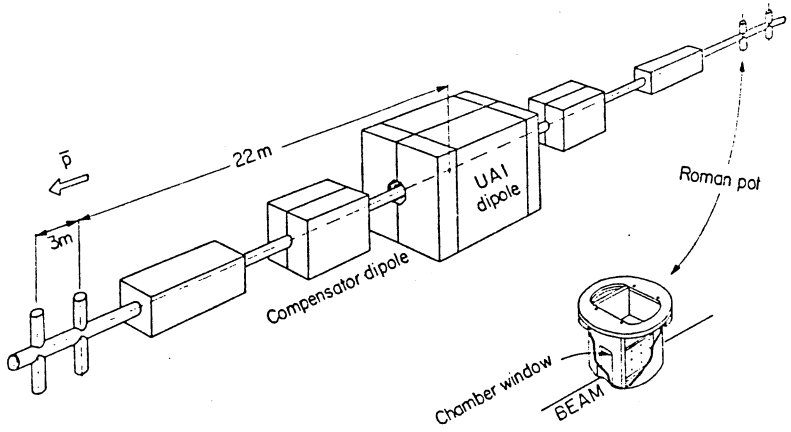

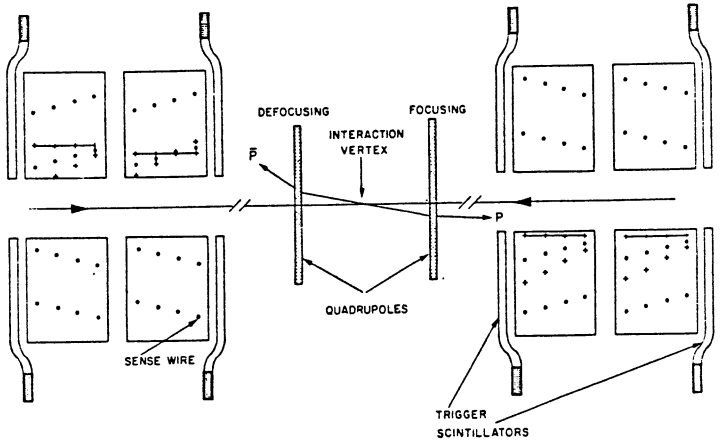

Figure 5 The elastic scattering detectors in UA1. The Roman pots house the drift chambers shown in the lower half of the figure which contain a typical event.

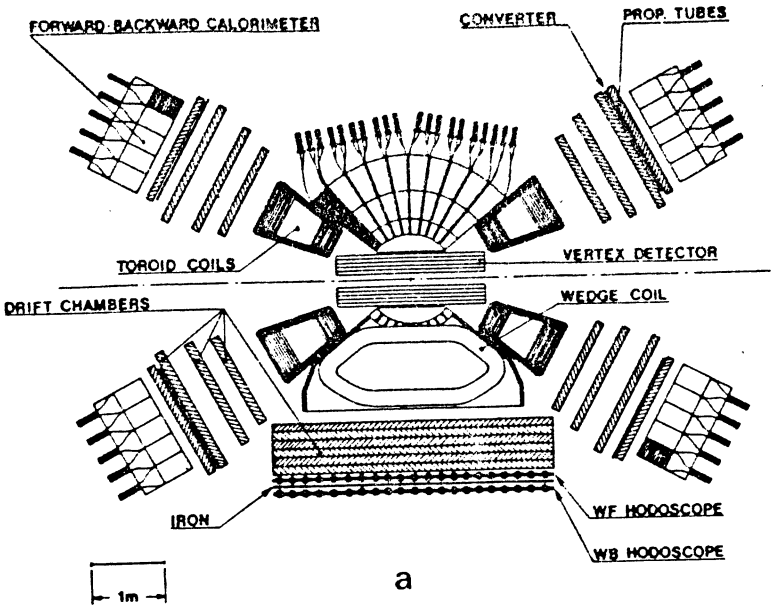

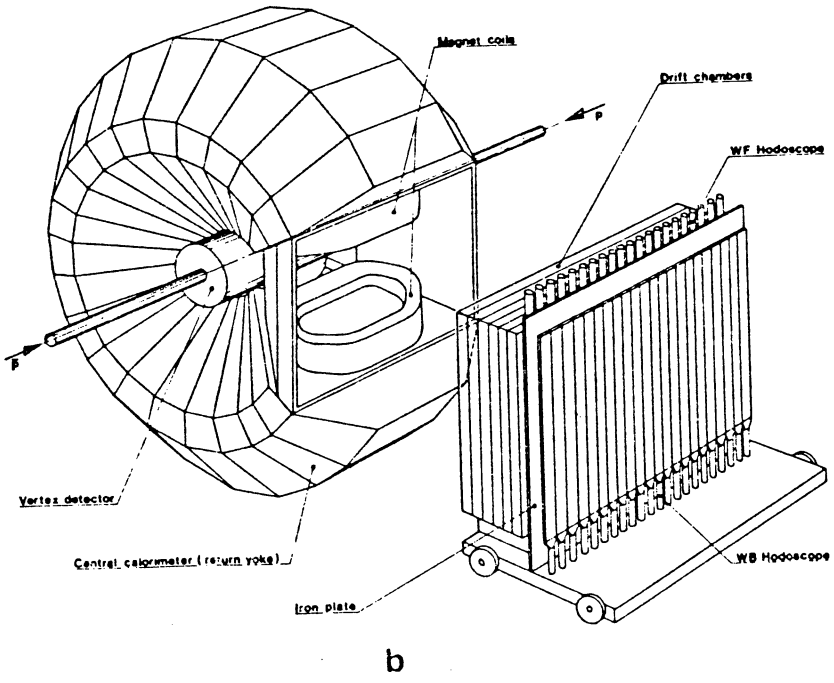

Figure 6 The UA2 detector a) a plan showing the side detector in place b) the central calorimeter and the side detector. The wedge aperture was closed for the 1983 run.

Table 1

Type	Drift chamber with charge division readout of the second coordinate
Gas mixture	Argon (40%) + ethane (60%)
Drift field and gap length	1.5 kV/cm, 18 cm
Drift velocity	5.3 cm/μs
Drift angle	23° at $\|B\|$ = 0.7 T
Anode plane arrangement:	
a) Distance between sense wires	10 mm
b) Wire length	80 cm min., 220 cm max.
c) Sense wire charac.	35 m Ni-Cr stretched at 80 g
d) Field wire charac.	100 μm gold-plated Cu-Be stretched at 200 g
Cathode plane structure:	
a) Distance between wires	5 mm
b) Wire characteristics	150 μm gold-plated Cu-Be stretched at 200 g
Total number of wires	22800
Total number of sense wires	6110

Table 2

Calorimeter		Angular coverages	Thickness: No. rad. lengths	Thickness: No. abs. lengths	Cell Size: Δθ (°)	Cell Size: Δφ (°)	Sampling step	Segmentation in depth	Resolution
Barrel	e.m.: gondolas	25-155	$26.6/\sin\theta$	$1.1/\sin\theta$	5	180	1.2 mm Pb 1.5 mm scint.	3.3/6.6/10.1/6.6 X_o	$0.15/\sqrt{E}$
	hadr.: C's		-	$5.0/\sin\theta$	15	18	50 mm Fe 10 mm scint.	2.5/2.5 λ	$0.8/\sqrt{E}$
End-caps	e.m.: bouchons	5-25 and 155-175	$27/\cos\theta$	$1.1/\cos\theta$	20	11	4 mm Pb 6 mm scint.	4/7/9/7 X_o	$0.12/\sqrt{E_T}$
	hadr.: I's		-	$7.1/\cos\theta$	5	10	50 mm Fe 10 mm scint.	3.5/3.3 λ	$0.8/\sqrt{E}$
Calcom	e.m.	0.7-5 and 175-179.3	30	1.2	4	45	3 mm Pb 3 mm scint.	4 x 7.5 X_o	$0.15/\sqrt{E}$
	hadr.		-	10.2	4	45	40 mm Fe 8 mm scint.	6 x 1.7 λ	$0.8/\sqrt{E}$
Very forward	e.m.	0.2-0.7 and 179.3-179.8	24.5	1.0	0.5	90	3 mm Pb 6 mm scint.	5.7/5.3/5.8/7.7 X_o	$0.15/\sqrt{E}$
	hadr.		-	5.7	0.5	90	40 mm Fe 10 mm scint.	5 x 1.25 λ	$0.8/\sqrt{E}$

UA1: angular coverage, segmentation and resolution of calorimeters.

Table 3

Main parameters of the UA2 detector

I. SOLID ANGLE COVERAGE

Central region. Electron-hadron calorimetry.

$\Delta y = 2$, $\Delta\theta = 100^o$, $\Delta\phi = 300^o$

Forward-backward regions. Electron calorimetry and magnetic spectroscopy.

$\Delta y = 1.5$, $\Delta\theta = 35^o$, $\Delta\phi = 82\%$ of 360^o

Wedge region. electron calorimetry and magnetic spectroscopy.

$\Delta y = 1.3$, $\Delta\theta = 68^o$, $\Delta\phi = 28^o$

II. CENTRAL CALORIMETER

200 cells, each covering $\Delta\theta \times \Delta\phi = 10^o \times 15^o$.

Longitudinal segmentation

17 r.l. (lead-scintillator) + 2 x 2 abs. l. (iron-scintillator)

Electron calorimetry 26 x 3.5 mm lead plates
27 x 4 mm NE 104 scintillator plates

Hadron calorimetry (18 + 22) x 15 mm iron plates
(18 + 22) x 5 mm scintillator plates
(PMMA, 10% naphtalene, 1% PBD, 0.01% POPOP)

Light guides: 2 mm lucite, 80 mg/l BBQ

Photobus: 7 per cell, XP2012 for electron calorimetry and XP2008 for hadron calorimetry

III. FORWARD DETECTORS

24 identical sectors each covering $\Delta\theta \times \Delta\phi = 17.5^o \times 25^o$

Field integral 0.38 Tm.

9 drift chambers per sector

- wire orientation with respect to field: -7^o, 0^o, $+7^o$
- drift cell width 15 cm
- field shaping wires every 5 mm
- total number of signal wires 2304

Table 3 (continued)

preshower counter

- preconverter 1.4 r.l. lead + iron
- 4 tube planes (brass) 20 mm O.D., 0.3 mm thick
- tube orientation with respect to field: 0^o, 0^o, 77^o, 77^o
- anode 30 micron gold plated tungsten

forward calorimeters

- 10 cells per sector, each covering $\Delta\theta \times \Delta\phi = 4^o \times 15^o$
- cell transverse sizes 27 x 33 to 27 x 60 cm^2
- longitudinal segmentation: 33 x (4 mm lead + 4 mm Altustipe 10105) + 8 x (4 mm lead + 4 mm Altustipe 10105) = 24 + 6 r.l.
- light guides and phototubes as in central calorimeters

IV. VERTEX DETECTOR

- five proportional chambers with cathode strip read-out one of which is located behind a 1.5 r.l. tungsten converter.
  number of strips 480, 480, 528, 672 and 480.
  number of wires 288, 384, 576, 864 and 576.
  chamber radii 100, 124, 236, 315 and 355 mm.
  chamber lengths 104, 110, 150, 178 and 80 cm.
  wire pitch 2.2, 2.0, 2.6, 2.3 and 3.9 mm.
  strip angle $\tan\alpha = \pm 0.9, 1.3, 1.0, 1.0, 1.0$.
  half gap 4 mm.
  strip pitch = 4 mm.
- two drift chambers of 24 azimuthal cells each, 6 sense wires/cell (charge division, multihit capability), sense wire lengths 1520 and 1785 mm.
- 24 scintillator plates.

comparisons with cosmic ray data where the energy of the primary parent particle is not known. Another quantity commonly used is transverse energy defined as

$$E_T = E_i \sin\theta_i$$

where E_i is the energy of a particular particle and θ_i its polar angle. It is relevant where calorimeters are used which measure energy. In the case of jets, local sums of calorimeter energy may be used

$$E_T = \sum_i E_i \sin \theta_i$$

where the sum is over calorimeter elements contributing to an energy cluster. Furthermore, one can define the total transverse energy of an event as the sum of all transverse energy depositions.

The UA1 detector[4] (figures 1 - 5) was designed as a general purpose instrument with an almost 4π solid angle coverage extending down to polar angles of a few mrad. Its central part is a 6 m long, 2.4 m diameter drift chamber system with 18 cm drift spaces. The image readout gives space points at centimetre intervals along the tracks and records ionization information. The central track detector is surrounded along its length by 48 semicylindrical electromagnetic calorimeters and at each end by 32 similar radial sectors. All of the above are inside the coil of a dipole magnet (7 m x 3.5 m x 3.5 m) which produces a highly uniform field of 0.7T. The laminated return yoke of the magnet, equipped with scintillation counters, also serves as a hadron calorimeter. The outer shell of the detector is a large-area muon detector consisting of 8 layers of drift tubes (2 separated chambers each with 4 layers). Calorimeterized compensator magnets, small angle calorimeters and further track detectors extend the detection to angles less than 5^o. The measured rms accuracy of the central drift chambers is 290 μm giving a momentum resolution $\frac{\Delta p}{p} \sim 0.005\ p$ for a 1 m track perpendicular to the field. The electromagnetic and hadron calorimeters have energy resolutions of $\frac{\Delta E}{E} \sim 0.15/\sqrt{E}$ and $\sim 0.8\sqrt{E}$ respectively. An independent means of measuring the luminosity is provided by small drift chambers at ± 22 m to measure elastic scattering by detecting collinear particles.

The UA2 detector[5] (figure 6), more specifically matched to the $W^{\pm}$, Z^o search, is composed of finely segmented calorimeter cells, 240 in the central region and 240 in the forward and backward cones. They are arranged in tower structures pointing at the intersection region. An inner detector, using drift and proportional chambers, determines the vertex position. The forward and backward detectors include magnetic spectrometers (toroidal magnets and drift chambers) to measure the asymmetry of the electrons from $W^{\pm}$ decays. For the 1981 and 1982 runs a 60^o azimuthal wedge of the central calorimeter was replaced by a magnetic spectrometer covering ± 0.7 units of rapidity which used drift chambers, time of flight counters and a lead-glass array, outside the main apparatus, to identify charged particles and neutral pions.

Experiment UA3[6] shares the same intersection region as UA1 and is a search for magnetic monopoles by looking for their expected ionization in 125 μm thick kapton foils. These are placed both inside the vacuum chamber near the intersection point and around the

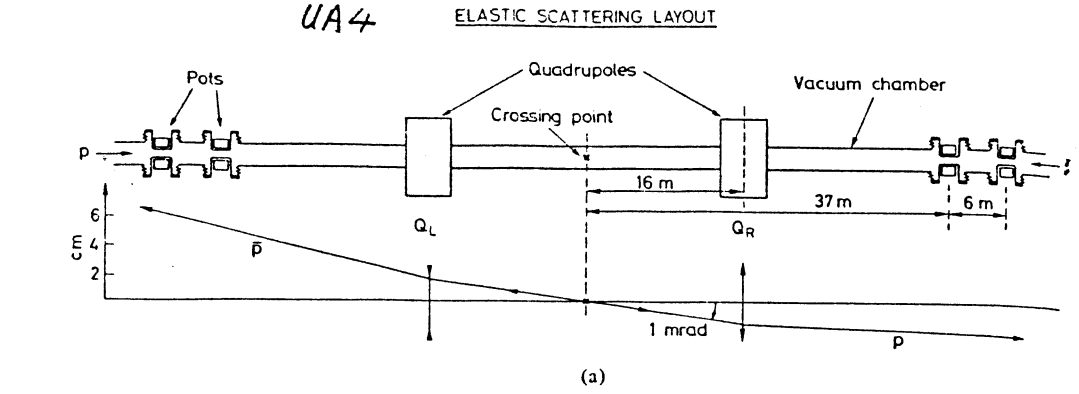

(a)

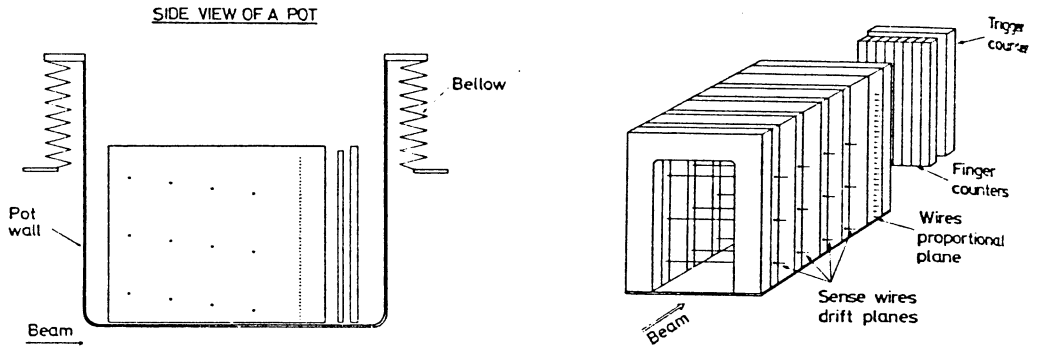

(b) (c)

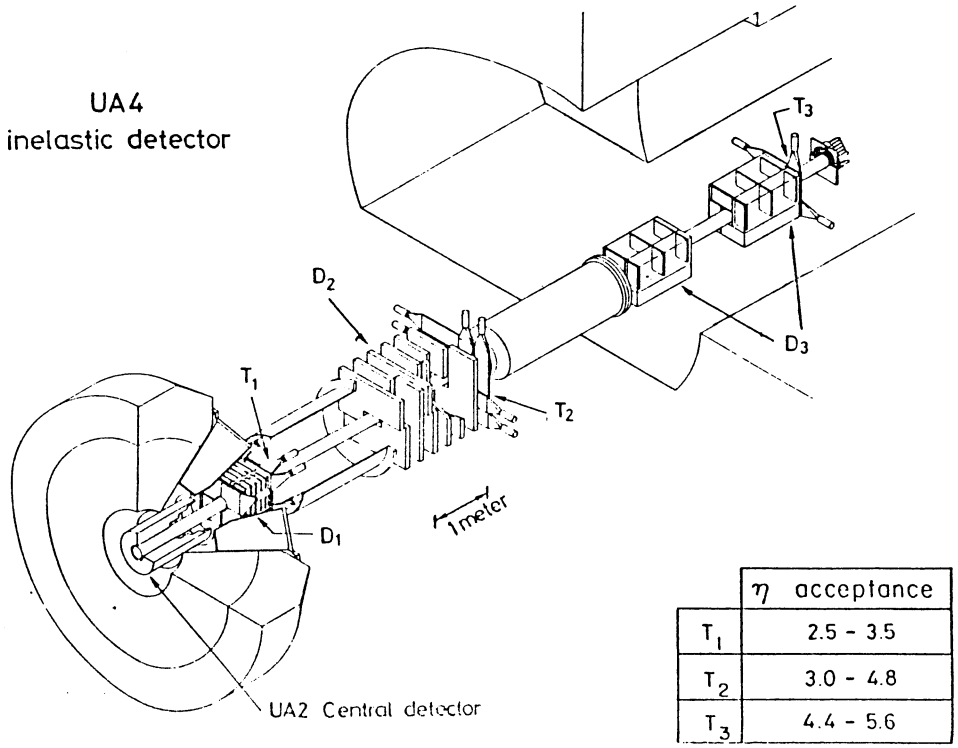

	η acceptance
T_1	2.5 - 3.5
T_2	3.0 - 4.8
T_3	4.4 - 5.6

Figure 7 The UA4 elastic scattering and total cross section experiment a) general layout b) Roman pot c) details of drift chambers d) inelastic detector showing the UA2 calorimeter.

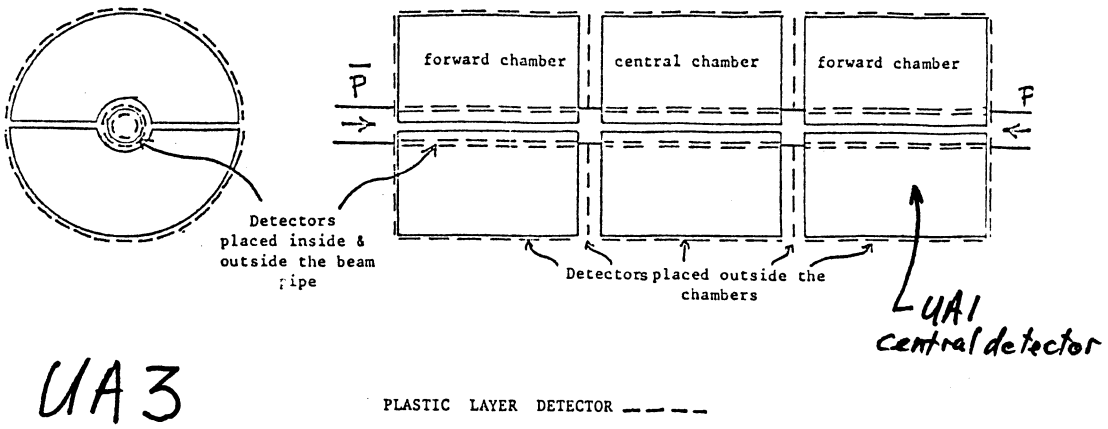

Figure 8 The UA3 magnetic monopole experiment.

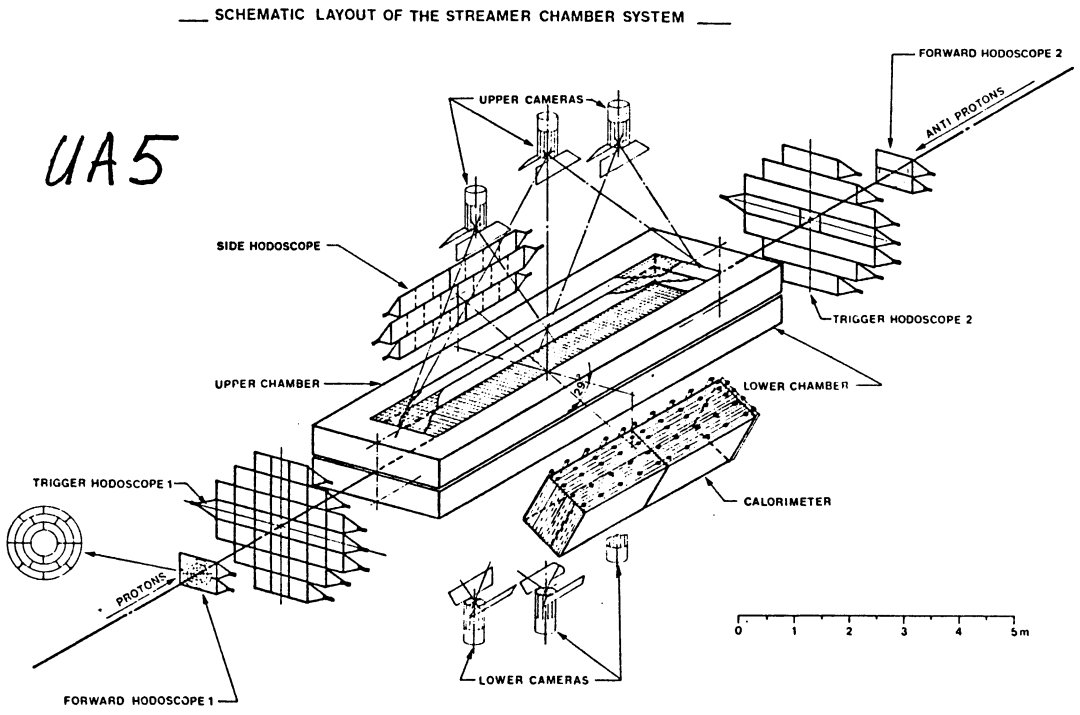

Figure 9 The UA5 streamer chamber experiment.

outside of the UA1 central track detector. The foils have been scanned but no evidence for monopoles has yet been observed[6]. The specific ionization of a monopole is related to that of the specific ionization of a minimum ionizing particle by

$$(dE/dx)_{mono}/(dE/dx)_{min.ion} = \beta^2(g^2/e^2)$$

where β is the monopole velocity and g the magnetic charge. For Dirac monopoles $(g^2/e^2) \sim 5 \times 10^3$. The experimental threshold is $\sim 2 \times 10^3$ minimum ionization.

Experiment UA4[7] coexists with UA2 (figure 7). It measures elastic and inelastic scattering and (using the optical theorem) the $p\bar{p}$ total cross section. Small drift and proportional chambers can be placed very near to the beams inside "Roman pots" situated 20 m and 40 m on either side of the intersection point. Smaller angles of scattering can be detected than in UA1.

The main part of the UA5 detector[8] consists of two 6 m long streamer chambers above and below the intersection region incorporating lead-glass plates to allow photon detection. There is no magnetic field and the experiment is an alternative to UA2. It is designed to study simple characteristics of particle production. (See figure 8). A 90° hadron calorimeter has been added for triggering on high p_t processes but not yet used.

As data acquisition rates are limited some form of triggering is needed to select events of interest. Up to now, three types of trigger have been used to study inelastic events: a) simple hodoscopes at each end of the detector (UA1, UA2, UA5) giving a 'minimum bias' trigger; b) transverse energy triggers (UA1, UA2) where $E_T = \sum E_i \sin\theta_i$ is summed over electromagnetic and hadronic calorimeter cells and a threshold is imposed to select high p_t processes (for example a high p_t electron from W decay would give a localised electromagnetic deposition); c) muon triggers (UA1).

It is worth commenting on the relative merits of the UA1 and UA2 detectors. The strong features of UA1 are the magnetic field and central track detector which make it a good general purpose instrument. Furthermore its calorimeters extend to very forward angles (0.2°) giving excellent sensitivity to missing transverse energy (neutrinos). On the other hand, the electromagnetic calorimeters cells are not segmented in ϕ in the barrel region (gondolas) or in θ in the end-cap regions (bouchons) which can cause problems if more than one particle strikes a cell. UA2 has better calorimeter granularity and position detection for electromagnetic showers which compensate to some extent for the absence of a magnetic field in recognising electrons (see later) but has less complete angular coverage which is bad for missing E_T. There is also only one depth segmentation in the UA2 electromagnetic calorimeters compared to four in UA1.

Calibration of the electromagnetic calorimeters is essential for W and Z mass determinations. UA1 uses an intense (7 Ci) Co^{60} source to map the calorimeters which is normalised to test beam measurements on a single element. A pulsed laser is used to monitor the photomultiplier gains. UA2 can put all cells in a beam and uses a Co^{60} source and photodiodes for local monitoring.

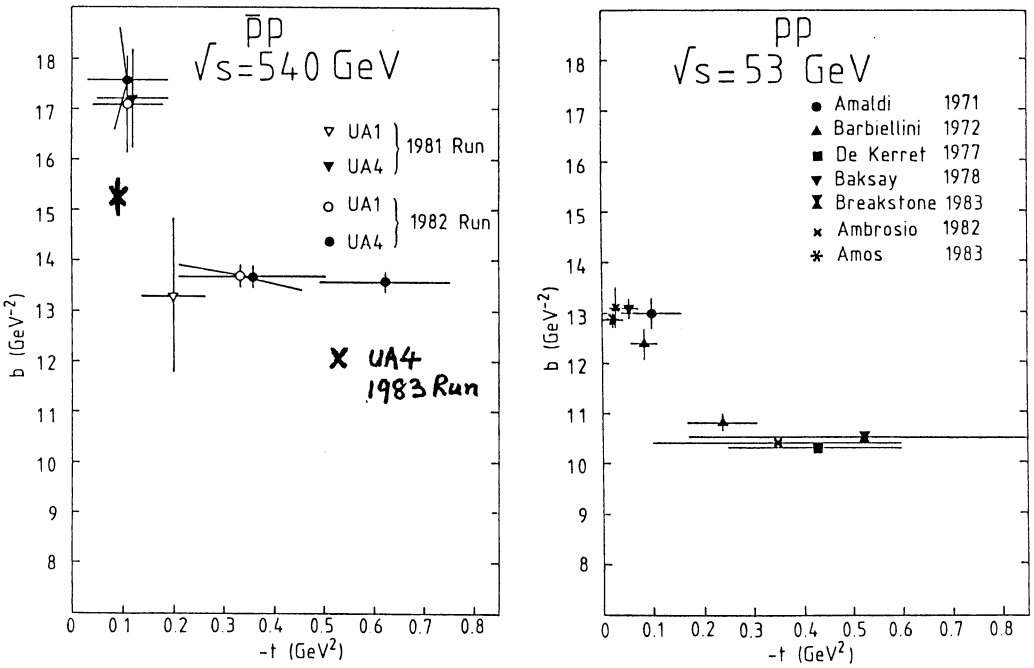

Figure 10 The elastic scattering slope parameter b at $\sqrt{s}$ = 540 GeV and $\sqrt{s}$ = 53 GeV (pp collisions), when $d\sigma/dt$ is parametrised as e^{bt}.

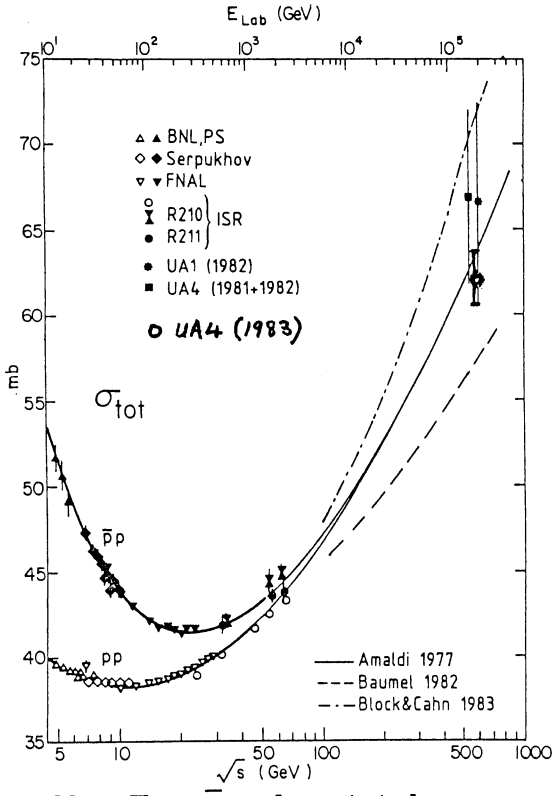

Figure 11. The $p\bar{p}$ and pp total cross section. The curves are fits up to ISR energies [12, 13, 14]. The solid curve[12] has an $(\ln s)^2$ dependence.

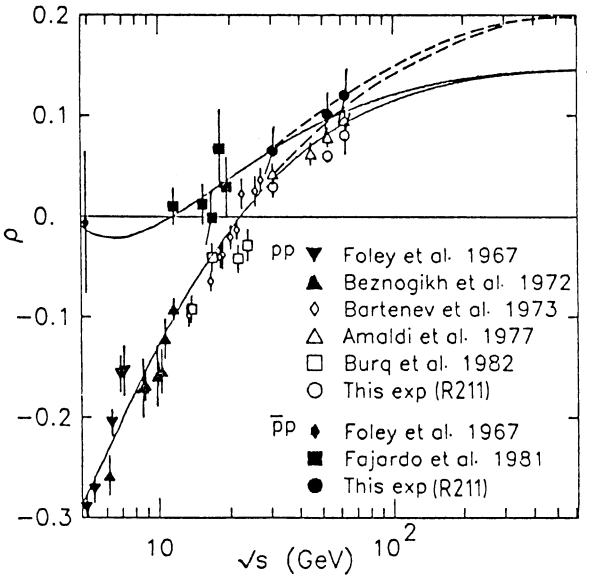

Figure 12. ρ, the ratio of the real part to the imaginary part of the forward amplitude for pp and $p\bar{p}$ elastic scattering. The curves are dispersion relation fits by Amaldi et al[12] (solid curves) and Block et al[13].

2. ELASTIC SCATTERING AND TOTAL CROSS SECTION

W and Z production account for only about 10^{-7} of the total cross section. Even QCD processes producing high p_t ($>$ 20 GeV/c) jets are only a fraction of a percent. The majority of what happens therefore comes under the heading of total cross section, particle production etc., discussed in the next three sections. If one is designing an experiment, say for a 20 TeV collider, one needs a way of extrapolating these things to higher energies in order to judge what detectors will be required to handle the events. Furthermore, one hopes that what is called "soft" physics may ultimately be described by QCD which would therefore have to explain the details. Finally, there is always the prospect of some anomalous behaviour pointing to new phenomena even at low p_t. However, in the absence of any precise theory of low p_t process, I am presenting only the data and refer the reader to published work for theoretical attempts to explain the results.

$\bar{p}p$ elastic scattering has been measured by UA1[9] and UA4[10] in the 1981 and 1982 running periods. Good agreement for the slope b of the differential cross section,

parametrised as $\frac{d\sigma}{dt}(t) = \frac{d\sigma}{dt}(0)\, e^{bt}$, were obtained for $|t|$ values up to 0.8 $(GeV/c)^2$ showing a change of slope near $|t| = 0.15$ $(GeV/c)^2$ (Figure 10) similar to that observed at the ISR ($\sqrt{s}$ = 63 GeV). Improved measurements by UA4 in 1983[11], however, give a smaller value of the low t slope (15.3 ± 0.3 $(GeV/c)^{-2}$ compared to 17.3 ± 0.6 $(GeV/c)^{-2}$). Using this smaller value gives a slope change Δb of 1.6 ± 0.4 $(GeV/c)^{-2}$ compared to 2.7 ± 0.4 $(GeV/c)^{-2}$ at 63 GeV, where Δb is the difference in slope between $-t = 0.1$ $(GeV/c)^2$ and $-t = 0.3$ $(GeV/c)^2$. This necessarily affects the value obtained for the total cross section which requires an extrapolation to t = 0.

The total cross section σ_t is obtained using the optical theorem

$$(\mathrm{Im}\ f(0))^2 = \frac{\sigma_t^2}{16\pi(hc)^2}$$

where f(0) is the forward elastic scattering amplitude. The differential elastic event rate can be written

$$\frac{dn_{el}}{dt} = L\,\frac{\sigma_t^2(1+\rho^2)}{16\pi(hc)^2}\, e^{bt}$$

where ρ is ratio of the real to imaginary parts of f(0) and L the luminosity. Furthermore

$$N_{el} + N_{inel} = L\,\sigma_t$$

where N_{el} and N_{inel} are the total elastic and inelastic event rates.

Combining the two expressions and extrapolating $\frac{dN_{el}}{dt}$ to t = 0 allows σ_t to be calculated (the extrapolation can allow an arbitrary form for the shape of the elastic differential cross section at small t which we have written as e^{bt} for simplicity). This is the method

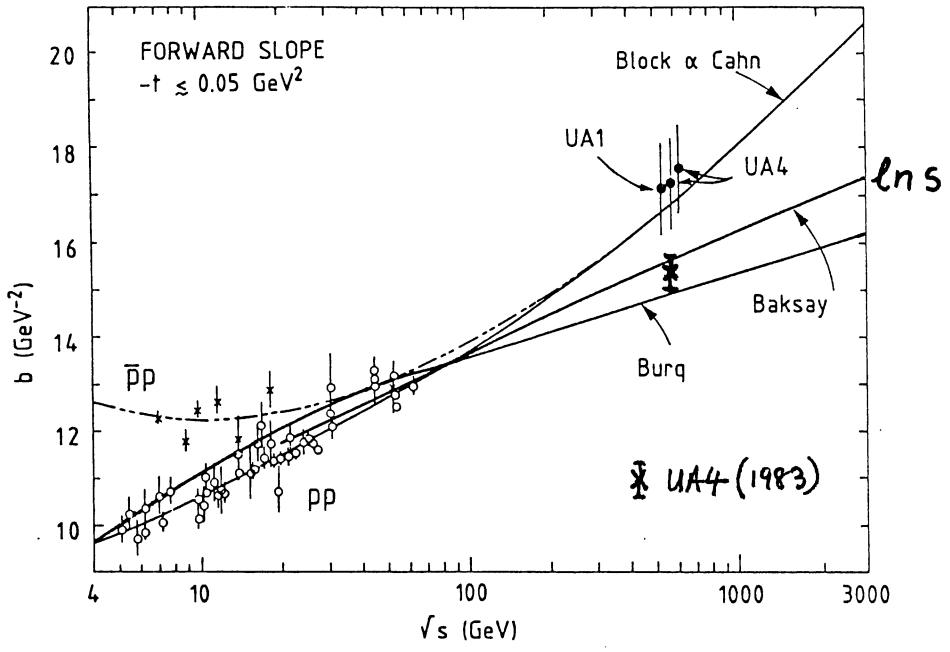

Figure 13 The forward slope parameter b for $\bar{p}p$ and pp elastic scattering. The curves are fits up to ISR energies[13, 15, 16].

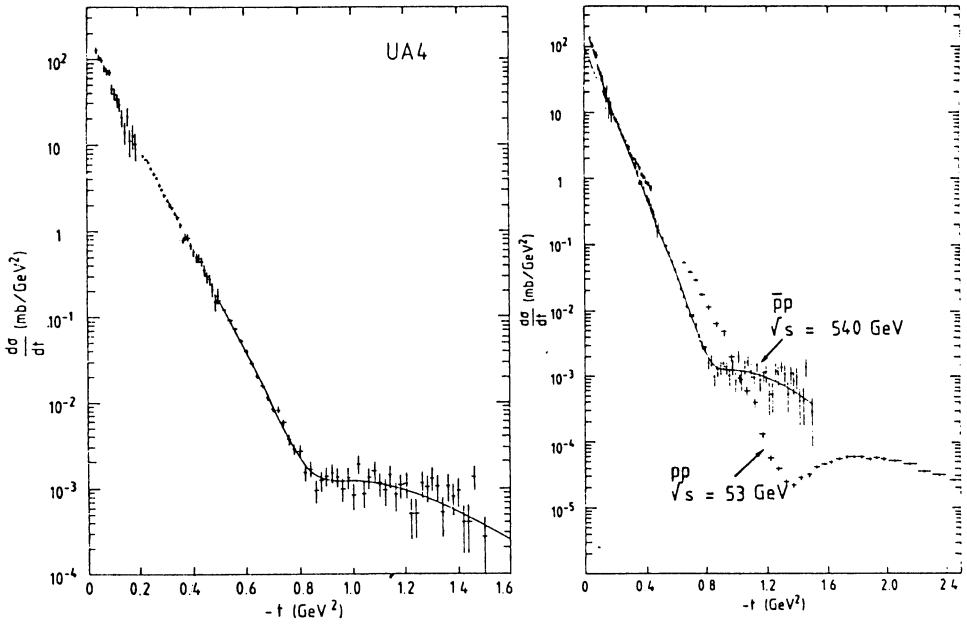

Figure 14 a) Differential cross section for $\bar{p}p$ elastic scattering measured by UA4. The curve is a fit with two interfering exponential amplitudes.
b) A comparison between collider data and ISR data at $\sqrt{s}$ = 53 GeV.

used by UA4 who measure $\frac{dN_{el}}{dt}$, N_{el}, N_{inel} yielding $(1+\rho^2)\sigma_t$. UA1 measure only $\frac{dN_{el}}{dt}$, N_{el} and require a separate measurement of the luminosity (provided by wire scanners in LSS2 diametrically opposite to LSS5, with an error of ± 8%) which leads to a determination of $(1+\rho^2)^{1/2}\,\sigma_t$. The 1982 measurements of the two experiments with low statistics were in excellent agreement (figure 11) giving an average value of 67 ± 5 mb. The 1983 UA4 result is 61.9 ± 1.5 mb at 546 GeV, somewhat lower but statistically compatible (figure 11). In all cases a value of 0.15 has been assumed for ρ as suggested by a dispersion relation fit to lower energy measurements (figure 12) by Amaldi et al[12]. Both the old and new results are compatible with a $(\ln s)^2$ dependence of σ_t and agree well with a dispersion relation extrapolation[12]. The energy variation of the forward elastic slope (and as a consequence of the total elastic cross section) is more controversial, the old results favouring a $(\ln s)^2$ dependence and the new UA4 result an $\ln s$ dependence (figure 13). This is important in assessing whether an asymptotic situation has been reached[17]. The Froissart bound[18] forbids the total cross section to rise faster than $(\ln s)^2$. If the bound is qualitatively saturated then asymptotically $\frac{\sigma_{el}}{\sigma_t}$ should tend to a constant which also means $\frac{b}{\sigma_t} \to$ constant. The new UA4 data indicate a significant change in $\frac{\sigma_{el}}{\sigma_t}$ from 0.185 ± 0.005 at the ISR to 0.215 ± 0.005 at the collider, a change of (16 ± 4)%.

The tentative conclusion is that asymptopia has not yet been reached. In geometrical terms the proton is becoming <u>bigger</u> and <u>blacker</u> (more opaque). A totally black proton would have $\frac{\sigma_{el}}{\sigma_t} = 1/2$.

UA4 have also made elastic measurements at larger $|t|$ which have revealed a shoulder at $|t| = 0.8$ (GeV/c)^2 which is presumably related to the dip at 1.2 (GeV/c)^2 observed at 53 GeV (figure 14). An empirical fit of the expression

$$\frac{d\sigma}{dt} = \left| e^{b_1(t-t_o)/2} + e^{b_2(t-t_o)/2} + i\phi \right|^2$$

gives $b_1 = 10.9 \pm 1.1$ (GeV/c)$^{-2}$

$b_2 = 4.6 \pm 1.1$ (GeV/c)$^{-2}$

$t_o = 0.81 \pm 0.01$ (GeV/c)

$\phi - \pi = -0.39 \pm 0.16$ rad.

$\phi = \pi$ would give a dip at $t = t_o$ (destructive interference).

Several authors[17,19] have described models to explain the elastic scattering but none is particularly successful in explaining all the features. They will not be discussed here.

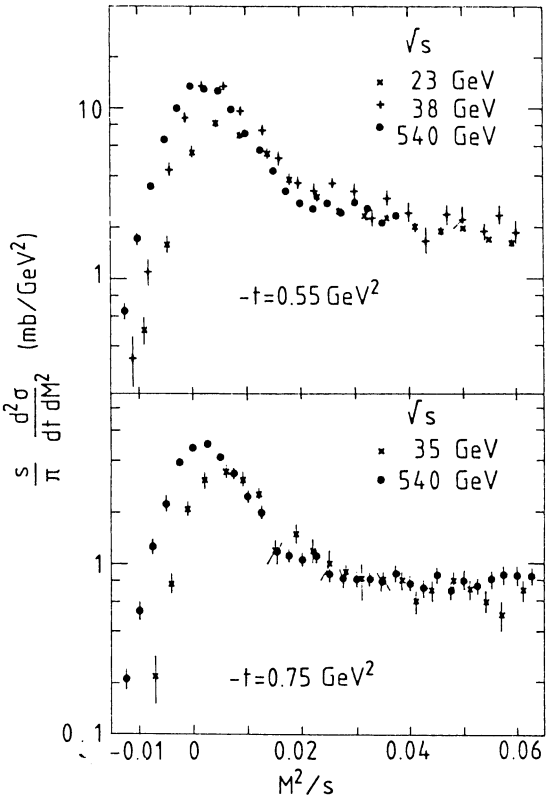

Figure 15. The invariant cross section for pp → pX at the collider plotted versus M^2/s, where M is the mass of the diffractive system X, for two different t-values. ISR data are shown and exhibit scaling for larger values of M^2/s.

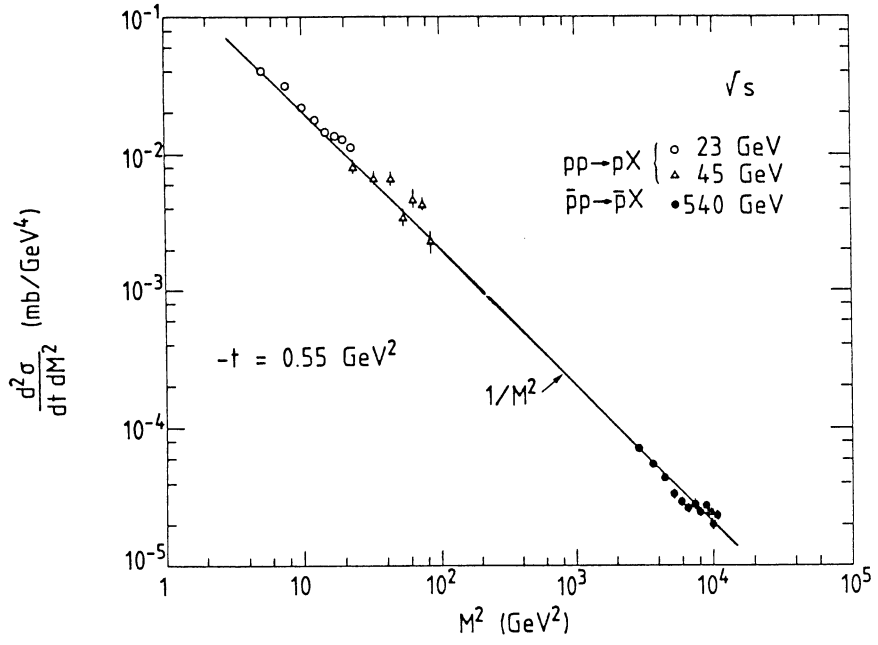

Figure 16 Data on the non-invariant cross section $d^2\sigma/dtdM^2$ at various energies and fixed t, in the interval $0.01 < M^2/s < 0.04$, plotted versus M^2.

3. SINGLE DIFFRACTION DISSOCIATION ($\bar{p}p \to \bar{p}X$)

UA4 have studied single diffraction dissociation[20] in which one of the colliding particles fragments but the other remains intact. The technique is to detect the scattered $\bar{p}$ (or p) and measure its momentum p and angle θ. This allows the four momentum transfer and the mass of the recoiling system to be calculated.

$$-t = m_p^2(1-x)^2/x + 2xp_o^2(1-\cos\theta)$$

$$M^2 = (1-x)s$$

where p_o is the incoming momentum and $x = p/p_o$. p is measured from the bending in an SPS quadrupole to a precision of about 0.6%. Consequently $\Delta(\frac{M^2}{s}) = x\ \frac{\Delta p}{p}$ is $\sim \cdot 006$.

The main results are (figures 15 and 16)

i) Scaling of the invariant cross section $\frac{s\, d^2\sigma}{dtdM^2}$ at fixed t with the results obtained at the ISR[21] to about 20%, apart from a kinematic effect at low M^2/s which is due to the fact that the minimum mass that can be produced is independent of s,

ii) a $1/M^2$ behaviour for $\frac{d^2\sigma}{dtdM^2}$ at fixed t.

Both of these results are expected in a Regge picture with Pomeron exchange.

$$\frac{d^2\sigma}{dtdM^2} = f(t)\ (\frac{s}{M^2})^{2(\alpha_p(t)-1)}\ \frac{1}{M^2}\ \sigma_{p_p}\ (M^2,t)$$

where f(t) is a function of t and σ_{p_p} is the Pomeron-proton cross section which should be constant for large M^2. $\alpha_p(t)$ is the Pomeron Regge trajectory.

Summarising the main results on total cross sections, elastic and single diffractive scattering at 540 GeV we have:-

i) σ_t is compatible with an $(\ln s)^2$ increase with s

ii) the elastic slope parameter b (where $\frac{d\sigma}{dt} \propto e^{bt}$) increases as $\ln s$

iii) the above results mean that σ_{el}/σ_t is varying with energy and is $(16 \pm 4)\%$ larger than at 53 GeV.

iv) therefore we are not yet in an asymptotic regime

v) single diffractive production of large masses ($\sim$100 GeV/c^2) is observed which scales with ISR results to $\sim$20%.

4. PARTICLE PRODUCTION (MINIMUM BIAS PHYSICS)

4.1 Pseudo-rapidity density distribution

The study of particle production (multiplicity, p_t spectrum etc.) would ideally be unbiassed, including all types of events. In practice it is necessary to apply a trigger to signify that an event has occured. It is easy to trigger from inelastic events in which both colliding particles fragment because they will generally throw particles into

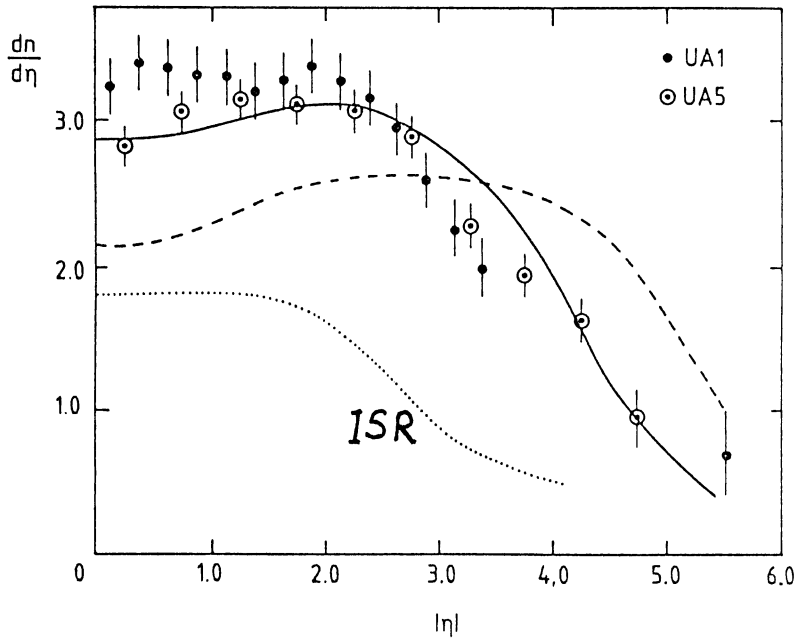

Figure 17 The pseudo-rapidity density for non-single diffractive inelastic events observed by UA1 and UA5. The dashed curve is the expectation based on cylindrical phase space for $< p_t > = 0.35$ GeV/c. The solid curve is for $< p_t > = 0.5$ GeV/c. The shape of the ISR data is shown for comparison.

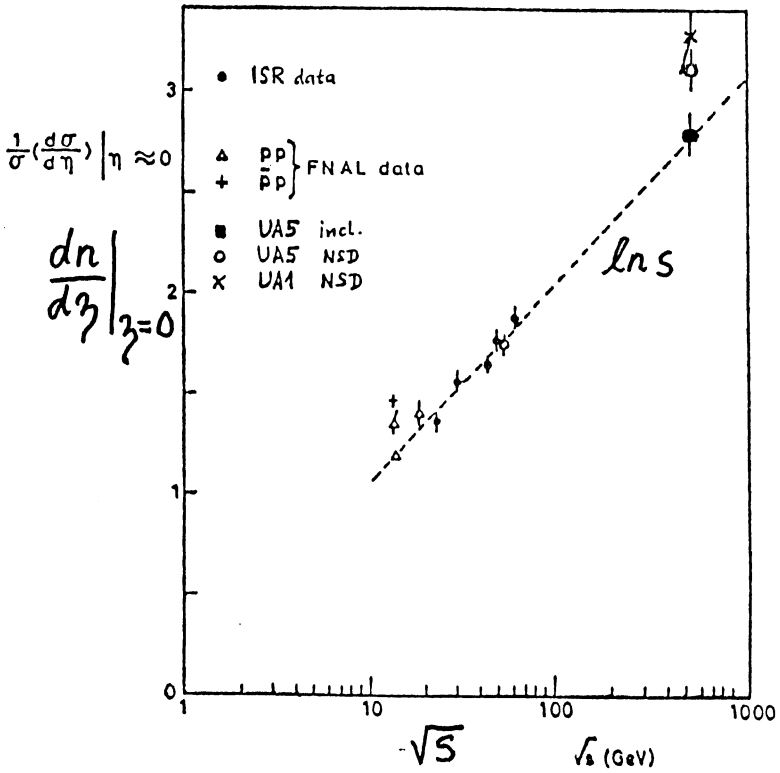

Figure 18 The central rapidity plateau height showing the ln s dependence. Note the difference between the plateau heights for inclusive and non single diffractive events.

the triggering hodoscopes. However, single diffractive events are more difficult to detect because one particle stays in the beam pipe. The term "minimum bias" therefore usually refers to non single diffractive events. UA1 and UA5 studied such events in 1981 [23,24] and, in 1982[25], UA5 added a single diffraction trigger. The UA1 data were taken with field off to make acceptance calculations easier and UA5 in any case has no field. Thus, the data on charged particle multiplicities have been obtained as a function of pseudo-rapidity $\eta = -\ln \tan \theta/2$.

In 1969 Feynman[26] conjectured that, if the transverse momentum was limited, there should be a uniform distribution of particles as a function of pseudo-rapidity giving rise to the rapidity plateau, and that the pseudo-rapidity density $\frac{dn}{d\eta} = \frac{1}{\sigma_{inel}} \frac{d\sigma}{d\eta}$ should be independent of s, known as Feynman scaling. As the range of rapidity available increases as ln s, the average multiplicity would then increase as ln s. It was already known from the ISR that the average central rapidity density $(\frac{dn}{d\eta})_{\eta = 0}$ increases by 40% from $\sqrt{s}$ = 23 GeV to $\sqrt{s}$ = 63 GeV violating Feynman scaling. A continued rise, as ln s, is observed in going to the collider energy, $\sqrt{s}$ = 540 GeV (figure 18). As a consequence, the average inclusive charged particle multiplicity increase to $\langle n_{ch} \rangle = 28.9 \pm 0.4$ (figure 19) requires an $(\ln s)^2$ term to account for its energy dependence. However, the width of the pseudo rapidity distribution has grown by only 2 units from ISR to collider energy compared to the 4.6 units available kinematically. Furthermore, a cylindrical phase space distribution with $\langle p_t \rangle$ = 0.35 GeV/c (see figure 17) that describes the ISR data (dashed curve) fails to account for the collider results. One explanation could be that the mean particle transverse momentum has increased, so limiting the rapidity. Better agreement is obtained (solid curve) with $\langle p_t \rangle$ = 0.50 GeV/c. However, UA1 measurements[27] (see later) give $\langle p_t \rangle$ = 0.42 GeV/c so this may not be the whole reason.

4.2 Multiplicity distributions

If particles were produced randomly and independently their multiplicity might be expected to obey a Poisson distribution $P_n = \frac{e^{-\langle n \rangle} \langle n \rangle^n}{n!}$ which would become relatively narrower (as $\sim 1/\sqrt{n}$) as the energy and hence multiplicity increased. (The fact that some particles result from the decay of resonances already modifies this expectation. Any correlation between particles[29] will result in a broader distribution). Koba, Nielsen and Olesen[28] showed, starting from Feynman scaling, that on the contrary the shape of the distribution should tend to become constant as $s \to \infty$ (KNO scaling). Thus if $\langle n \rangle P_n$ is plotted against $n/\langle n \rangle$, where P_n is the probability of observing a multiplicity n, the distributions at different energies should coincide at sufficiently high energies. Early collider results (1981) from UA1[23] and UA5[24], when compared with ISR data were consistent with KNO scaling in spite of the violation of Feynman scaling. However, the UA5 data taken in 1982[25] show a deviation from KNO scaling particularly at high multiplicities (figure 20). Nevertheless scaling is observed for a restricted range of $|\eta|$ both by UA1[23] and UA5[25] (figure 21). A natural explanation for KNO scaling would be that a limited number of subprocesses is responsible for particle production, the number varying little with energy. The collider results hence have prompted renewed theoretical interest in the subject[30] but it will not be discussed further here.

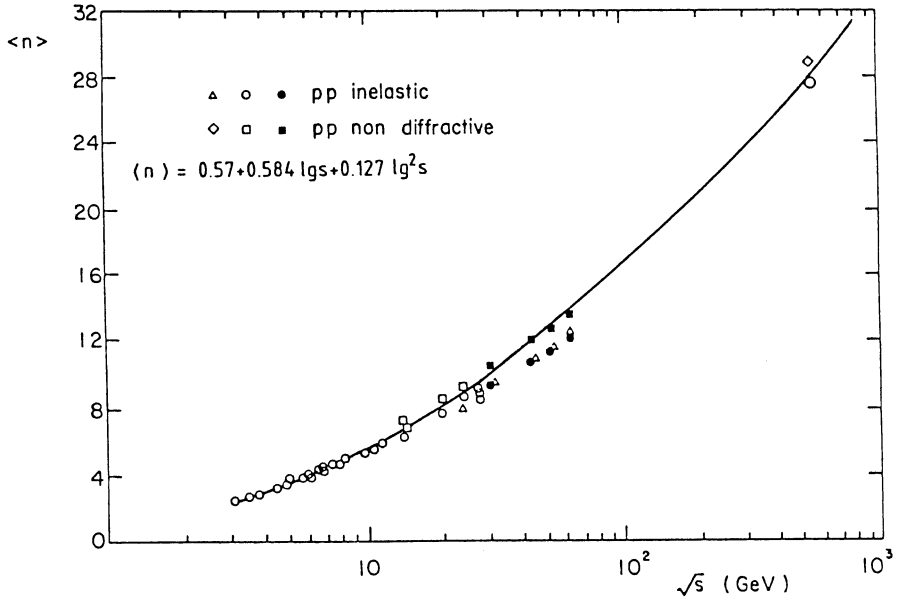

Figure 19 The average charged particle multiplicity for fully inclusive and non-single diffractive inelastic events versus energy. The curve (parameters given) is a fit to the non-diffractive events.

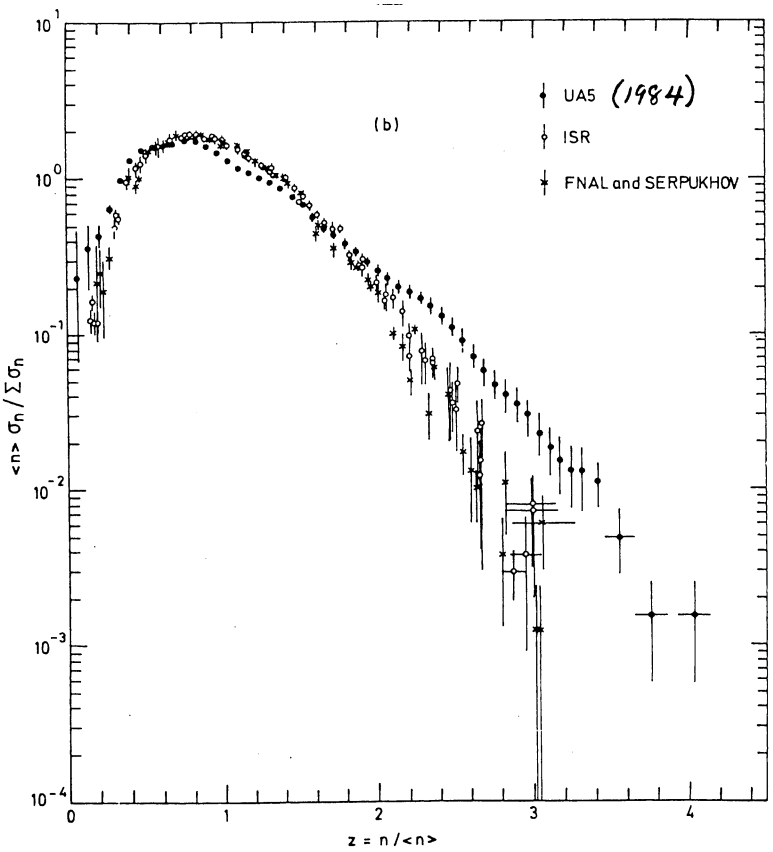

Figure 20 The charged multiplicity distributions at collider and lower energies plotted in KNO variables (see text). A deviation from KNO scaling is observed by UA5.

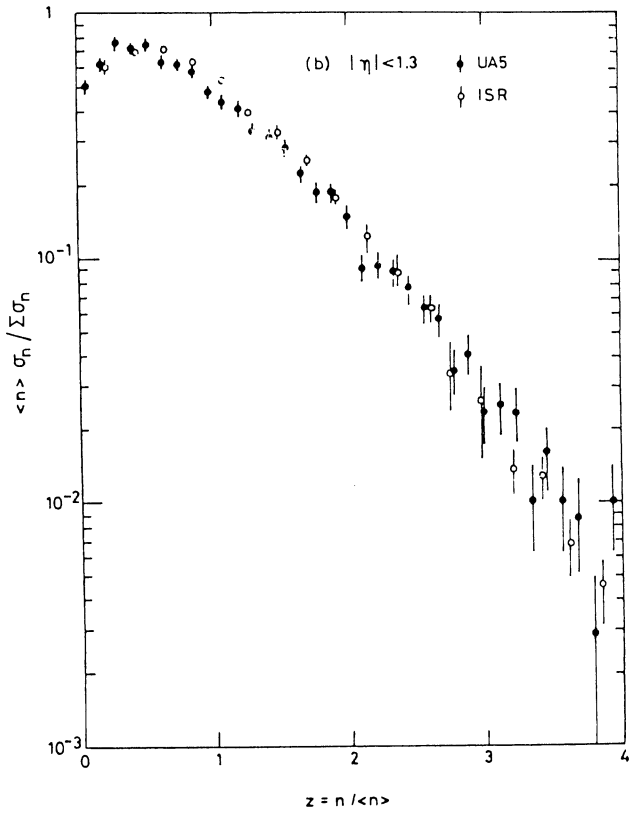

Figure 21. The charged particle multiplicity distributions for a restricted range of |η| 1.3. In this case KNO scaling is observed as seen also by UA1[23] (points not shown).

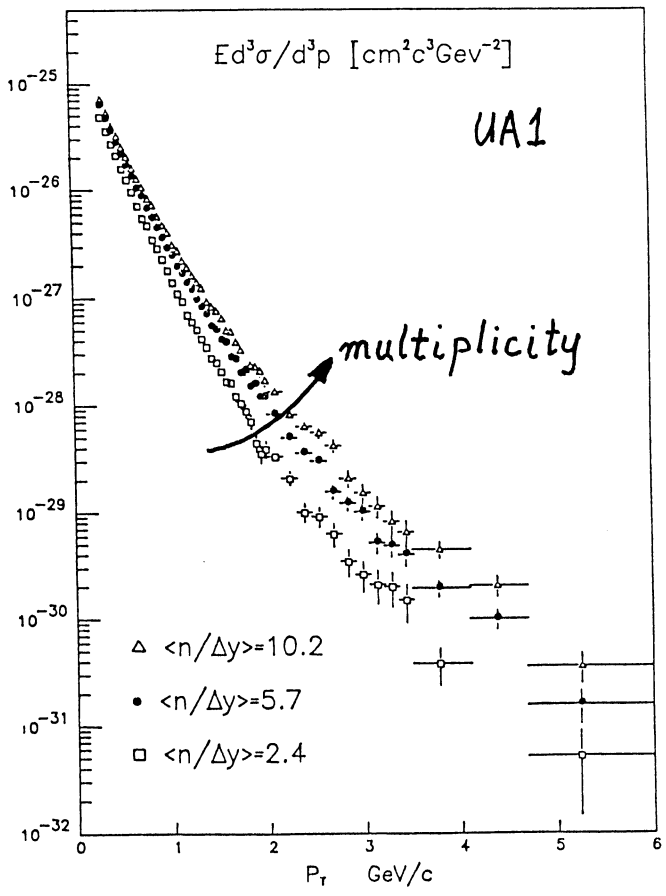

Figure 22. The invariant differential cross section as a function of p_t for different regions of rapidity density showing the multiplicity dependence.

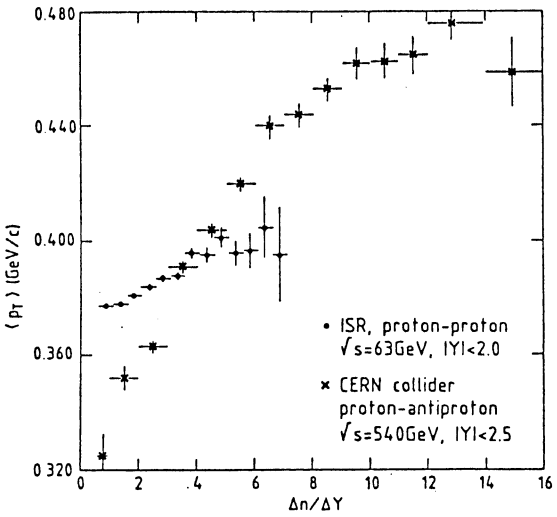

Figure 23. The growth of average p_t with rapidity density.

4.3 Single particle p_t-spectrum

The transverse momentum spectrum for unidentified charged hadrons observed by UA1[27] is given in figure 22 for three different bands of multiplicity averaged over the interval $|y| < 2.5$. The three spectra have been normalised to the full inclusive cross section at $p_t = 0$ [n.b. the invariant cross section $E\frac{d^3\sigma}{dp^3} = \frac{d^2\sigma}{dp_t^2 dy}$ since $\frac{dp_l}{dy} = E$]. Even at low p_t values the spectrum becomes flatter with increasing multiplicity, a result first noticed in cosmic ray experiments[31]. The average transverse momentum $\langle p_t \rangle$ increases with increasing multiplicity, an effect that begins to be apparent at the highest ISR energy $\sqrt{s}$ = 63 GeV (figure 23), and becomes constant at high multiplicities. Averaged over all multiplicities $\langle p_t \rangle = 0.42$ GeV/c. According to Van Hove[32] the observed behaviour could be an indication of a phase transition to a quark-gluon plasma. Indeed, an accompanying effect would be the observation of local density fluctuations in the rapidity plateau for which there is evidence from UA5[33]. Explanations of the p_t-variation exist also within conventional fragmentation models[34] but the effect in this case would be confined to large $|y|$. Further study would clearly be interesting but tends to receive a lower priority than W, Z, top, etc.

4.4 Strange and neutral particle production

UA2 have studied K, p and π productions using their wedge spectrometer[35]. UA5 have measured γ-ray production from their conversion in the beam vacuum pipe and in lead-glass plates: also K^o and Λ^o and Ξ decays[36]. Kaons have a higher average p_t than pions. Roughly summarised there are about 12% Ks, 5% baryons or antibaryons and 38% neutral particles per event.

4.5 Summary on particle production

In summary the following features have been observed, some of which are intriguing:

i) The width of the rapidity plateau ($\frac{dn}{d\eta}$ vs η) grows from the ISR to the collider but less than would be expected for constant $\langle p_t \rangle$.

ii) However, $\langle p_t \rangle$ rises from 0.35 to 0.42 GeV/c over the same energy range.

iii) The height of the plateau $\left(\frac{dn}{d\eta}\right)_{\eta = 0}$ rises as ln$s$ (continued violation of Feynman scaling).

iv) $\langle n_{ch} \rangle$ as a consequence requires an $(\ln s)^2$ term.

v) There is a deviation from KNO scaling at large multiplicities for $|\eta| < 5$, but scaling is observed for $|\eta| < 1.5$.

vi) $\langle p_t \rangle$ rises with multiplicity - a new feature that begins to set in at the ISR.

vii) A typical collision contains about 43 particles of which 28.9 ± 0.4 are charged (62%) with 12% Ks and 5% baryons/antibaryons.

viii) So far there has been no indication of bizarre processes such as the Centauro events oberved in cosmic ray experiments[37,38].

5. JET PRODUCTION AND QCD

5.1 Introduction

One of the striking features of collider results is the cleanness of jets (see

EVENT 2737. 289.

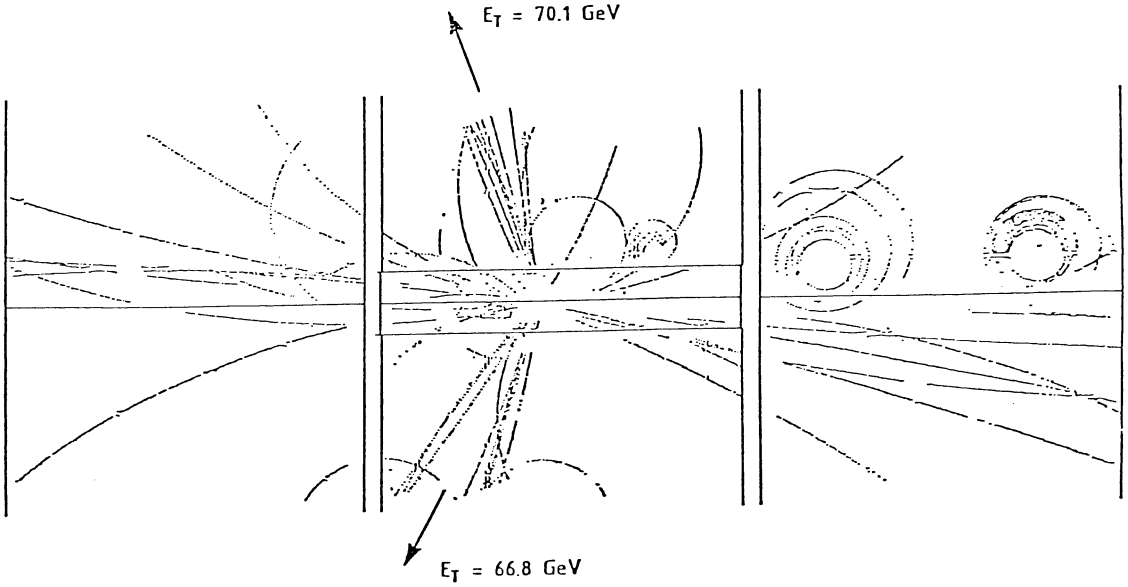

Figure 24 A typical two-jet event in the UA1 experiment showing the central detector tracks.

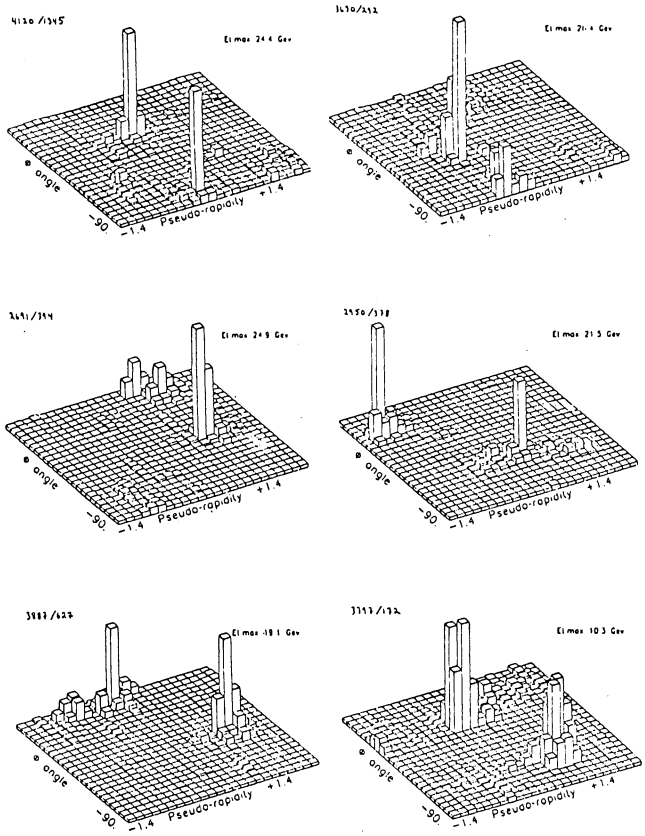

Figure 25. "Lego" plots of two-jet events in the UA1 experiment. The axes are pseudo rapidity, η, and azimuth, ϕ. The heights of the bins are proportional to transverse energy.

figures 24 and 25) resulting from parton-parton scattering and the excellent agreement with expectations from QCD. Unlike the situation at e^+e^- machine where the basic jets are from quarks and antiquarks

$$e^+e^- \rightarrow q\bar{q}$$

the initial partons at the $p\bar{p}$ collider may be quarks, antiquarks or gluons which may collide in any combination. Furthermore their relative contributions depend on the proton structure functions and, of course, there are spectator partons. As the gluon structure function is softer (concentrated at low values of Bjorken x) gluons tend to dominate

scattering at low x_T, where $x_T = p_t/p_t^{max} = 2p_t/\sqrt{s}$ is the fractional transverse momentum of the produced jet.

For larger values of $x_T (\gtrsim 0.2)$, i.e. $p_t \gtrsim 50$ GeV/c, valence quarks and antiquarks become increasingly important as only they can carry enough momentum to provide the required p_t. Both UA1 [39-42] and UA2 [43-46] have obtained results on cross sections, angular distributions and fragmentation of jets, as well as three-jet events consistent with gluon radiation.

5.2 Data taking and trigger

Both experiments used a calorimeter trigger:-

UA1 a) $\sum E_T$ ($|\eta| < 1.5$) > 20, 30, 40, 50 GeV

b) 'jet' trigger E_T(8G + 2C) > 15 GeV

E_T(end cap quadrant) > 15 GeV

UA2 $\sum E_T(|\eta| < 1.0) > 25, 40$ GeV

Cuts were applied to the analyzed data to remove beam-gas and halo events yielding, after cuts:-

	UA1	UA2
Background	1%	5%
Event losses	2%	5%

The resulting data samples are:-

UA1	1982	14 nb^{-1}
	1983	118 nb^{-1}
UA2	1982	15 nb^{-1}
	1983	112 nb^{-1}

5.3 Jet Algorithms

Somewhat different algorithms are used in the two experiments to select jets. In UA1 the following procedure is used:-

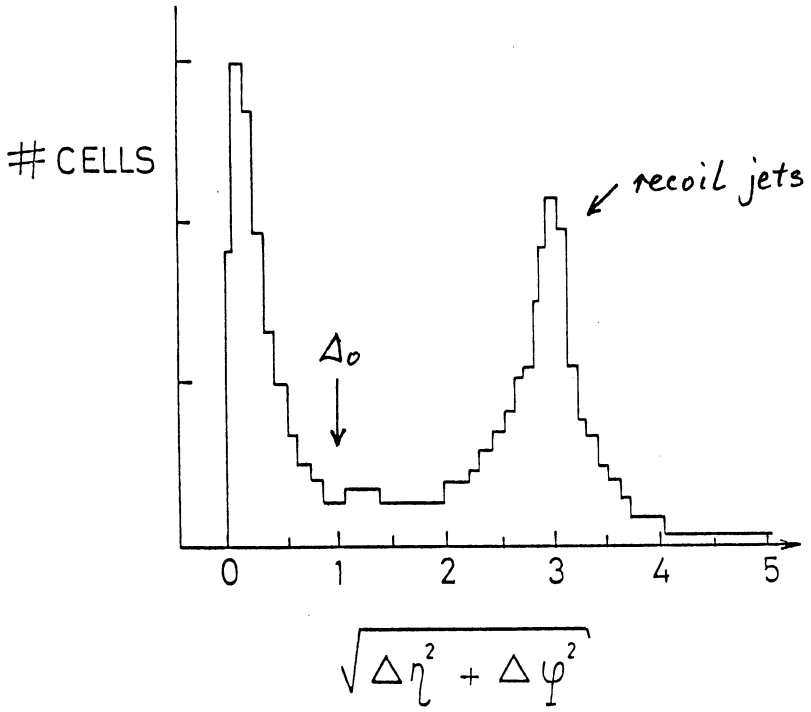

Figure 26 The UA1 jet algorithm selects calorimeter cells according to their proximity in η, ϕ space. A cut is made at r = 1, where $r = \sqrt{\Delta\eta^2 + \Delta\phi^2}$.

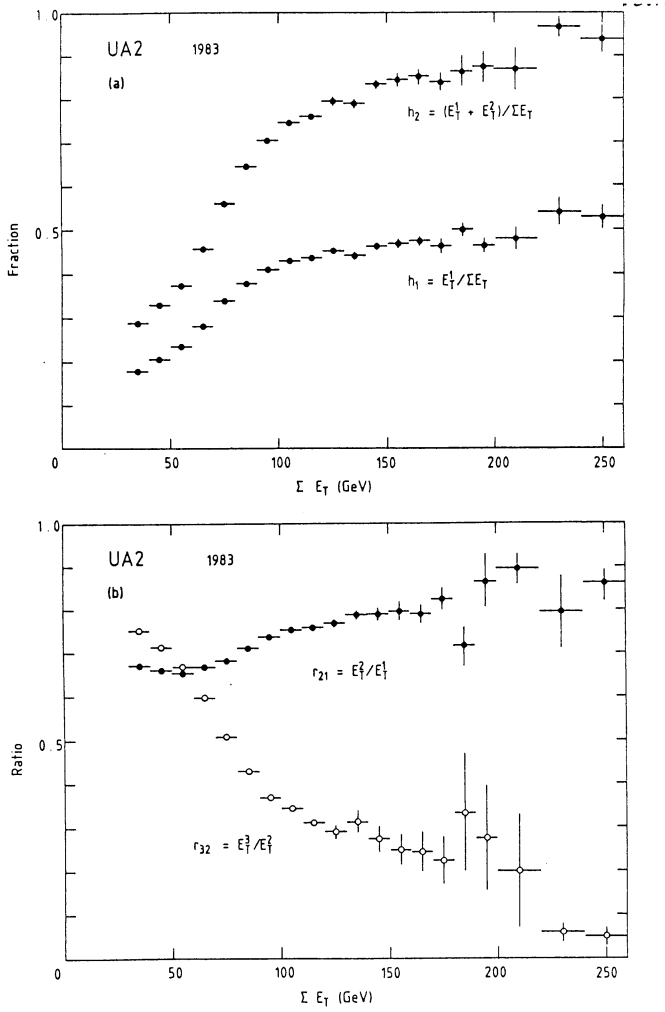

Figure 27 a) The fractional transverse energy carried by the leading jet and the leading two jets in UA2.
b) The ratio of the transverse energies of the second jet to the first and the third to the second.

i) Construct an E_T 'vector' for each of the 548 electromagnetic and hadronic cells with $|\eta| < 3$.

ii) Order cells with $E_T > 2.5$ GeV.

iii) Using these as initiators, associate cells with $\sqrt{\Delta\eta^2 + \Delta\phi^2} < \Delta_o = 1$ to form clusters (see figure 26).

iv) Add the remaining cells to the nearest cluster if p_t relative to the jet axis is < 1.0 GeV/c and $\Delta\theta_{relative} < 45^o$.

Note that, because of the rapidity plateau, the background from soft processes should be uniform in $\eta - \phi$ space.

The UA2 algorithm has two stages:-

i) join cells with a common side for cells with $E_T > 0.4$ GeV.

ii) split the clusters if there is a valley deeper than 5 GeV between two local maxima.

UA2 then order the jets so found in decreasing E_T; $E_T^1 > E_T^2 > E_T^3$ etc.

They define $h_1 = E_T^1 / \sum E_T$

$$h_2 = (E_T^1 + E_T^2) / \sum E_T$$

$$r_{21} = E_T^2 / E_T^1$$

$$r_{32} = E_T^3 / E_T^2 \quad \text{etc.}$$

For a pure 2-jet event $h_1 = 0.5$ and $h_2 = 1$. Also $r_{21} = 1$ and $r_{32} = 0$.

Figure 27 shows the results from the 1983 data for these quantities which clearly demonstrate the 2-jet dominance for $\sum E_T > 100$ GeV where the jet algorithm is correctly finding the jets.

Internal properties of jets

Four jet characteristics have been studied by the two experiments:-

i) Transverse energy flow

ii) Fragmentation function

iii) p_t of charged particles with respect to the jet axis

iv) charged particle multiplicity.

Figure 28 shows the transverse energy density in jets with $E_T > 35$ GeV for the UA1 experiment.

The curves are the ISAJET Monte Carlo programme[47] and cylindrical phase space[48].

The former is a closer approximation to the data. Note that the bin size of the data does not limit the resolution.

Figure 29 shows the charged particle density in UA1 versus the angle relative to the jet axis for various cuts on the p_t of the particles with respect to the beam direction. The dashed curve is a Monte Carlo calculation with no jets. For p_t (beam) > 2.0 GeV/c essentially all jet fragments are contained within a 35^o cone around the jet axis. Consequently this has been used as a somewhat arbitrary cut to determine the fragmentation function. Obviously the selection (angle, p_t) and background processes (from the remaining partons) affect the choice of particles belonging to a jet. This is clearly a

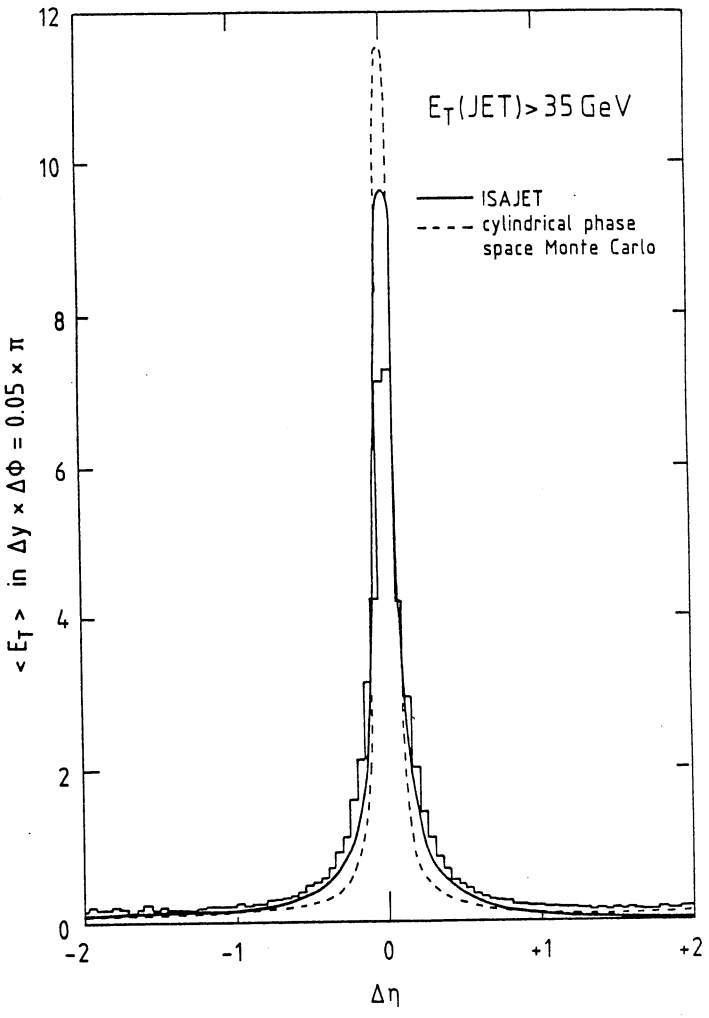

Figure 28 The transverse energy flow in jet events (UA1) jet events (UA1) as a function of $\Delta\eta$ with respect to the jet axis compared to Monte Carlo calculations.

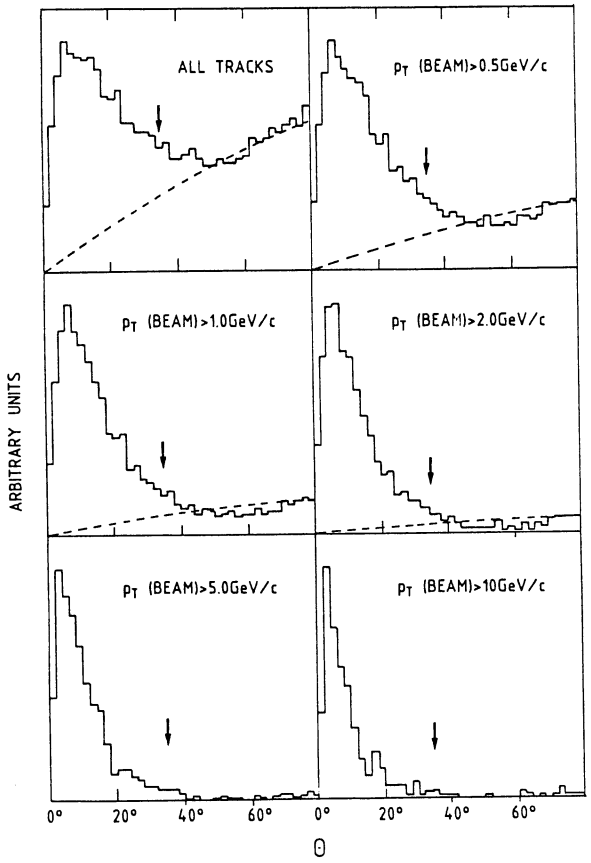

Figure 29 The charged particle density versus the particle angle relative to the jet axis in UA1 for various cuts on the p_t of the particle with respect to the beam direction. The dashed curve is a Monte Carlo calculation with no jets.

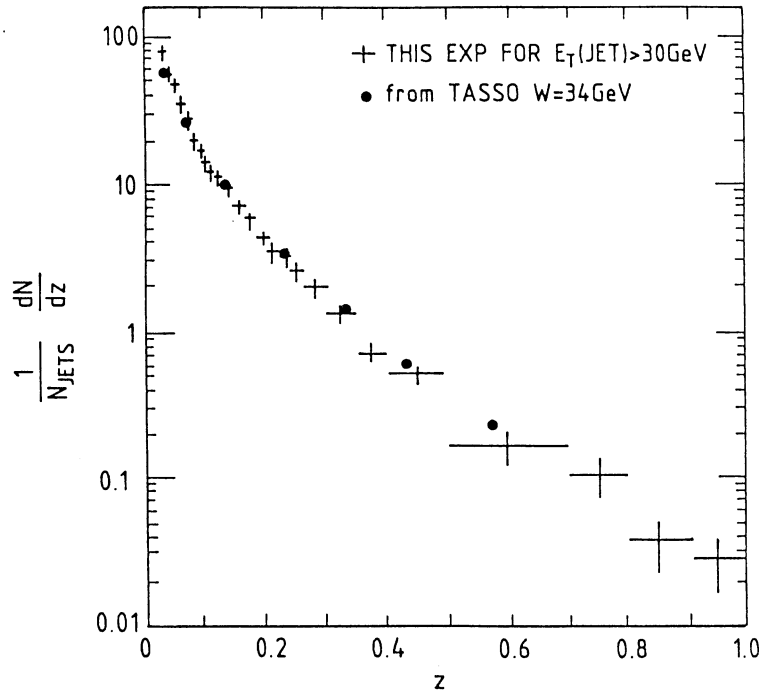

Figure 30 The charged particle fragmentation function for UA1 jets with E_T > 30 GeV compared to equivalent data from the TASSO e^+e^- experiment at $\sqrt{s}$ = 34 GeV.

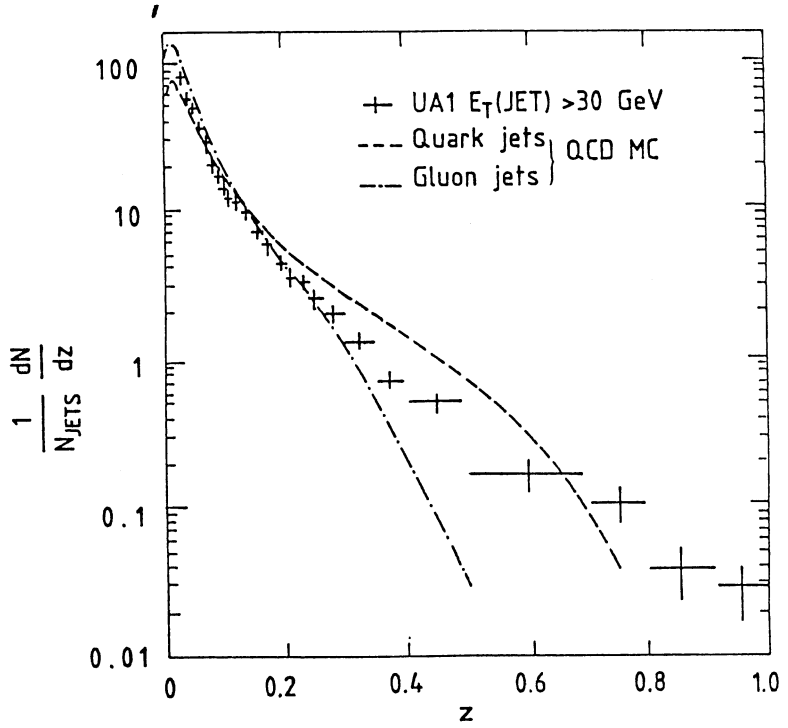

Figure 31 Comparison between the UA1 fragmentation function and a QCD Monte Carlo calculation (B. Webber[50]) for quark and gluon jets.

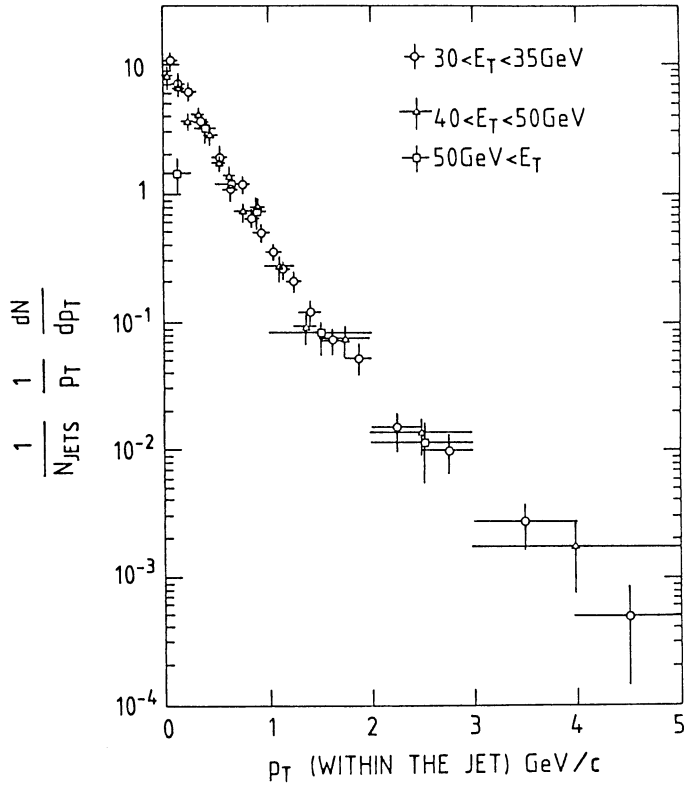

Figure 32 The transverse momentum distribution of charged particles with respect to the jet axis for $z > 0.1$ and three bands of jet E_T (UA1).

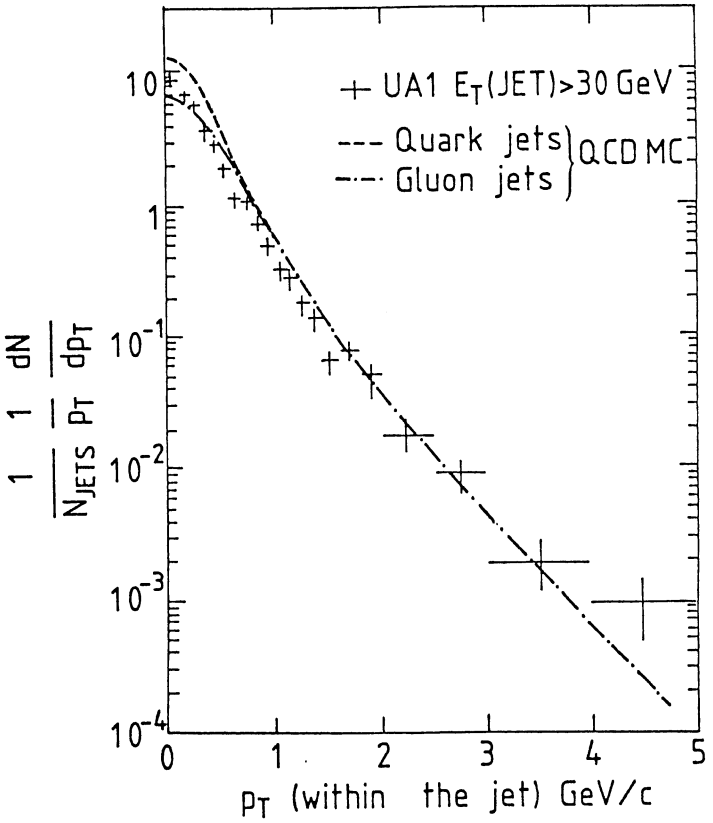

Figure 33. A comparison between the transverse momentum distribution of charged particles with respect to the jet axis and a QCD Monte Carlo calculation[50].

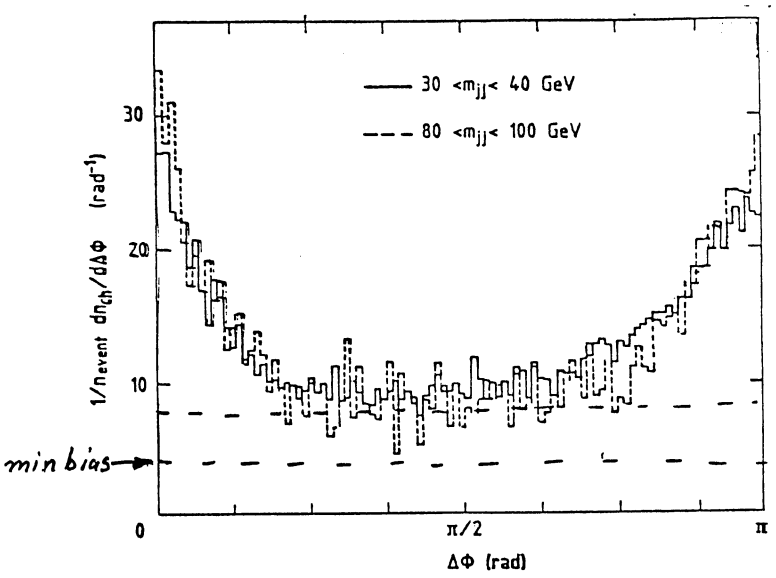

Figure 34. The charged particle density in UA2 jets as a function of $\Delta\phi$ with respect to the jet axis. The background level ($\Delta\phi = \pi/2$) is approximately twice the level for minimum bias events as observed also by UA1.

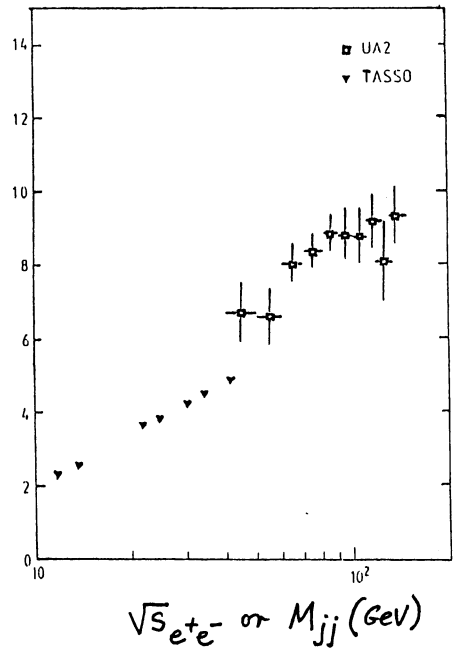

Figure 35. A lower bound on the mean charged multiplicity in TASSO and UA2 jets as a function of $\sqrt{s}$ or m_{jj} (i.e. after subtracting a constant background of 2 x minimum bias).

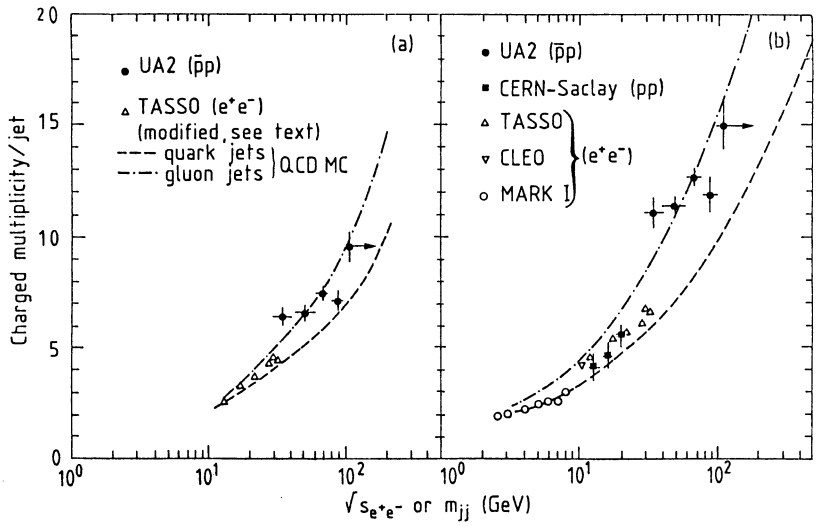

Figure 36. A comparison between the mean charged multiplicity in UA2 and TASSO jets and a QCD Monte Carlo calculation [50] with two different background subtractions.

more difficult problem than with e^+e^- jets where there are no spectator particles. The fragmentation function is defined as

$$D(z) = (dN/dz)/N(jet)$$

where $z = \underline{p} \cdot \underline{n}\ (jet)/E_{jet}$, i.e. the fractional component of momentum along the jet axis. N is the number of charged tracks and N(jet) the number of jets in the sample.

$$\therefore\ N/N(jet) = \int_0^1 D(z)dz$$

As an example of the magnitude of the bias that may be introduced by the selection procedures it is estimated that the 35° cut in UA1 loses 35% of the particles for $0.02 < z < 0.03$ and 5% for $z < 0.07$, for jets with $E_T > 30$ GeV.

Figure 30 shows the fragmentation function obtained compared to the e^+e^- result from TASSO with total energy W = 34 GeV[49]. No correction has been applied for the loss of particles at low z or for the uncertainty on the jet energy ($\sim \pm$ 15%) which smears z. The shapes of the distributions are remarkably similar. At first sight this is somewhat surprising as the $p\bar{p}$ data are expected to be dominated by gluon jets at these E_T values whereas the e^+e^- data are quark jets. Gluon jets naively should have a softer fragmentation function than quark jets since a gluon must first turn into a $q\bar{q}$ pair as part of the fragmentation process. However, a comparison with a QCD Monte Carlo calculation[50] in figure 31 indicates that the UA1 results (apart from a few high-z points) are somewhere between the quark and gluon expectations, a not unreasonable result at the present stage of the data, showing that the higher energy of the collider data also affects the shape of the fragmentation function.

Figure 32 shows the p_t of charged particles with respect to the jet axis for $z > 0.1$ and three bands of jet E_T. No significant differences between the spectra are noticeable. A comparison with the QCD Monte Carlo[50] in figure 33 (same cuts) shows perhaps a slight preference for the gluon prediction. The average value p_t is 0.6 GeV/c.

Figure 34 shows the charged particle density for two bands of jet-jet invariant mass, obtained in the UA2 experiment[46], plotted against $\Delta\phi$, the difference in ϕ between the particle and the jet-axis. There is a constant background level which is approximately twice the density in minimum bias events. The behaviour is seen also by UA1[40]. Presumably this has to be interpreted as soft gluon emission from the jets. UA2 have obtained a lower bound on the mean charged multiplicity of their jets as a function of M_{jj} (after subtracting a constant background of 2 x minimum bias) which is compared in figure 35 with results from TASSO. Figure 36 is a comparison with the QCD Monte Carlo[50] for two different background assumptions, the UA2 results appearing to favour the expectations for gluon jets.

In summary, the data are dominated by two-jet events which at the present level of study are certainly compatible with being mainly gluon jets as expected.

5.4 Multijet events

Events with three or more jets can arise from gluon bremsstrahlung from initial or final state partons.

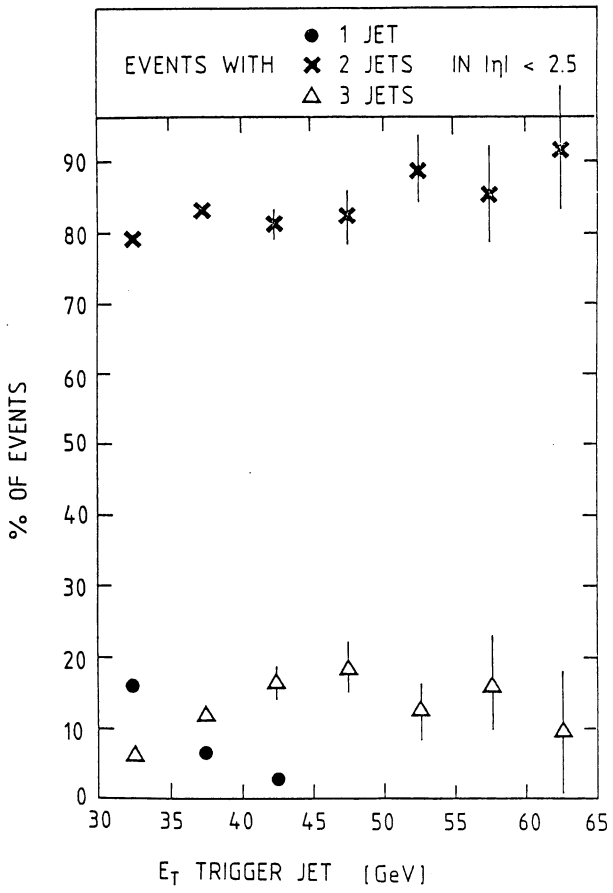

Figure 37 The fraction of 1, 2 and 3-jets with E_T > 15 GeV, $|\eta|$ < 2.5 observed in UA1. The 'trigger' jet has E_T > 30 GeV, $|\eta|$ < 1.5 and is included in the count.

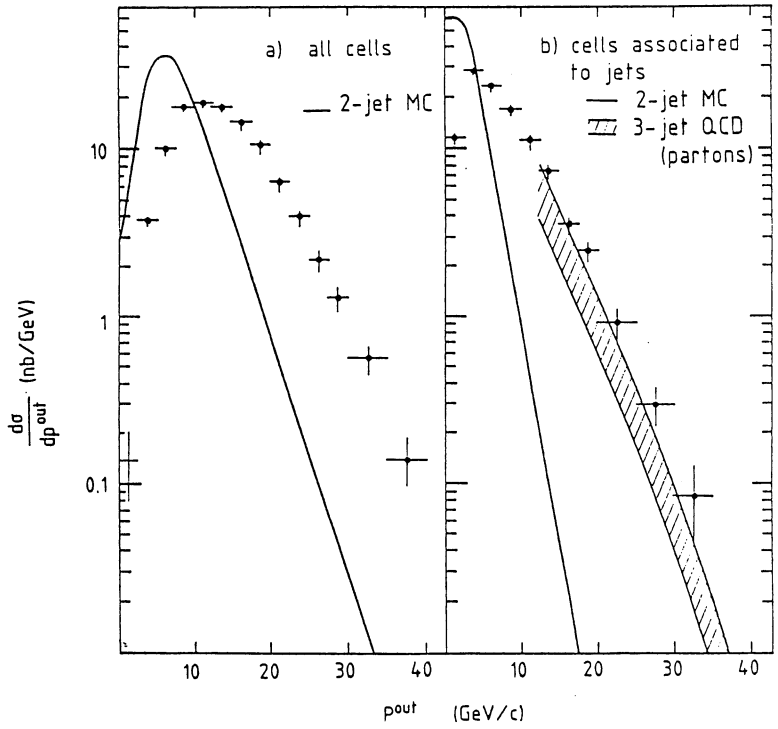

Figure 38 A plot of p^{out} for multijet events in UA1. p^{out} is the amount of momentum perpendicular to a plane containing the beam and the trigger jet. The data agree with a 3-jet QCD Monte Carlo calculation[51].

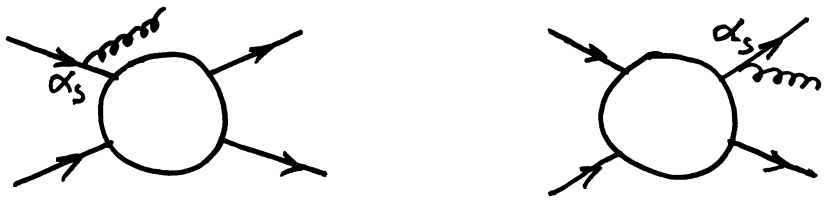

The ratio of 3-jet to 2-jet events should therefore be of the order α_s(~15%). In principle this offers a way to measure α_s but is obviously sensitive to cuts and to the fact that there is a continuous transition between two and three jet events as the radiated gluon becomes harder. Up to now only the general features have been studied at the $p\bar{p}$ collider but the events appear to have the expected characteristics.

UA1 define a "trigger" jet as one with $E_T > 30$ GeV and $|\eta| < 1.5$ and count the fraction of one, two and three jet events where the additional jet has $E_T > 15$ GeV and $|\eta| < 2.5$. As seen in figure 37, the fraction of 3-jet events is indeed of the order of 15% but no allowance has been made for acceptance. A more quantitative comparison has been made noting that the multijet events do not in general lie in a plane containing the trigger jet and the beam. A comparison of the amount of momentum perpendicular to this plane (p_{out}) shows good agreement with a QCD Monte Carlo[51] (see figure 38). More refined analyses are in progress.

5.5 Angular distribution for 2-jet events and structure functions

An extensive study of the formulae describing parton-parton scattering has been carried out by B. Combridge et al.[52,53]. For a 2-jet process one can write

$$\frac{d^3\sigma}{dx_1 dx_2 d(\cos\theta)} = \sum_{ij} \frac{F_i(x_1)}{x_1} \frac{F_j(x_2)}{x_2} \frac{d\sigma_{ij}}{d(\cos\theta)} \qquad (1)$$

where θ is the centre of mass scattering angle and $F_i(x)$, $F_j(x)$ are the structure functions. The sum is over the different combinations of partons in the proton (i) and antiproton (j). $\frac{d\sigma_{ij}}{d(\cos\theta)}$ are the respective cross sections (e.g. qg, gg, $q\bar{q}$, etc.) and are calculable in QCD. Elastic sub-processes (i.e. ones where the initial and final state partons are the same) are mediated by t-channel gluon exchange and are expected to dominate for small $\hat{t}$, the sub-process four-momentum transfer squared. In fact for vector gluons they depend

essentially on $\frac{1}{\hat{t}^2} \propto \frac{1}{(1-\cos\theta)^2}$ which is the familiar angular dependence of Rutherford scattering

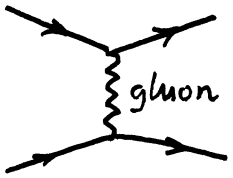

elastic

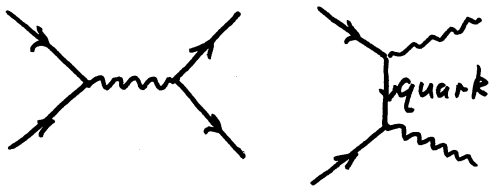

inelastic

Processes involving s-channel gluon exchange or quark exchange are generally inelastic - the final state partons are different from the initial ones - and have a much weaker angular dependence[53]. Consequently, at sufficiently large values of $\cos\theta$, the angular dependences of the dominant sub-processes ($gg \to gg$, $gq \to gq$, $g\bar{q} \to g\bar{q}$, $q\bar{q} \to q\bar{q}$) are approximately the same. In the approximation that they are identical one may make a considerable simplification of equation (1) which factorises to give

$$\frac{d^3\sigma}{dx_1 dx_2 d(\cos\theta)} = \frac{F(x_1)}{x_1}\,\frac{F(x_2)}{x_2}\,\frac{d\sigma}{d(\cos\theta)}$$

where $\frac{d\sigma}{d(\cos\theta)}$ is a common differential cross section and $F(x)$ is an effective structure function which incorporates "colour factors" to account the different relative couplings of qq, qg, etc. In terms of the gluon, quark and antiquark structure functions $G(x)$, $Q(x)$ and $\bar{Q}(x)$ one finds

$$F(x) = G(x) + \frac{4}{9}\,(Q(x) + \bar{Q}(x))$$

which gives the appropriate relative rates for all the contributing subprocesses when $F(x_1)$ and $F(x_2)$ are multiplied. As gluon-gluon scattering is expected to be the most important for $E_T(\text{jet}) \lesssim 50$ GeV we write the gluon-gluon differential cross section in full

$$\frac{d\sigma}{d(\cos\theta)} = \frac{9}{8}\,\frac{\pi\alpha_s^{\,2}}{2x_1x_2s}\,\frac{(3 + \cos^2\theta)^3}{(1 - \cos\theta)^2} \qquad (2)$$

where $x_1x_2s = \hat{s}$ is the parton-parton centre of mass energy squared. In summary, the approximation that the angular distributions have the same shape allows us to extract a combined structure function from the data. It remains only to determine the values of x_1, x_2 and $\cos\theta$ on an event by event basis so that the rate can be determined in terms of x_1, x_2 and $\cos\theta$. Integrating over $\cos\theta$ then allows $F(x_1)$ or $F(x_2)$ to be found if factorization holds.

Let $\underline{p}_1$ and $\underline{p}_2$ be the three-momenta of the incoming partons, $\underline{p}_3$ and $\underline{p}_4$ the three-momenta of the outgoing partons. (n.b. the lowest E_T jet in 3-jet events is ignored and the effect corrected by Monte Carlo). $p_1 = x_1\sqrt{s}/2$; $p_2 = x_2\sqrt{s}/2$; $\underline{p}_3$ and $\underline{p}_4$ are measured.

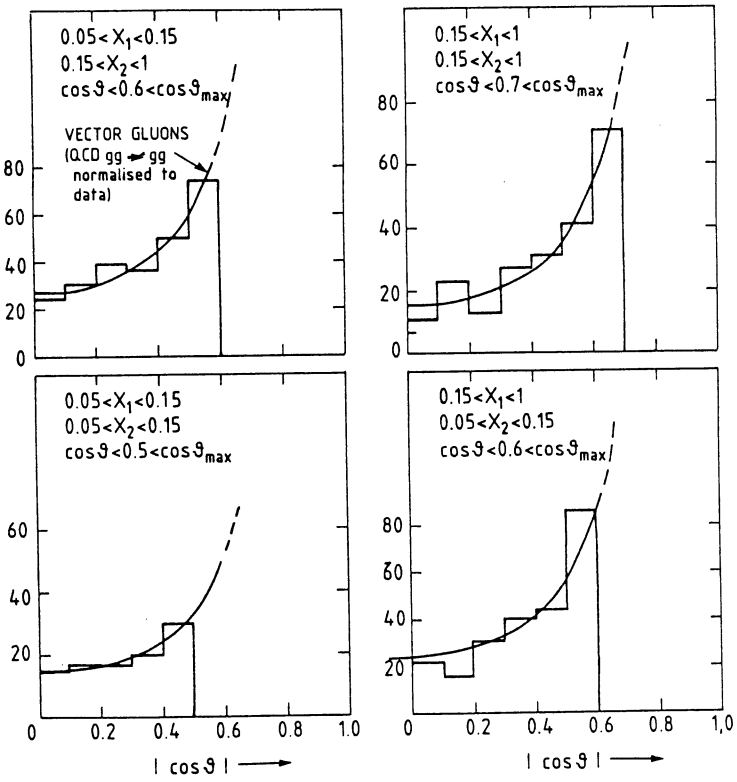

Figure 39 Angular distributions in the parton-parton centre of mass for various x-ranges of the colliding partons. The curves are for vector gluon exchange (normalised to the data).

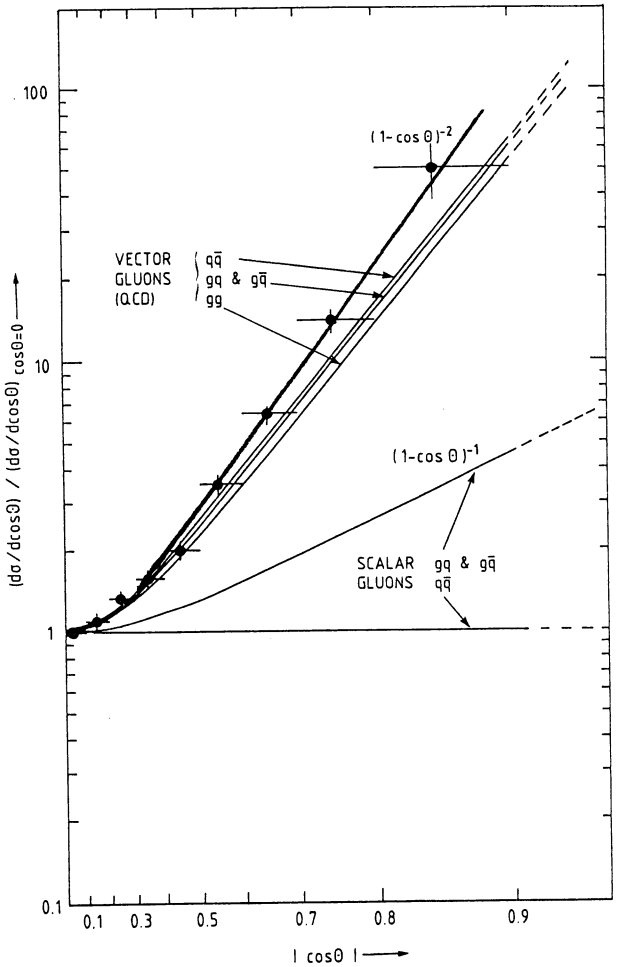

Figure 40 The combined parton-parton angular distribution in UA1 corrected for acceptance. The upper curve is for gluon-gluon scattering allowing for the variation of α_s with Q^2. Scalar gluon exchange is clearly excluded. The theoretical curves are normalised at cos θ = 0.

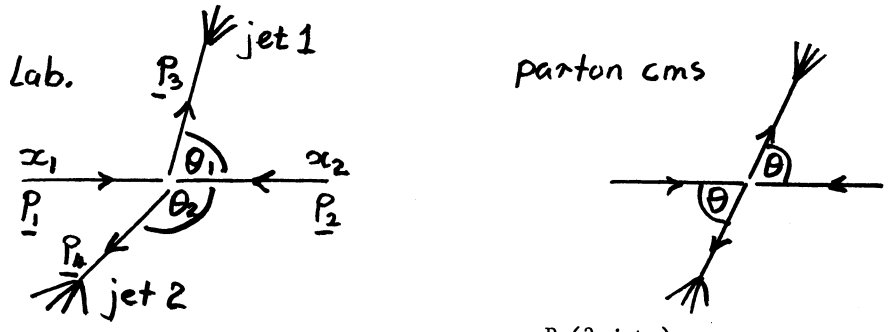

Now $\hat{s}$ (measured) = $x_1 x_2 s$ and $x_F = x_1 - x_2$ where $x_F = \dfrac{P_L(2\text{ jets})}{P_{beam}}$. Solving for x_1, x_2 one finds

$$x_1 = [x_F + \sqrt{x_F^2 + 4\tau}] \;/\; 2$$

$$x_2 = [-x_F + \sqrt{x_F^2 + 4\tau}] \;/\; 2$$

Finally $\cos\theta = \dfrac{(\underline{P}_3 - \underline{P}_4).\,(\underline{P}_1 - \underline{P}_2)}{|\underline{P}_3 - \underline{P}_4|\;\;|\underline{P}_1 - \underline{P}_2|}$

The limited y (rapidity) acceptance means that the accessible $\cos\theta$ range depends on x_1 and x_2. Figure 39 shows the angular distributions for regions of full acceptance obtained by UA1[42] for various x_1, x_2 ranges. The curves are for vector gluon exchange. Figure 40 shows the combined distribution obtained in UA1 with curves for the three main subproceses, normalised at $\cos\theta = 0$. The expectations for scalar gluon exchange are also shown and are clearly excluded by the data. Interestingly, even better agreement is obtained if allowance is made for the Q^2 dependence of α_s in the differential cross section formula (2) where Q^2 is taken to be $-\hat{t}$. Similar results have been obtained by UA2[46].

To extract the effective structure function F(x) it is important to verify that factorization is working, i.e. that $F(x_2)$ is independent of the value of x_1 (and vice versa). The data determine a quantity $S(x_1,x_2)$ if $d\sigma/d(\cos\theta)$ is known

$$S(x_1,x_2) = \frac{x_1 x_2 (d^2\sigma/dx_1 dx_2)}{\int_0^{\cos\theta_{max}} K \dfrac{d\sigma}{d(\cos\theta)}\, d(\cos\theta)}$$

where $\cos\theta_{max}$ is the maximum value of $\cos\theta$ permitted for given values of x_1, x_2. The theoretical form of $d\sigma/d(\cos\theta)$ was used by UA1[53] and K is a factor to allow for higher order corrections (K-factor). In the theoretical expressions for $d\sigma/d(\cos\theta)$

$$\alpha_s = 12\pi/[23\,\ln(Q^2/\Lambda^2)]$$

which asumes 5 effective flavours of quarks. Λ was taken to be

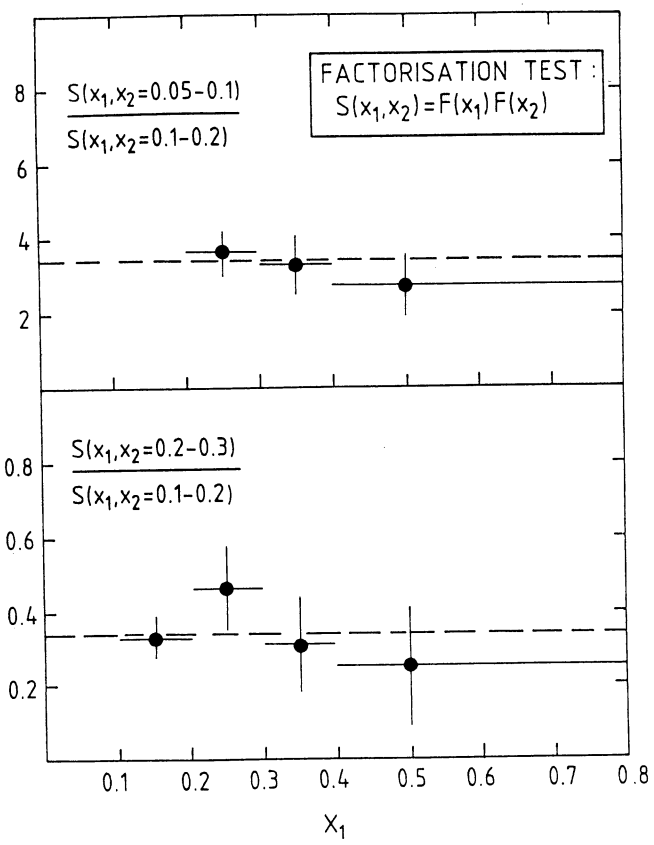

Figure 42 A demonstration that the product of the structure functions obtained from the UA1 data factorises. i.e. $F(x_2)$ is independent of the value of x_1.

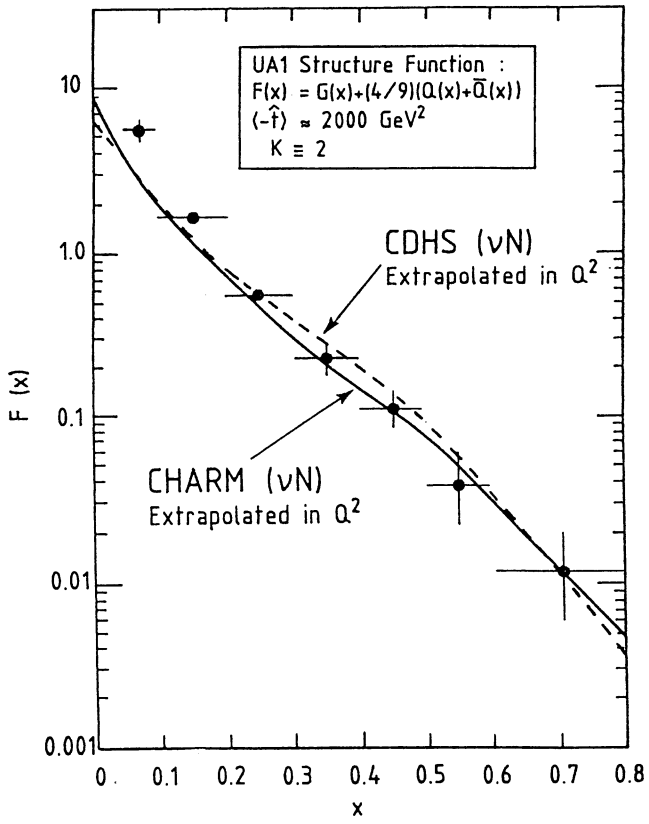

Figure 43 The structure function $G(x) + 4/9\ (Q(x) + \bar{Q}(x))$ derived from the UA1 jet data [$Q^2 \sim 2000$ GeV^2]. The curves are the results for the same quantity measured in the CDHS and CHARM experiments ($Q^2 = 20$ GeV^2) extrapolated in Q^2.

0.2 GeV and $Q^2 = -\hat{t}$. As can be seen from figure 42, factorization appears to work

$$\text{i.e. } S(x_1,x_2) = F(x_1)F(x_2).$$

The resulting structure function, assuming K = 2, $F(x) = G(x) + \frac{4}{9}\ (Q(x) + \overline{Q}(x))$ is shown in figure 43. Also shown is the same function from the CDHS and CHARM experiments[54] obtained at $Q^2 = 20\ \text{GeV}^2$ but extrapolated to $Q^2 = 2000\ \text{GeV}^2$, the average Q^2 of the UA1 data. A similar analysis has been performed by UA2[46] and is in good agreement with UA1. The conclusion is that the collider data are entirely compatible with QCD expectations, showing the expected angular distribution for vector gluon exchange and compatibility with low energy results evolved to collider energies for the structure functions.

5.6 Jet production cross sections

In determining jet cross sections it is necessary to allow for various systematic effects, the most important being the luminosity, the content (correctness of the assignment of calorimeter elements to jets by the algorithms) and the calibration of the energy scale. A Monte Carlo procedure is used to estimate a correction factor for the jet content. Jets are generated in the apparatus, with shower simulation in the calorimeters, and then reconstructed by the algorithm. A comparison of $\frac{dN}{dE_T}$ (found) with $\frac{dN}{dE_T}$ (generated) then allows a correction to the cross section to be obtained which is $\sim$1.25 and only weakly dependent on E_T. There is, of course, a dependence on the reliabiity of the Monte Carlo simulation itself.

The calibration of the energy scale includes an allowance for the different response of the electromagnetic calorimeters to hadrons and photons which is a correction of $\sim$1.2. For UA1 the uncertainties on the energy scale are

absolute calibration e.m.	± 3%
had.	± 5%
e.m./had. response correction	± 5%
	± 7%

The resulting cross section errors for the two experiments are:-

	UA1	UA2
energy scale	±50%	±20%
luminosity	±20%	±20%
jet algorithm	±20%	±35%
Monte Carlo	±20%	
	±65%	±45%

Figure 44 shows the UA1 inclusive jet cross secitons[40]. The shaded band is the QCD prediction[55]. Figure 45 shows a comparison between UA2[45] and UA1 (1981 and 1982 data) cross sections and figure 47 a comparison between UA2 results for inclusive cross sections and 2-jet masses with QCD expectations. In all cases the agreement is excellent.

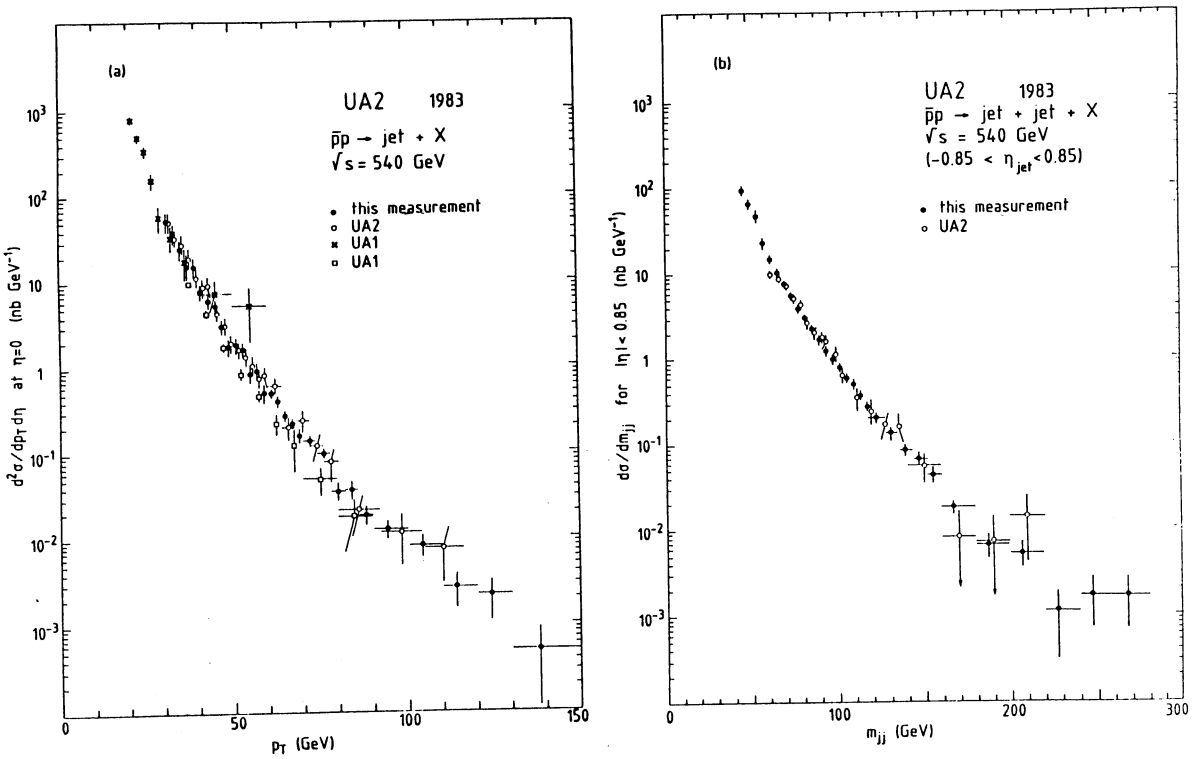

Figure 44 a) UA2 inclusive jet cross sections compared to 1981-2 data
b) jet-jet mass distribution from UA2.

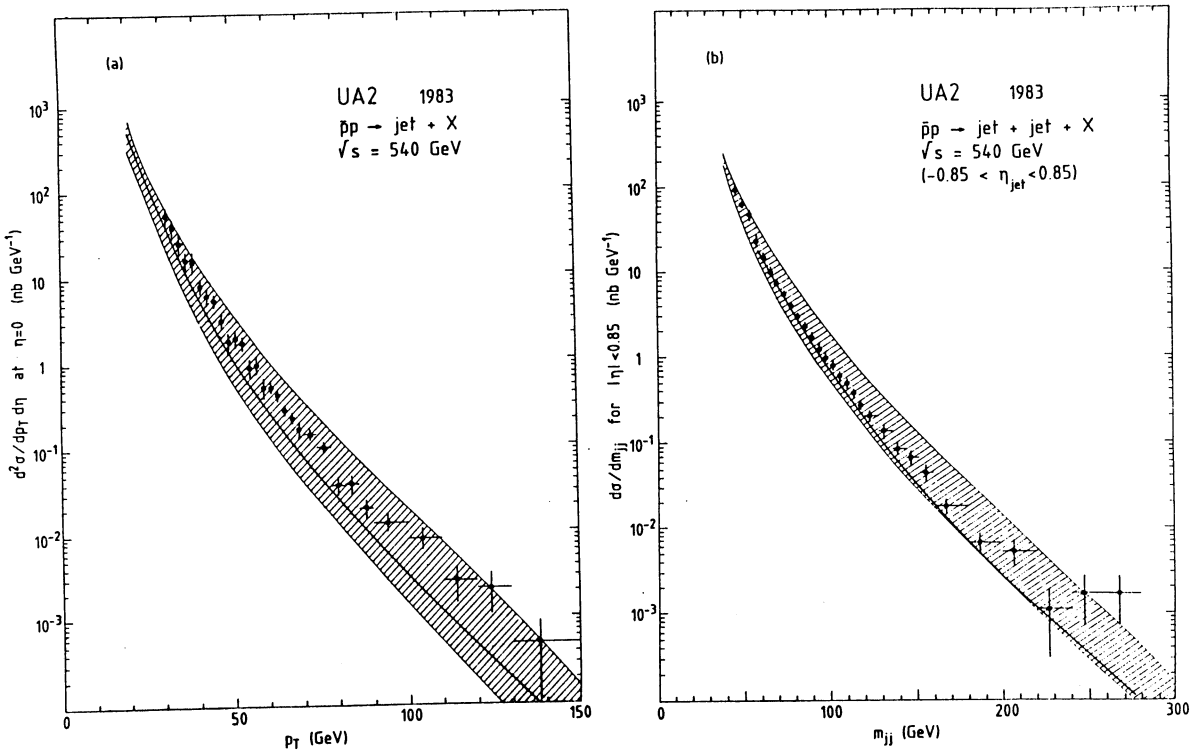

Figure 45 a) inclusive jet cross sections compared to QCD (hatched band)
b) jet-jet mass distribution compared to QCD.

5.7 Summary of jet physics

i) 2-jet events dominate at high E_T (85%)

ii) the rate of 3-jet events is compatible with QCD ($O(\alpha_s)$)

iii) the fragmentation function for pp jets (mainly gluons) is similar to that for e^+e^- jets (quarks) but agrees with QCD expectations when the higher collision energy is taken into account

iv) the $\langle p_t \rangle$ of charged particles with respect to the jet axis is $\sim$0.6 GeV and agrees with QCD

v) the 2-jet centre of mass angular distribution, $(1-\cos\theta)^{-2}$, supports vector gluon exchange

vi) the effective structure function $F(x) = G(x) + \frac{4}{9}(Q(x)+\bar{Q}(x))$ shows the expected evolution from $Q^2 = 20$ GeV^2 to $Q^2 = 2000$ GeV^2

vii) the jet cross sections and 2-jet mass distributions agree with QCD up to E_T of 150 GeV and m_{jj} of 270 GeV respectively.

6. W AND Z PHYSICS

6.1 Introduction

The main features of the standard electroweak model have been described elsewhere in this school[56,57]. We shall concentrate on the properties of the W and Z particles and how they are determined experimentally. Then we shall review the extent to which the standard model is checked by the UA1 and UA2 results and the expected improvements in the future. An excellent account of the collider results is given in reference 58.

6.2 The W and Z masses

Irrespective of the fine details one may obtain an order of magnitude estimate of the W mass under the assumption that the electromagnetic and weak coupling strengths are the same (unification) but that the two interactions are mediated by a massless photon and a massive W respectively. The point-like four fermion interaction is characterised by a single constant G_F (Fermi constant) which determines the rate of β-decay (strictly $d \to u e \bar{\nu}_e$). Under the W boson hypothesis this is replaced by a coupling constant g at each of the quark and lepton vertices, and the boson propagator.

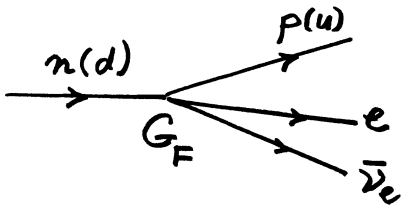

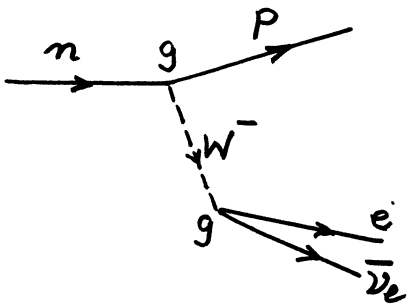

G_F becomes $\frac{g^2}{q^2+m_W^2}$ where q^2 is the four-momentum squared of the W. At low q^2 ($\ll m_W^2$)

$$G_F \sim \frac{g^2}{m_W^2}$$

If g = e (equal electromagnetic and weak coupling)

$$M_W \gtrsim \frac{e}{\sqrt{G}} \quad 100 \text{ GeV/c}^2.$$

According to the standard model

$$M_W = (\pi\alpha/\sqrt{2}\ G_F)^{1/2}/\sin\theta_W$$

where $e^2 = 4\pi\alpha$ and $\alpha = 1/137.032$ at low energy[59]. From neutrino neutral current experiments[60] $\sin^2\theta_W = 0.233 \pm .009$ giving $M_W = 77.2 \pm 1.6$ GeV/c^2. However, at the W-mass both α and $\sin^2\theta_W$ are different (renormalised)[61].

$$\alpha(m_W) = 1/127.7$$

$$\sin^2\theta_W(m_W) = 0.217 \pm 0.014$$

leading to the prediction

$$m_W = 38.65/\sin\theta_W = 83.0 \begin{smallmatrix} + 3.0 \\ - 2.8 \end{smallmatrix} \text{ GeV/c}^2.$$

which is measureably higher, already providing a test of radiative corrections at the present level of experimental study.

In the GSW model, the parameter ρ, which determines the relative strengths of the charged and neutral current couplings is given by

$$\rho = m_W^2/m_Z^2 \cos^2\theta_W$$

If there are only Higgs doublets, $\rho = 1$, i.e. $1/2I_\phi$ where I_ϕ is the Higgs isospin. Therefore $\rho = 1$ in the simplest theory. Using $\sin^2\theta_W(m_W)$ gives

$$M_Z = 93.8 \begin{smallmatrix} +2.5 \\ -2.4 \end{smallmatrix} \text{ GeV/c}^2$$

6.3 Decay of the W and Z

The decays of the W^- are

$$W^- \to \ell\bar{\nu}_\ell$$

$$W^- \to q\bar{q}$$

where $\ell\bar{\nu}_\ell$ is $e\bar{\nu}_e$, $\mu\bar{\nu}_\mu$, $\tau\bar{\nu}_\tau$ and $q\bar{q}$ is $d\bar{u}$, $s\bar{c}$, $b\bar{t}$. The W^+ decays are the charge conjugates. Here we have ignored the Cabibbo type quark mixing but this is not important for calculating the decay width. For each of the three leptonic channels

$$\Gamma(\ W^- \to \ell\bar{\nu}_\ell\ ) = \frac{G_F\ m_W^3}{6\pi\sqrt{2}} = 250 \text{ MeV}$$

The quark channels are the same except for three effects

i) a colour factor of 3

ii) a QCD correction of $(1 + \alpha_s/\pi)$

iii) a phase space factor for $b\bar{t}$[62].

Assuming m_t = 30 GeV/c^2 the total hadronic width is

$\Gamma(W \to \text{hadrons}) = 2.20$ GeV

and $\Gamma(W \to \text{all}) = 2.95$ GeV

Hence $\Gamma(W \to e\nu_e)/\Gamma(W \to \text{all})$ is 8.5% or approximately 1/12. Furthermore the decay is pure V-A. In other words the W decays purely into left-handed leptons or quarks. It is also produced by left-handed quarks. Of course, it couples to right handed antiquarks and antileptons.

The Z decay is more complicated because of mixing with the photon which modifies its vector couplings. Consequently its vector and axial vector couplings are not equal, except for the neutrino decays, and it couples to both left and right handed quarks and leptons.

$$\Gamma_Z = \frac{G_F\, m_Z^3}{24\pi\sqrt{2}} \left[3\sum_q (a_q^2 + v_q^2) + \sum_\ell (a_\ell^2 + v_\ell^2)\right]$$

where v_q(v_ℓ) is the vector coupling to quark (lepton)

a_q(a_ℓ) is the axial coupling to quark (lepton)

and the factor 3 is for colour. According to the model (with the definition that $a_\nu = v_\nu = 1$).

$$v_\ell = 2I_3^\ell - 4Q_\ell \sin^2\theta_W; \quad a_\ell = 2I_3^\ell$$
$$v_q = 2I_3^q - 4Q_q \sin^2\theta_W; \quad a_q = 2I_3^q$$

I_3 is the 3rd component of weak isospin and Q_ℓ, Q_q the lepton and quark charges. Consequently

$$\Gamma(Z \to \nu\bar{\nu}) = \frac{G_F\, m_Z^3}{12\pi\sqrt{2}} = 181 \text{ MeV}$$

$$\Gamma(Z \to \ell^+\ell^-) = 92 \text{ MeV}$$

and, allowing for m_t and the QCD factor

$$\Gamma(Z \to \text{hadrons}) = 2.12 \text{ GeV}$$

$$\Gamma(Z \to \text{all}) = 2.94 \text{ GeV}$$

assuming 3 families of neutrinos. The branching ratio

$$\Gamma(Z \to \ell^+\ell^-)/\Gamma(Z \to \text{all}) = 3.1\%$$

6.4 Production of W and Z; cross sections

The production is analogous to the Drell-Yan mechanism, which has been well studied experimentally[63].

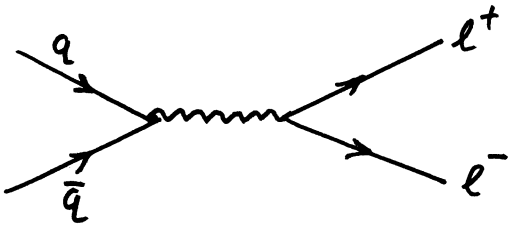

The γ is replaced by a W or Z and there are mass peaks for the final state particles

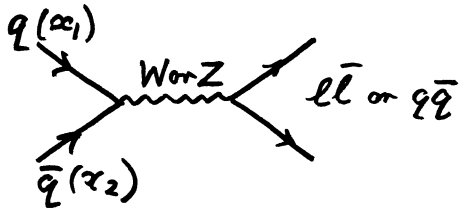

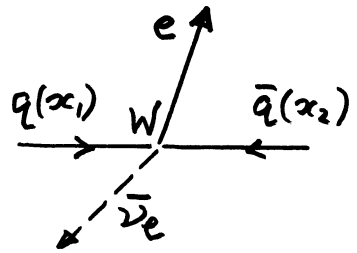

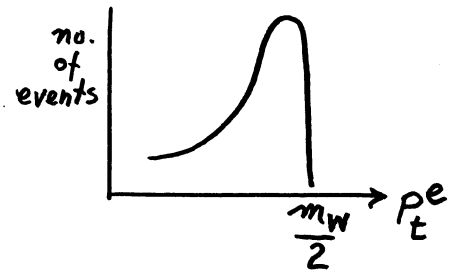

For W decay into $e\bar{\nu}_e$, only the electron is seen and it has a transverse momentum peak at $p_t = m_W/2$, smeared by the finite width of the W, assuming no transverse motion of the W. This is then the characteristic signature of the W. The remaining spectator quarks will, of course, produce additional particles in the event.

The Drell-Yan differential cross section is given by [63]

$$\frac{d^2\sigma}{dx_2 dx_2} = \left(\frac{4\pi\alpha^2}{3M^2}\right) \sum \frac{Q_q^2}{3} \left[q_1(x_1)\bar{q}_2(x_2) + \bar{q}_1(x_1)q_2(x_2)\right]$$

where $q_1(x_1)$ is the probability density of finding a quark of fractional momentum x_1 in hadron 1 etc., and M is the mass of the produced lepton pair. The second factor 3 allows for the fact that the annihilating quark and antiquark have to have the same colour.

For W production we have

$$u\bar{d} \to W^+; \quad u\bar{s} \to W^+$$

$$\bar{u}d \to W^-; \quad \bar{u}s \to W^-$$

where we now include Cabibbo suppressed channels. In this case the differential cross section is

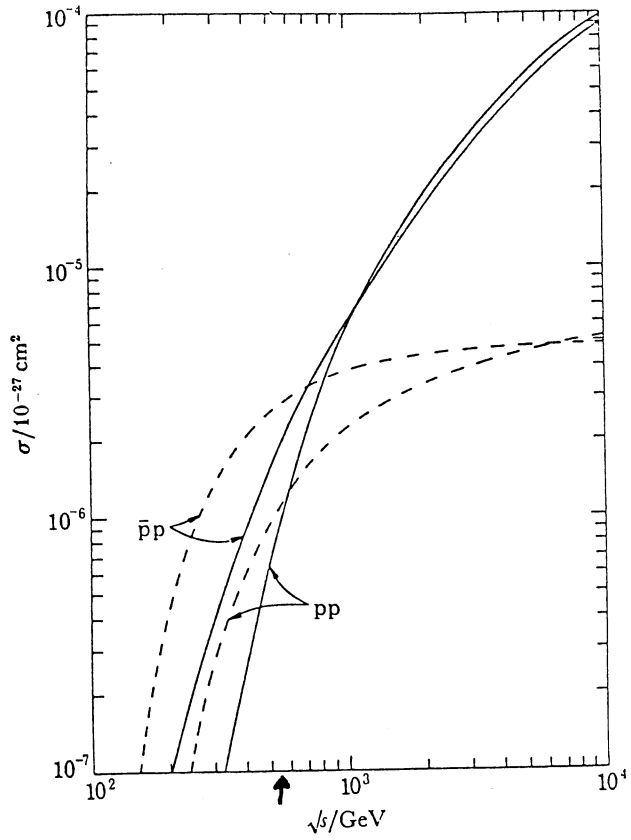

Figure 46 The cross sections for W^+ (or W^-) production versus energy (Paige[64]). The solid curves are for non-scaling quark distributions. The dashed curves are for scaling distributions.

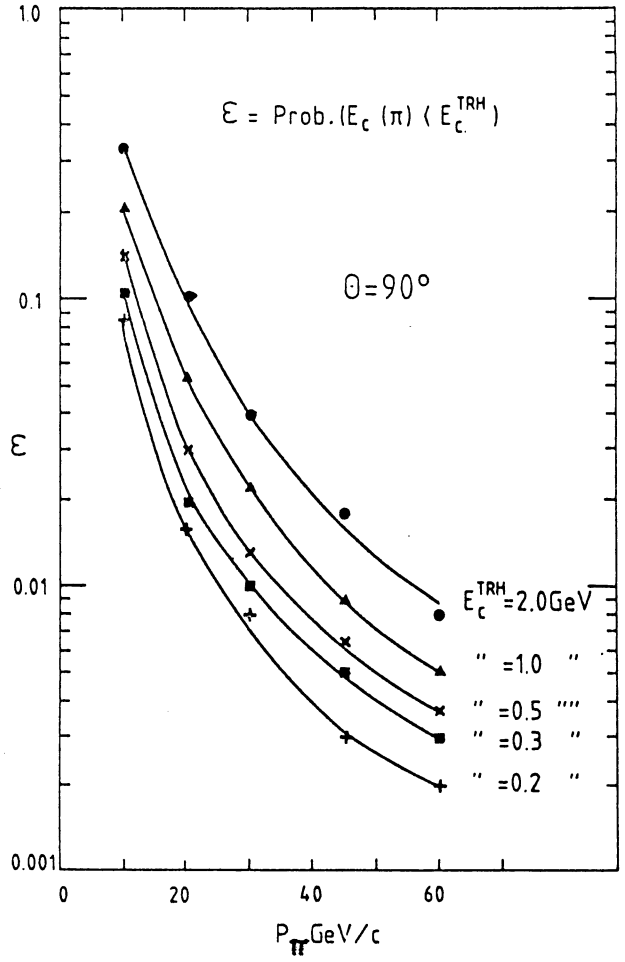

Figure 47 The probability that a pion entering a UA1 electromagnetic calorimeter (gondola) will deposit less than E_C^{THR} in the hadron calorimeter (C) behind it. The data are from test beam measurements. For p_π = 40 GeV/c and E_C^{THR} = 0.2 GeV the probability is 4 x 10^{-3}.

$$\frac{d^2\sigma}{dx_1dx_2} = \frac{\sqrt{2}G_F\pi}{3}\left[\{u_1(x_1)\bar{d}_2(x_2) + \bar{d}_1(x_1)u_2(x_2)\}\cos^2\theta_c + \{u_1(x_1)\bar{s}_2(x_2) + \bar{s}_1(x_2)u_2(x_2)\}\sin^2\theta_c\right]$$

For the Z, only $u\bar{u}$, $d\bar{d}$ and $s\bar{s}$ contribute.

$$\frac{d^2\sigma}{dx_1dx_2} = \frac{\sqrt{2}G_F\pi}{3}\left[\{u_1(x_1)\bar{u}_2(x_2) + \bar{u}_1(x_1)u_2(x_2)\}F_1(\theta_W) + \{d_1(x_1)\bar{d}_2(x_2) + \bar{d}_1(x_1)d_2(x_2) + s_1(x_1)\bar{s}_2(x_2) + \bar{s}_1(x_1)s_2(x_2)\}F_2(\theta_W)\right]$$

where $F_1(\theta_W) = 1/4 - 2/3\ \sin^2\theta_W + 8/9\ \sin^4\theta_W$

$F_2(\theta_W) = 1/4 - 1/3\ \sin^2\theta_W + 2/9\ \sin^4\theta_W$

obtained from the products of the neutral current couplings given above for the charge 2/3 and charge 1/3 quarks respectively. The total cross section is given by

$$\sigma_W = \iint \frac{d^2\sigma}{dx_1dx_2}\,\delta\left(x_1x_2 - \frac{M_W^2}{s}\right)dx_1dx_2$$

with a similar expression for σ_Z, where s is the total centre of mass energy squared.

Figure 46 shows the W and Z cross sections calculated by Paige[64]. The dashed curves are for scaling quark distributions q(x) and the solid curves for non-scaling distributions $q(x,M^2)$ where the q^2 variation is taken into account. At the CERN collider ($\sqrt{s}$ = 540 GeV) there is little difference, but at the Fermilab collider ($\sqrt{s}$ = 2 TeV) the non-scaling functions give a factor 5 higher cross section. Notice that in proton-proton collisions the antiquarks are from the sea which means that proton-antiproton collisions are more favourable close to threshold.

The predicted W^+ cross section at 540 GeV is 2-3 nb, or about 0.2 nb for $W^+ \to e\nu$.

6.5 Higher order corrections to the cross sections

The above calculations are to lowest order in QCD. Higher order processors not only increase the cross sections but also give transverse momentum to the W or Z. Examples of first order diagrams (in α_s) are:-

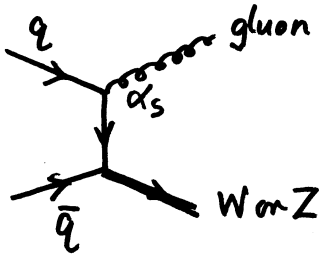

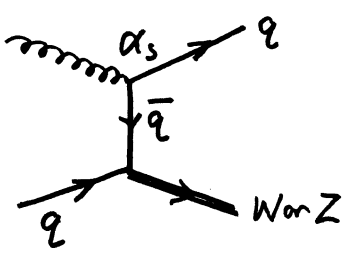

Their effect has been calculated[65]. The cross sections are increased by approximately a factor of 2 - the K factor, observed experimentally in Drell-Yan[63]. p_t values, for the W and Z, averaging several GeV are expected (see later) as well as observable recoil jets. The p_t distribution of the electron in W-decay is further smeared out, but not seriously.

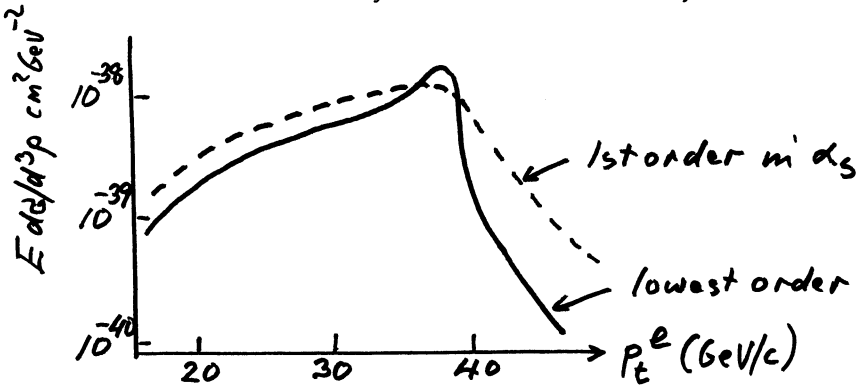

6.6 Experimental considerations (W-reconstruction from W → eν and W → μν events)

In UA1 and UA2 the momentum of the electron (or muon) is measured - in fact, for the electron, it is the energy and direction since the calorimeter measurement is much more precise (~± 2%). However, for the neutrino, only the transverse energy (i.e. the missing transverse energy in the event) is measured because part of the total energy (~100 GeV) escapes along the beam pipe. For ordinary hadronic events one expects the transverse components to be balanced. The decay lepton from the W is expected to be isolated (i.e. not part of a jet).

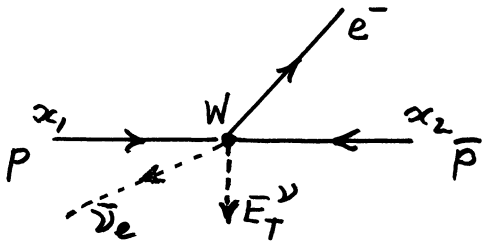

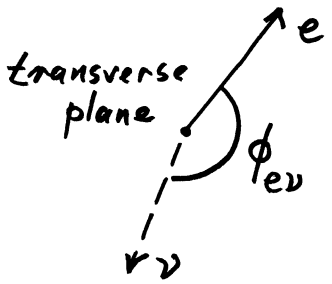

The W mass cannot be calculated but the transverse mass m_T ($\leq m_W$) can be found where

$$m_T^2 = 2p_t^e\, p_t^\nu\, (1-\cos\phi_{\nu e})$$

and $\phi_{\nu e}$ is the angle between the ν and e directions in a plane perpendicular to the beam direction (transverse plane). It is easily shown that m_T is independent of p_t^W to first order in p_t^W. Nevertheless it is necessary to assume a p_t distribution for the W (given by QCD) and a decay angular distribution in the W centre of mass in order to find m_W which is done by a Monte Carlo fitting procedure.

If $p_t^W = 0$, $p_t^e = \frac{m_W}{2} \sin\theta^*$: the decay angular distribution is $(1+\cos\theta^*)^2$. The calculation is then straight-forward[66].

The measurement of p_t^e only determines θ^*, the centre of mass decay angle, with a sign ambiguity: i.e. $\cos\theta^* = \pm\sqrt{1-\sin^2\theta^*}$. In the majority of the cases it is possible to solve this 2-fold kinematic ambiguity.

For a given value of θ_{lab} for the electron, which determines p_t^e, there are two values of $x_W = 2p_L^W/\sqrt{s}$ corresponding to the two signs for $\cos\theta^*$, or equivalently there are two possible directions for the neutrino. In about 70% of the cases one of the solutions for x_W is unphysical (> 1) and the other solution is unique. This is relevant in the study of the decay asymmetry discussed later. Furthermore x_1 and x_2 are then also determined using the fact that

$$m_W = x_1 x_2 s; \quad x_W = x_1 - x_2$$

6.7 Backgrounds to W events

There are several sources of background for $W \to e\nu(\mu\nu)$

i) misidentified electrons (or muons), i.e. a pion giving an energy deposition in the electromagnetic calorimeter like an electron (figure 47) (or a hadron "punching through" the calorimeters).

ii) photon overlap with a charged particle simulating an electromagnetic response in a calorimeter.
- UA1 compare the central detector momentum for the track with the energy in the calorimeter
- UA2 compare the impact point of the track and the photon (UA1 also does this).

iii) Asymmetric Dalitz pairs and conversions in the apparatus.

iv) Genuine electron or muon from heavy quark decays ($b\bar{b}$ principally). In the case of muons, also $\pi\to\mu$ and $K\to\mu$ decays.

v) Genuine $W \to \tau\nu_\tau$ events; $\tau \to e\nu_e\nu_\tau$ or $\pi^+\pi^o\nu_\tau$. This gives electrons or fake electrons and missing energy but with lower p_t.

All of the processes i) to iv) give an "electron" spectrum that decreases with increasing p_t. Therefore a p_t cut on the electron helps to remove the background. The striking feature of the data, however, is the large missing energy in W events that is not present in the background processes and proves to be an extremely powerful way of rejecting background events, resulting in quite small backgrounds.

Figure 48 shows the missing transverse energy for 55 single electron events with $p_t^e > 15$ GeV/c in UA1[67]. The dashed curve is the resolution function for missing energy, obtained from ordinary events, normalised to the three lowest missing energy events. Empirically[67], each component of missing transverse energy has an error $\Delta E_{y,z} = 0.4\sqrt{\sum E_T}$. To avoid the effect of 'cracks' at the top and bottom of the magnet, regions where the missing energy 'vector' is within $\pm 15^o$ of the vertical are excluded reducing the sample to 43 events for further study.

If they originate from W decays, there should be a strong correlation between the

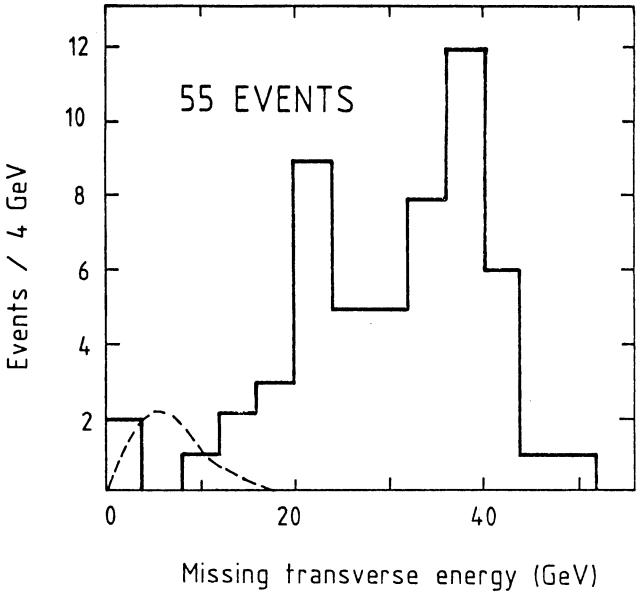

Figure 48. A plot of the missing transverse energy for single electron events with $p^e_t > 15$ GeV/c (UA1). The dashed curve is the resolution function for missing energy normalised to the three lowest missing energy events.

Figure 49. A plot of the electron transverse energy against the parallel component of neutrino transverse energy showing a striking correlation as would be expected for W decays.

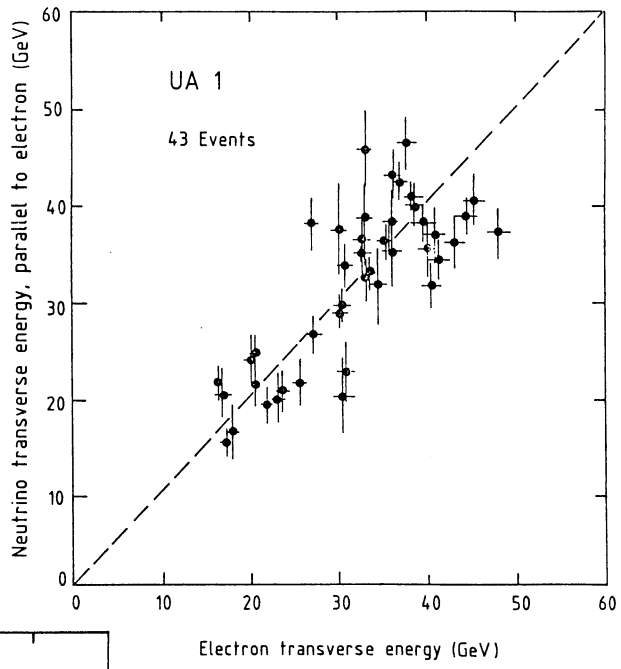

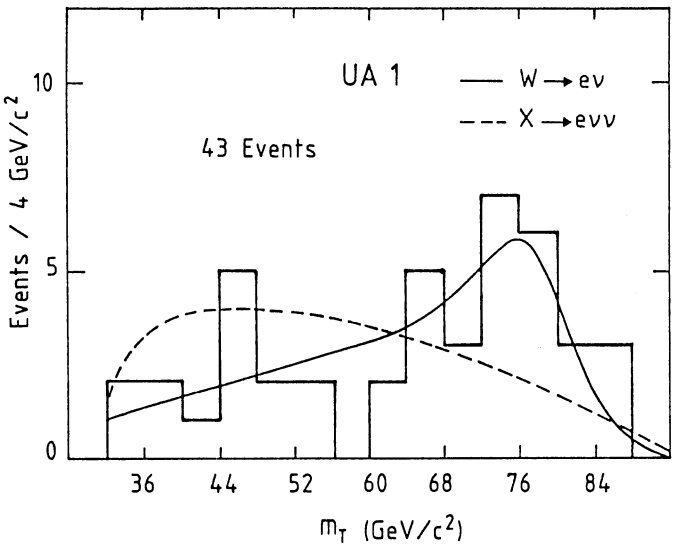

Figure 50. The transverse mass distribution for eν events. The solid curve is a fit for $m_W = 80.9$ GeV/c^2. The dashed curve is the expected shape for an object decaying into eνν.

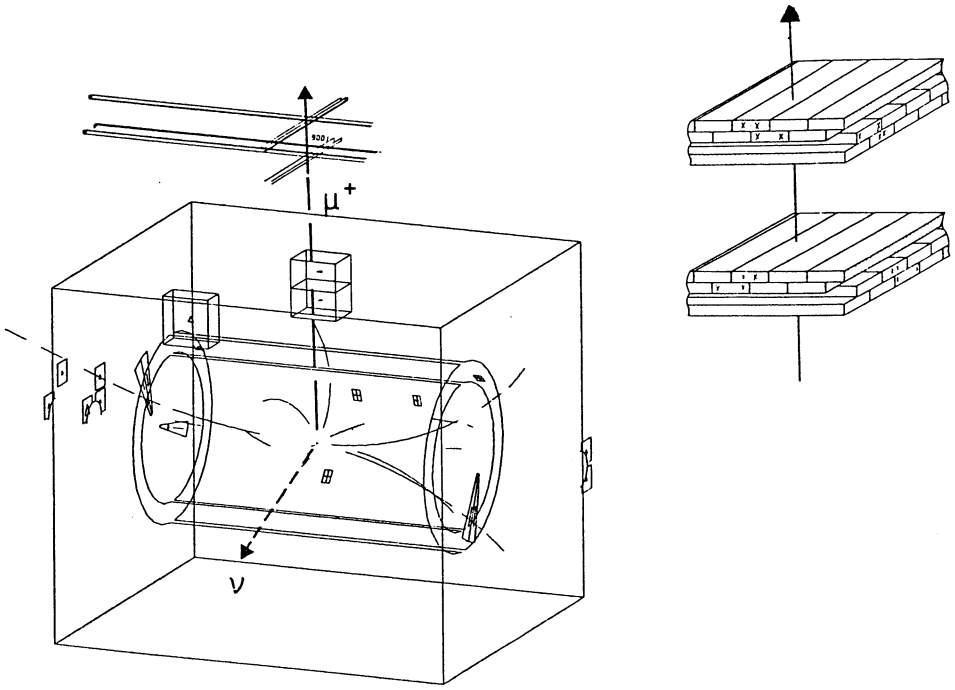

Figure 51 An example of a W → μν event. The struck muon drift tubes are indicated and the hadron calorimeter cells. The dashed arrow is the direction of the missing transverse energy.

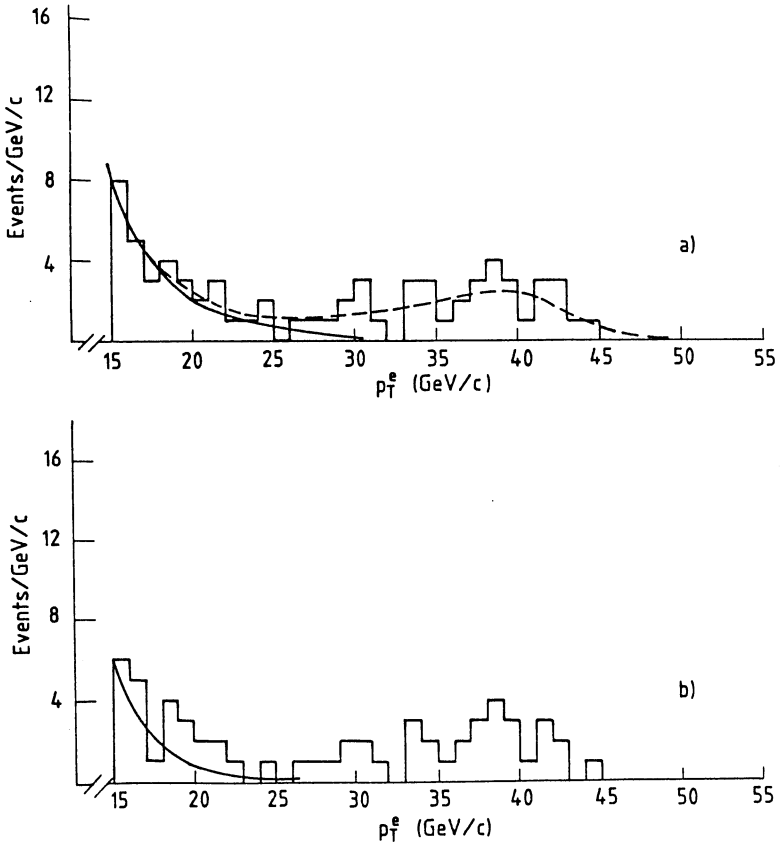

Figure 52. UA2 experiment a) the p_t distribution of the electron in the W → eν sample b) the same with strict cuts on the central detector. The full curves are background estimates and the dashed curve background + W → eν + W → τν (τ → eνν). The fitted mass is 83.1 GeV/c^2.

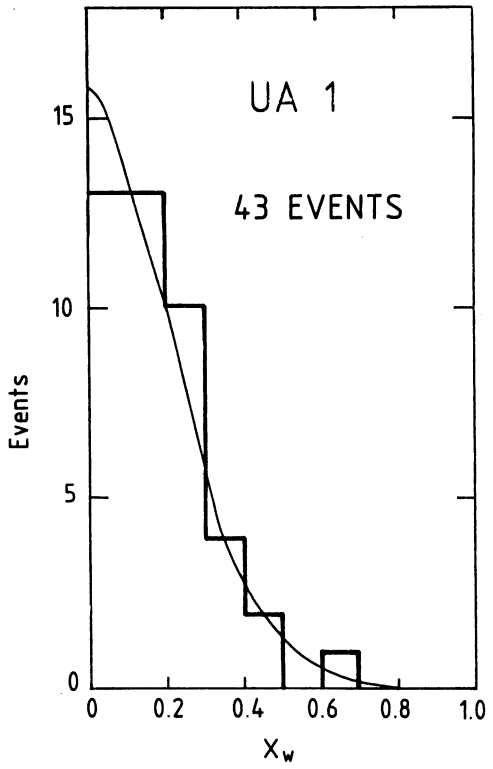

Figure 53. The fractional energy x_W carried by the W. The curve is the prediction assuming the W has been produced by valence quarks and antiquarks.

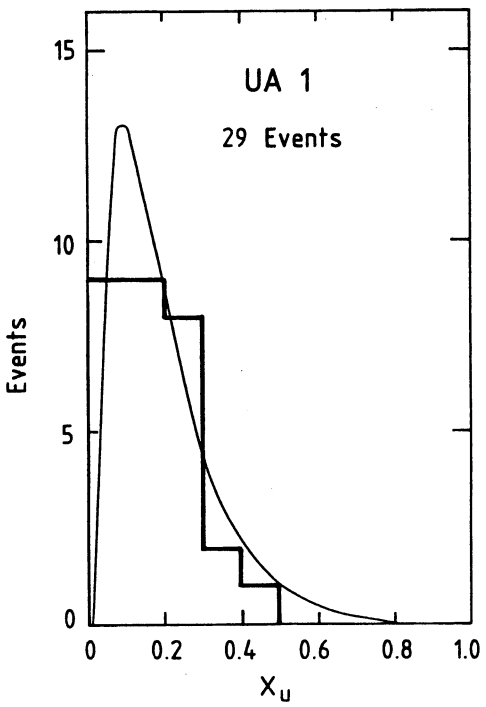

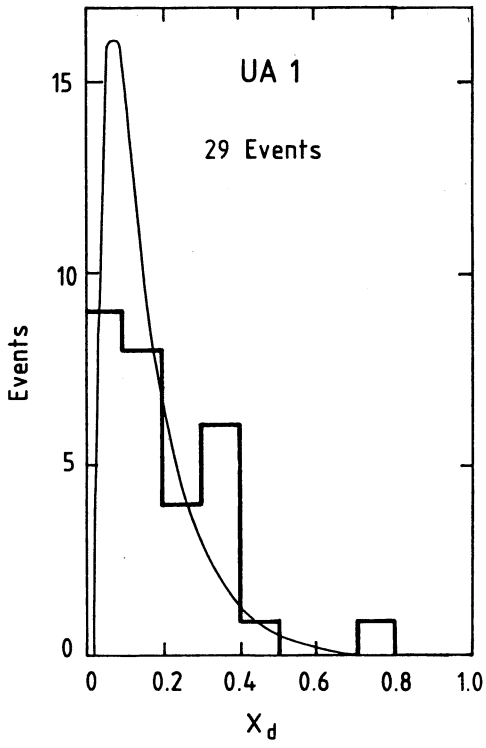

Figure 54. The x-distributions of $u(\bar{u})$ and $d(\bar{d})$ quarks in the proton (antiproton) for events where the W charge is determined.

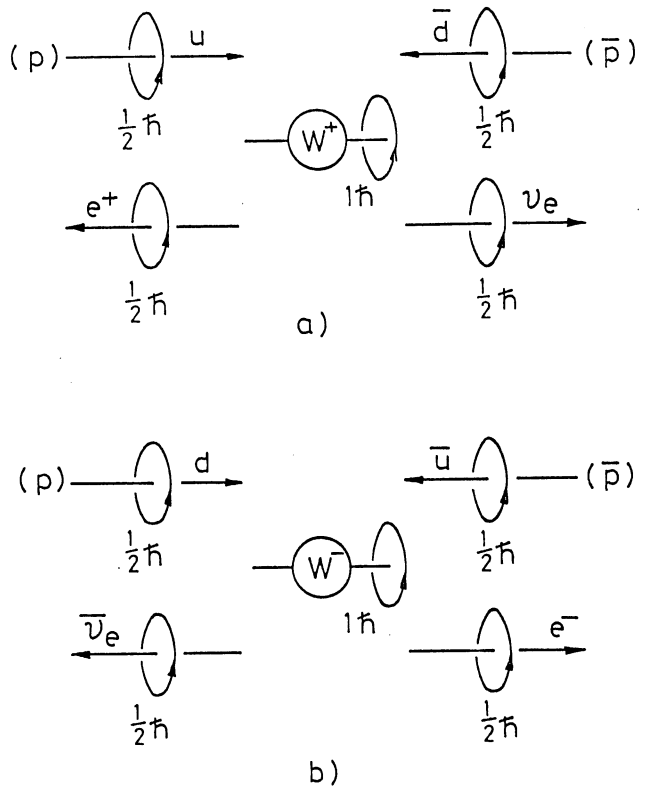

Figure 55. Production and decay of W^+ and W^- showing the behaviour of the particle spins. For example the W^+ is formed from left-handed quarks (proton) and right-handed antiquarks (antiproton). It decays to a right- handed e^+ and a left-handed νe which are constrained to travel in the directions shown to conserve angular momentum giving rise to a $(1 + \cos\theta^*)^2$ angular distribution.

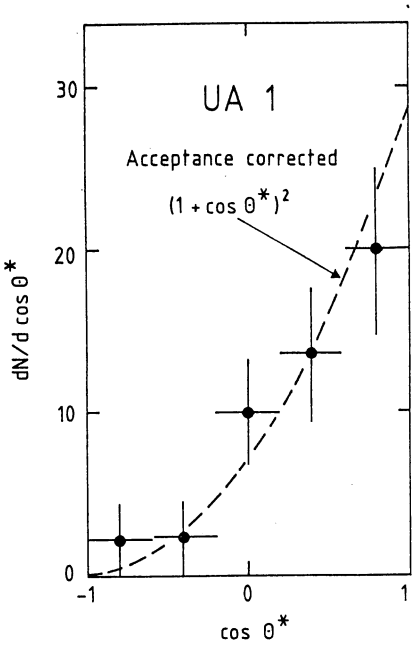

Figure 56. The W decay asymmetry observed in the UA1 experiment.

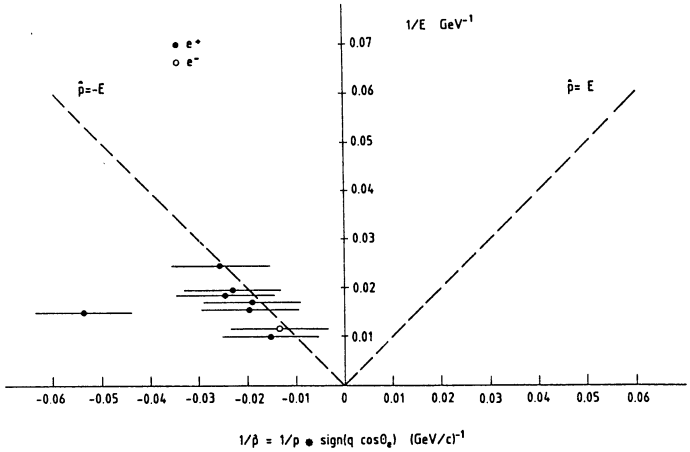

Figure 57. The asymmetry for W decays in UA2 using the forward toroidal spectrometers to measure the electron charge.

electron and neutrino transverse energies which should balance on average. Figure 49 shows that this behaviour is observed. Note that $W \to \tau\nu_\tau$ events lie on the same line. It is estimated that the plot contains <0.5 event where $\tau \to \pi\ \pi^o\nu_\tau$ and 2 events where $\tau \to e\nu_e\nu_\tau$ which necessarily have low p_t values for the electrons. Figure 50 shows the transverse mass distribution for the 43 events. The solid curve is the best fit to the W mass and the dashed curve is the expectation for a hypothetical particle of the same mass decaying to $e\nu\nu$. Actually, the mass was determined from events with p_t^e, $p_t^\nu > 30$ GeV/c to eliminate τ-backgrounds, and yielded a value

$$m_W = 80.9 \pm 1.5 \text{ (stat.)} \pm 2.4 \text{ (syst.) GeV/c}^2$$

The systematic error arises from the uncertainty on the absolute energy calibration of the electromagnetic calorimeters (± 3%).

UA1[68] has also observed 14 examples of $W \to \mu\nu$ (see figure 51) from which $m_W = 81.0^{+6}_{-7}$ GeV/c. The statistical error is larger because momenta have to be measured by the magnetic field and the number of events smaller because of lower geometrical acceptance and overall running time with a muon trigger. For full details see reference 68. Figure 52 shows the $W \to e\nu$ sample from UA2 in which the electron transverse momentum is plotted[69]. One can clearly see the falling background spectrum. The dashed curve is a fit for background + $(W \to e\nu)$ + $(W \to \tau\nu, \tau \to e\nu\nu)$. The fit gives 32.1 ± 6.0 $W \to e\nu$ decays yielding

$$m_W = 83.1 \pm 1.9 \pm 1.3 \text{ GeV/c}^2$$

The systematic error is lower than in UA1.

6.8 Longitudinal motion of the W

As already discussed the Feynman x of the W can be found with a 2-fold ambiguity. In 70% of the cases one solution is unphysical. In the remaining 30% the lower value is used. Figure 53 shows x_W for the 43 events[67] compared to a curve obtained using u and d quark distributions varying as $x(1-x)^3$ and $x(1-x)^4$ respectively. In 29 of the events the electron charge is determined to 3σ and one can actually obtain x_u and x_d which are shown in figure 54, together with the curves mentioned above. It is assumed that only valence quarks participate, otherwise the analysis would be impossible.

6.9 Decay asymmetry of $W \to e\nu$

The full reconstruction of the W production and decay is a necessary first step in determining the decay asymmetry which obviously requires a unique knowledge of $\cos\theta^*$. The left-handed coupling of the W arising from the pure V-A form of the theory leads to an angular distribution of $(1+\cos\theta^*)^2$. This is easily understood through a helicity argument (figure 55). The Ws are longitudinally polarised provided only valence quarks are involved. Figure 56 shows the UA1 result which is in excellent agreement with expectations. Figure 57 shows the results from UA2, obtained from their forward toroidal spectrometers[69]. Note that in pp collisions there is no asymmetry since the antiquark must come from the sea.

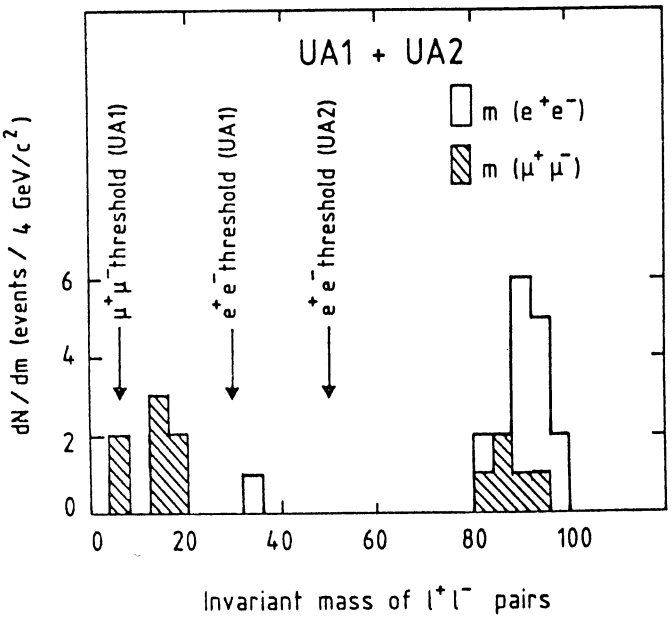

Figure 58. Mass plot of $\ell^+\ell^-$ pairs from UA1 and UA2 showing a clear Z^o mass peak containing 5 $\mu^+\mu^-$ and 12 e^+e^- events. The background is obviously negligible.

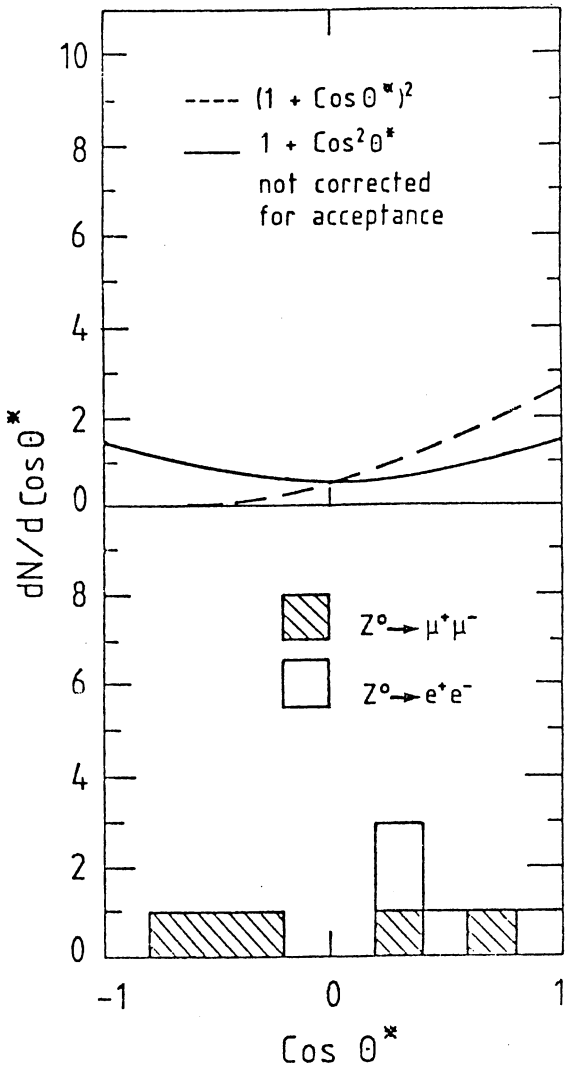

Figure 59. The Z^o decay angular distribution in the UA1 experiment. The expected asymmetry is very small because of the small vector coupling. The data are consistent with this behaviour.

Table 4

$W^{\pm}$ and Z^{o} parameters from the UA1 and UA2 experiments

	UA1	UA2
$N(W \to e\nu)$	52[a]	37[b]
$m_W(GeV/c^2)$	$80.9 \pm 1.5 \pm 2.4$	$83.1 \pm 1.9 \pm 1.3$
Γ_W(90%CL)	< 7 GeV	-
(σB)(nb)	$0.53 \pm 0.08 \pm 0.09$	$0.53 \pm 0.10 \pm 0.10$
$N(W \to \mu\nu)$	14	-
$m_W(GeV/c^2)$	81.0^{+6}_{-7}	-
(σB)(nb)	$0.67 \pm 0.17 \pm 0.15$	-
$N(Z^o \to e^+e^-)$	3+1[c]	7+1[c]
$m_{Z^o}(GeV/c^2)$	$95.6 \pm 1.4 \pm 2.9$	$92.7 \pm 1.7 \pm 1.4$
Γ_{Z^o}(90%CL)	< 8.5 GeV	< 6.5 GeV
(σB)(nb)	$0.05 \pm 0.02 \pm 0.009$	$0.11 \pm 0.04 \pm 0.02$
$N(Z^o \to \mu^+\mu^-)$	4+1[c]	-
$m_{Z^o}(GeV/c^2)$	85.6 ± 6.3	-
(σB)(nb)	$0.105 \pm 0.05 \pm 0.15$	-
$\sin^2\theta_W = (38.65/m_W)^2$	$0.228 \pm 0.008 \pm 0.014$	$0.216 \pm 0.010 \pm 0.007$
$\rho = [m_W/m_Z \cos\theta_W]^2$	0.97 ± 0.05	1.02 ± 0.06

a) $p_T > 15$ GeV/c

b) $p_T > 25$ GeV/c

c) $Z^o \to \ell^+\ell^-\gamma(E_\gamma > 20$ GeV)

[Averaging the electron and muon results for UA1 gives $m_W = 80.9 \pm 1.5 \pm 2.4$ GeV/c^2; $m_Z = 93.5 \pm 1.5 \pm 2.9$ GeV/c^2].

6.10 Z^o production

As two charged leptons result from the decay of the Z, the events are extremely clean as can be seen from a simple mass plot (figure 58). Consequently, no background discussion is necessary. UA1 has observed $4e^+e^-$ and 5 $\mu^+\mu^-$ events[70,75] while UA2[71] has 8 e^+e^- events. However 3 of them have hard γ-rays at appreciable angles to the leptons which cannot easily be accounted for as bremsstrahlung and will be discussed later. The results for Z masses are summarised in table 4 together with the W masses from the two experiments.

The Z decay angular distribution is expected to be almost symmetric because of the small vector coupling of the Z to electrons, $(1-4\sin^2\theta_W)$. The almost pure axial vector nature of the decay leads to equal couplings to left and right handed electrons which, according to the helicity argument, gives no significant asymmetry (figure 59).

6.11 Comparison with the Standard Model

Table 4 summarises the results of the two experiments for the W and Z masses, widths and cross sections. The values of $\sin^2\theta_W(m_W)$ obtained from $(38.65/m_W)^2$ (6.2) and the values of $\rho = (m_W/m_Z \cos\theta)^2$ are also given for each experiment. The results for $\sin^2\theta_W$ are in excellent agreement with the prediction of 0.217 ± 0.014 and ρ is compatible with unity as expected for Higgs doublets. Furthermore, the cross sections (x branching ratios) are in satisfactory agreement with QCD calculations[65], in view of the theoretical uncertainties, the predicted values being $\sigma B(W \to e\nu) = 0.39$nb and $\sigma B(Z \to e^+e^-) = 0.04$nb.

An alternative way of comparing the results with the standard model is to assume that $\rho = 1$ in which case $\sin^2\theta_W(m_W) = 1 - m_W^2/m_Z^2$. One may then test radiative corrections using

$$m_W = \frac{A}{\sin\theta_W}$$

where $A = \dfrac{37.2810 \pm 0.0003}{(1-\Delta r)^{1/2}}$ GeV

i.e. the low energy value with a correction term Δr. Hence

$$\Delta r = 1 - \frac{37.2810^2}{m_W^2(1-m_W^2/m_Z^2)}$$

The results are the following:-

	Δr
Theory	$+ 0.070 \pm 0.002$
UA1	$+ 0.16 \pm 0.11 \pm 0.05$
UA2	$- 0.03 \pm 0.24 \pm 0.03$

assuming that the systematic errors cancel on m_W/m_Z. There is agreement within statistics but the test is clearly not definitive.

What might one expect in the future? The improved collider, equipped with the new antiproton collector ring ACOL, is expected to give an improvement of a factor 10 in antiproton flux ($\sim 10^{11}$ per bunch).

Together with the higher energy of around 330 GeV per beam one can expect perhaps a factor 20 increase in W and Z yields. Three years of running (1987-9) should then produce $\sim 10^4$ $W \to e\nu$ and $\sim 10^3$ $Z \to e^+e^-$ in the two experiments together. Systematic errors on the W and Z masses should be $< 1\%$ in both experiments which corresponds to accuracy of ± 0.005 or $\sin^2\theta_W$ such as is planned in the CHARM II experiment[72]. The error on m_W/m_Z should be $< 0.2\%$ giving

$$\Delta r = 0.070 \pm 0.013(\text{stat.}) \pm 0.018(\text{syst.})$$

where we have inserted the theoretical value for Δr (whose error is ± 0.002). However a more accurate measurement of m_Z from SLC or LEP would greatly reduce the systematic error. Thus one can hope to check radiative corrections to about $\pm 20\%$.

We note that the error from the collider on Γ_Z should be ± 250 MeV corresponding to 2 extra neutrinos at 90% confidence level.

6.12 Z-width and number of neutrino families

Each additional neutrino family increases the Z-width by 0.18 GeV but the direct measurements are not at this level of sensitivity (UA1 finds $N_\nu < 31$ and UA2 $N_\nu < 22$ with 90% confidence level).

A better result is obtained indirectly from

$$\sigma B_{Z \to e^+e^-} / \sigma B_{W \to e\nu} = \frac{\sigma_Z}{\sigma_W} \left(\Gamma_{Z \to e^+e^-} / \Gamma_{W \to e\nu} \right) \frac{\Gamma_W}{\Gamma_Z}$$

which requires a knowledge of σ_Z/σ_W from QCD and $\Gamma_{Z \to e^+e^-}$, $\Gamma_{W \to e\nu}$ and Γ_W from theory. This assumes no heavier charged lepton that the W can decay into. $\frac{\sigma_Z}{\sigma_W} = 0.24 \pm 0.05$ from QCD and should be fairly reliable as most corrections are common to both cross sections.

From UA1 $$\sigma B_Z/\sigma B_W = 0.098 \begin{matrix} + 0.052 \\ - 0.035 \end{matrix}$$

giving $\Gamma_Z = 1.8 \begin{matrix} + 5.5 \\ - 1.1 \end{matrix}$ GeV and $N_\nu < 18$ (90% c.l.)[58]. In a similar analysis UA2[69] finds $\Gamma_Z < 2.6 \pm 0.3$ GeV and $N_\nu < 3$ (90% c.l.), the low value stemming from their rather high Z cross section. However with the present statistics neither result is very interesting. Furthermore there are the questions of whether the radiative decays of the Z should be included or not and the value of m_t that should be used. The limit from cosmological constraints[58] is $N_\nu < 4$.

6.13 Transverse momentum of the W and Z

As discussed earlier (6.5) QCD corrections to the simple Drell-Yan type diagram produce appreciable p_t-values for the W and Z as well as observable jets. Several authors have calculated the expected p_t-distributions which are compared with the data in figures 60 and 61. Good agreement is found. Furthermore UA1 have compared the jet E_T distributions for W and Z events to those from multijet data[74], which shows them to be consistent with initial state gluon bremsstrahlung (figure 63). However there is some

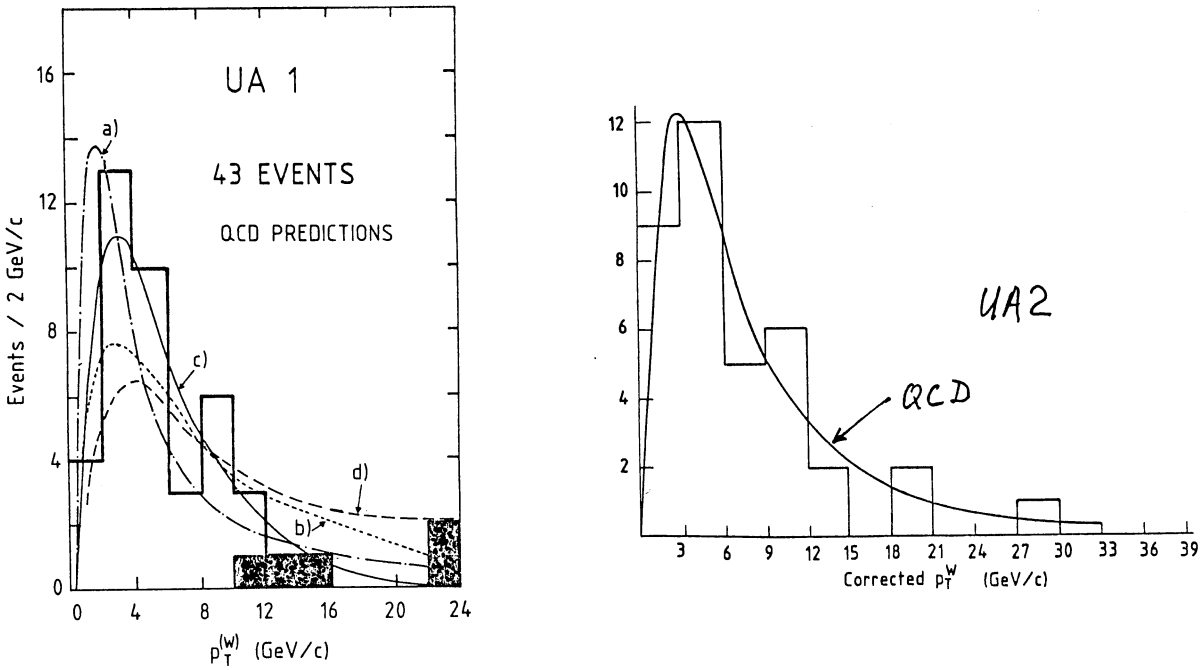

Figure 60 p_t distributions of the W compared to QCD predictions[73].

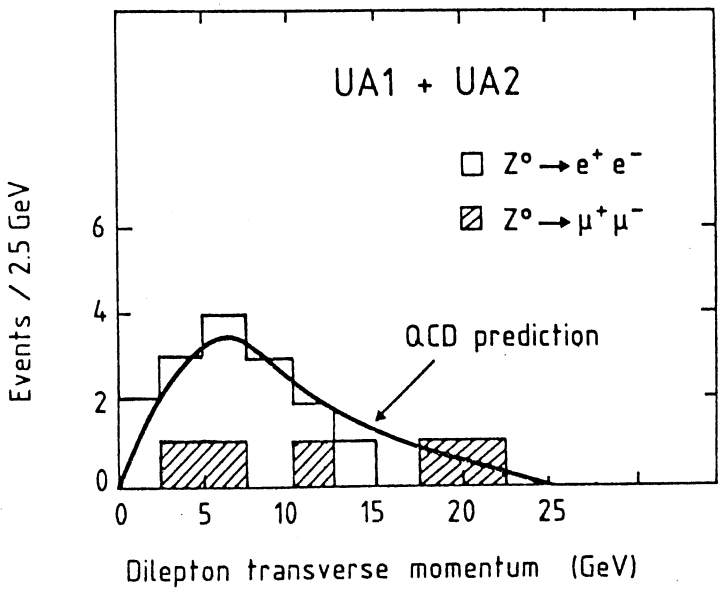

Figure 61 p_t distribution of the Z compared to a QCD prediction[73].

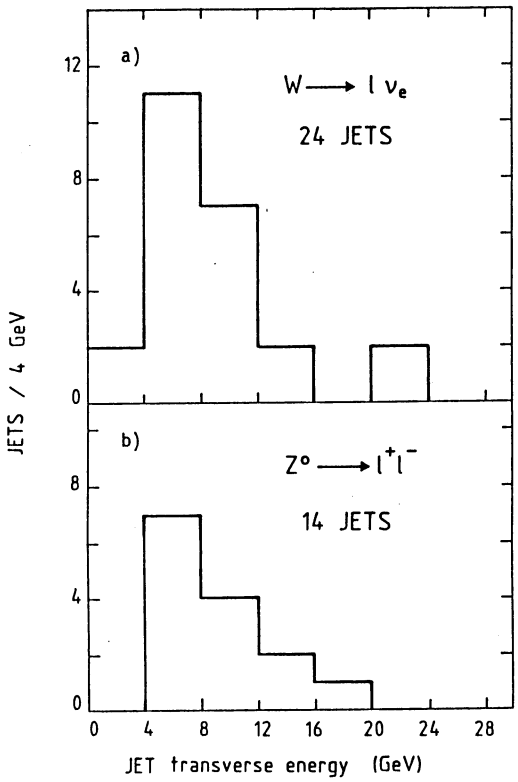

Figure 63 Jet E_T distributions for
a) 66 W → ℓν events,
b) 9 Z → $\ell^+\ell^-$ events.

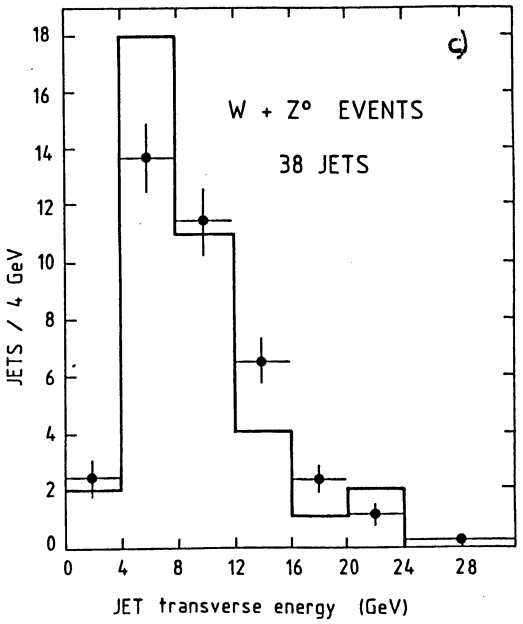

Figure 63 c) Jet E_T distributions for 75 W and Z events (histogram) compared to 'extra' QCD jets.

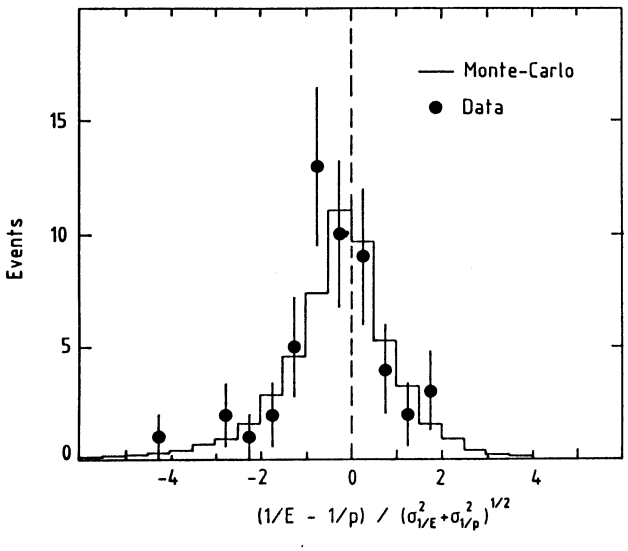

Figure 64 a) Comparison of 1/E and 1/p for W decay electrons and the expected behaviour.

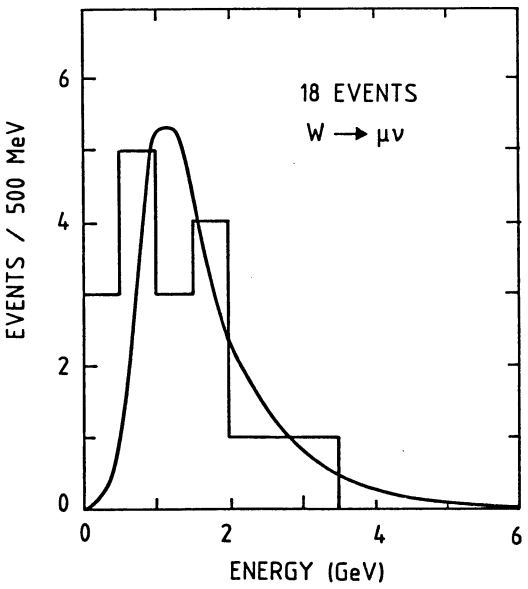

Figure 64 b) Energy deposition of W decay muons in the calorimeters compared to expectation.

Table 5

Properties of the $\ell^+\ell^-$ events

	$e^+e^-\gamma$(UA1)	$e^+e^-\gamma$(UA2)[a]	$\mu^+\mu^-\gamma$(UA1)
E_γ(GeV)	38.8±1.5	24.4±1.0	28.3±3
E_{ℓ^+}(GeV)	61.0±1.2	69.9±1.8	$50.6^{+5.8}_{-4.7}$
E_{ℓ^-}(GeV)	9±1	11.5±0.7	$42.2^{+44.0}_{-14.3}$
$\Delta\alpha(\ell^+,\gamma)(^o)$[b]	132.0±4.0	129.9	7.9
$\Delta\alpha(\ell^-,\gamma)(^o)$[b]	14.4±4.0	31.8	99.0
$m(\ell^+\ell^-)$(GeV/c^2)	42.7±2.4	50.4±1.7	$70.9^{+37.2}_{-12.4}$
$m(\ell^+\ell^-\gamma)$(GeV/c^2)	98.7±5.0	90.6±1.9	$88.4^{+46.1}_{-15.2}$
$m(\ell^+\gamma)$(GeV/c^2)	88.8±2.5	74.7±1.8	5.0±0.4
$m(\ell^-\gamma)$(GeV/c^2)	4.6±1.0	9.1±0.3	$52.5^{+27.5}_{-9.3}$

a) The e^+ is identified since it goes into the forward region; the charge of e^- is unknown.

b) $\Delta\alpha$ is the angular difference in space.

evidence for a higher jet multiplicity for Z events (figure 63) though this is not seen in UA2 and therefore needs confirmation.

6.14 Summary of W and Z Physics compared to the Standard Model

In summary the following features have been observed within experimental errors:

i) correct W and Z masses ($\rho = 1$)
ii) correct W and Z rates
iii) correct decay asymmetries
iv) μ-e universality
v) agreement with QCD for p_t-distributions.

On the other hand there are two unexpected features requiring confirmation:-

- Evidence for radiative Z-decays. These will be discussed further in section 7.1.
- Possible anomalous jet activity on Z-events.

7. NEW PHENOMENA

7.1 Introduction

In this section we shall discuss a number of miscellaneous topics, some of which may indicate phenomena that are not explicable within the framework of QCD and the electroweak model. They are:

1. Radiative Z decays
2. Charm production in jets (UA1)
3. Dimuon events (UA1)
4. High mass eν Jet events (UA2)
5. Monojets or γs with missing E_T (UA1)
6. Evidence for the top quark (UA1)

Finally, we discuss the future prospects at the $\bar{p}p$ collider in the search for Higgs mesons.

7.2 $Z \to \ell^+\ell^-\gamma$ events.

Two events in UA1 ($e^+e^-\gamma$ and $\mu^+\mu^-\gamma$)[70],[75] and one in UA2 ($e^+e^-\gamma$)[71] have been observed in which a hard γ carries off a large fraction of the energy of one of the leptons and is at an appreciable angle $\Delta\alpha$ to it. The details are presented in Table 5. All three events are consistent with Z decays. The most obvious explanation would be that the γ-rays are bremsstrahlung, either internal, or due to radiation in the apparatus. However, the probability of observing a γ with $F = E_\gamma / (E_\gamma + E_e)$ greater than that observed and $\Delta\alpha$ greater than that observed is $\lesssim 1\%$ in each case. Even when multiplied by the total number of lepton tracks, each of which could in principle radiate a γ, the probability of observing three such events is still less than 1%. In fact Barger et al.[76] estimate that (for $E_\gamma > 15$GeV, $\Delta\alpha > 10^o$)

$$\Gamma(Z^o \to e^+e^-\gamma)/\Gamma(Z^o \to e^+e^-) \sim 1.6\%$$

for inner bremsstrahlung using the Sterman-Weinberg formula[77]. This has to be compared with three events out of seventeen making the bremsstrahlung explanation quite unlikely ($\lesssim$ 0.3 event expected).

A similar study has been performed by Berends et al.[78] which takes into account the experimental conditions and gives an upper limit of 0.1 event (95% confidence level) for

the expected bremsstrahlung rate with $F \geq F_{obs}$ and $\Delta\alpha \geq \Delta\alpha_{obs}$.

7.3 Search for $W \to \ell\nu\gamma$

Both UA1[79] and UA2[80] have carried out careful searches for $W \to \ell\nu\gamma$. UA1 has found no events out of a sample of 55 $W \to e\nu$ and 18 $\to W \to \mu\nu$. UA2 has one $W \to e\nu\gamma$ event out of 37, but this occurs in the forward region and has a 4.5% probability of being a bremsstrahlung on the observed event. Furthermore the characteristics of the UA1 events, in terms of momentum-energy comparisons for electrons and energy loss in the calorimeters for muons, are entirely consistent with conventional behaviour (figure 64).

7.4 Possible explanations of the $Z \to \ell^+\ell^-\gamma$ events

Many authors[81-83] have considered alternative explanations for the events which, including bremsstrahlung, fall into four main classes

i) Bremsstrahlung

ii) Composite W, Z[81]

iii) Excited leptons[82]

iv) Anomalous $ZZ\gamma$ or $Z\gamma\gamma$ couplings[82].

7.4.1 Composite W, Z[81]

The basic idea is that the W and Z are not elementary but are composed of spin 1/2 or spin 0 constituents α, β giving rise to

$$W^+, W^o, W^- = \bar{\beta}\alpha, \frac{\bar{\alpha}\alpha - \bar{\beta}\beta}{\sqrt{2}}, \bar{\alpha}\beta$$

$$V^o = \frac{\bar{\alpha}\alpha - \bar{\beta}\beta}{\sqrt{2}}$$

For spin 1/2 constituents these would be $^3S_1$ states, mathematically analogous to ρ, ω. The Z^o would be a mixture of W^o, V^o. ^1S_o states X^+, X^o, X^- and U^o would also occur. The hard γ rays would then result from transitions between Z^o and U^o, the U^o subsequently decaying into $\ell^+\ell^-$. The non-observation of U^o at PETRA places its mass greater than 47 GeV.

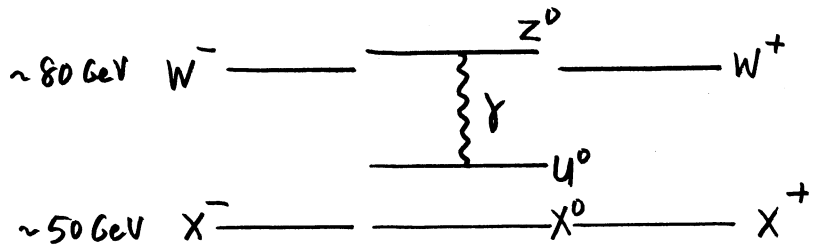

Decays of $W^{\pm} \to X^{\mp}\gamma$ and $Z^o \to X^o\gamma$ are approximately forbidden in this scheme.

For M_U = 50 GeV an 8.4% $e^+e^-\gamma/e^+e^-$ ratio is expected with spin 1/2 constituents and 6.7% with spin 0 constituents. The scheme would also predict $\gamma\nu\nu$ and γJJ decays each at a several times higher rate. The difficulty is that the γ is not correlated with either

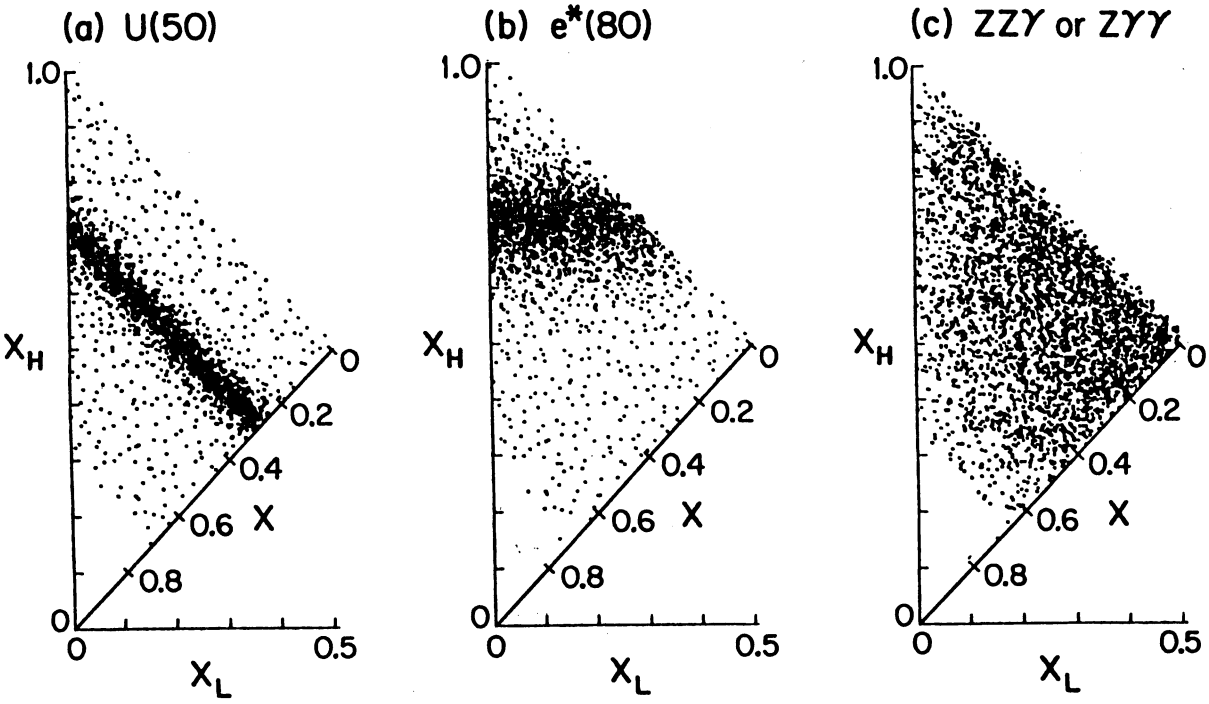

Figure 65 Dalitz plots according to various hypotheses for $Z \to \ell^+\ell^-\gamma$ events a) composite Z, b) excited lepton, c) anomalous couplings,

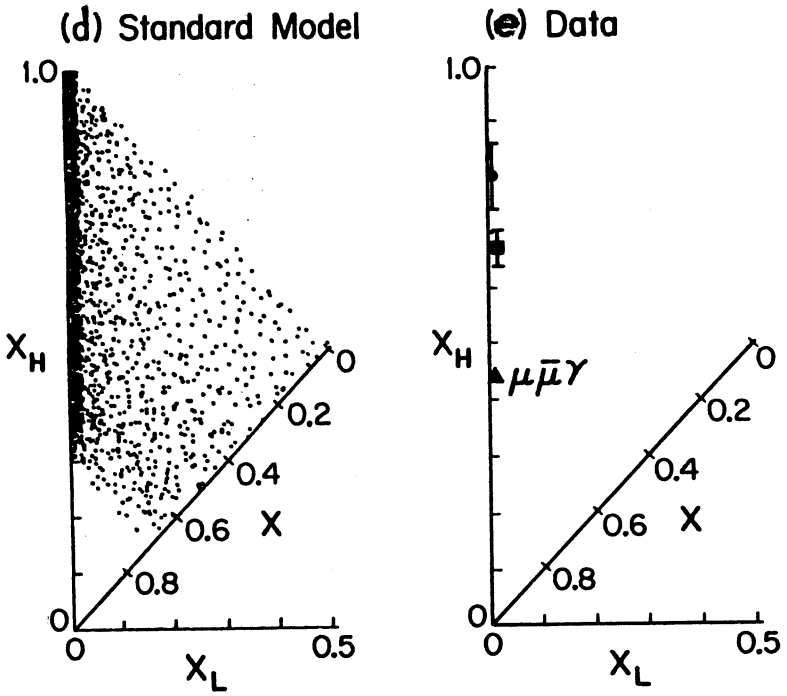

d) Bremsstrahlung, e) actual events.

lepton. The idea is in principle easily tested by a peak in the $\ell^+\ell^-$ invariant mass.

7.4.2 Excited leptons[82]

This idea is easily understood, i.e.

$$Z \to \ell^* \ell$$
$$\hookrightarrow \ell\gamma$$

It could imply composite leptons. However in this case the $\ell\gamma$ invariant mass should have a peak. Furthermore experiments at PETRA have ruled out $m_e^* \leq 50$ GeV[84], so only a high mass combination would be allowed. In this case the direction of the γ would not be strongly correlated with the direction of either lepton.

7.4.3 Anomalous $ZZ\gamma$, $Z\gamma\gamma$ couplings[83]

Anomalous $ZZ\gamma$ or $Z\gamma\gamma$ couplings are most easily explained if the Z has a strong coupling to some constituents which would then couple with normal electromagnetic coupling to photons. This would also give a natural explanation to the large value of $\sin^2\theta_W$. The two processes can be distinguished through neutrino decays of the Z, which occur for $ZZ\gamma$ only

$$Z \to \gamma\ 'Z'$$
$$\hookrightarrow e^+e^-,\ \nu\bar{\nu} \text{ etc.}$$

$$Z \to \gamma\ '\gamma'$$
$$\hookrightarrow e^+e^-,\ \mu^+\mu^-$$

Again there is no explanation of why the γ should be close to one of the leptons.

7.4.4 Conclusion on $Z \to \ell\ell\gamma$ decays

A Dalitz plot Monte Carlo study has been carried out by Barger et al.[76] (figure 65) who also plot the actual data for the three events. It is obvious that topologically they are most consistent with bremsstrahlung for the reasons alluded to above. However, the rate remains a factor 10 - 20 too high and one must await further experimental results before any conclusion can be drawn.

7.5 Charm production in jets

UA1[85] have followed the now standard procedure of using the mass difference between D^* and D-mesons in order to isolate events containing charm, i.e.

$$D^{*+} \to D^o\pi^+ \to K^-\pi^+\pi^+$$

and the charge conjugate process. The mass difference

$$\Delta M = M(K^-\pi^+\pi^+) - M(K^-\pi^+)$$

peaks at 147 MeV. The data sample (113 nb^{-1}) comes from two triggers

i) "electron" trigger $E_T > 10$ GeV

ii) global E_T trigger $E_T > 60$ GeV

Figure 66 shows the relevant mass plots. 22 D^* events on a background of 7 are observed out of 3×10^3 jets with the following cuts

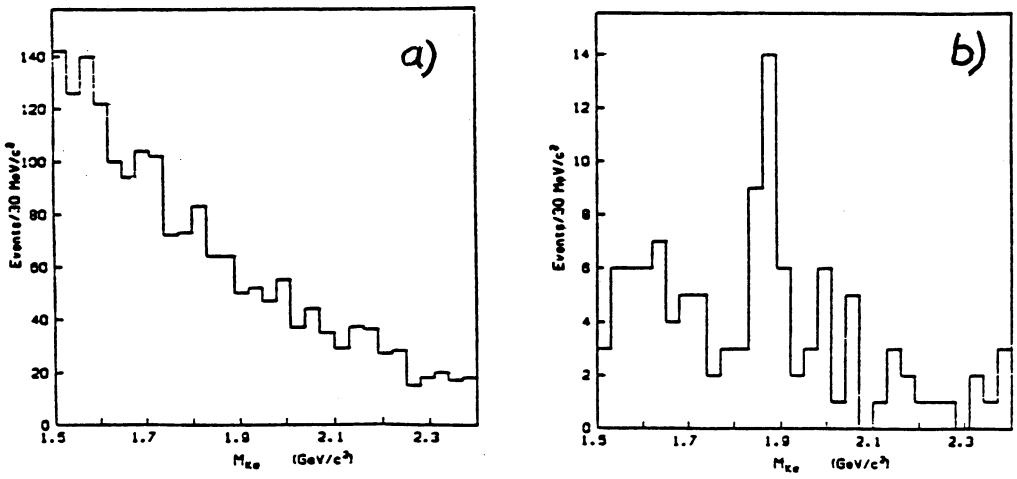

Figure 66 a) M(Kπ) distribution in the region of M(D^o) for all events.

b) M(Kπ) distributions for $146 < \Delta M < 148$ MeV/c^2.

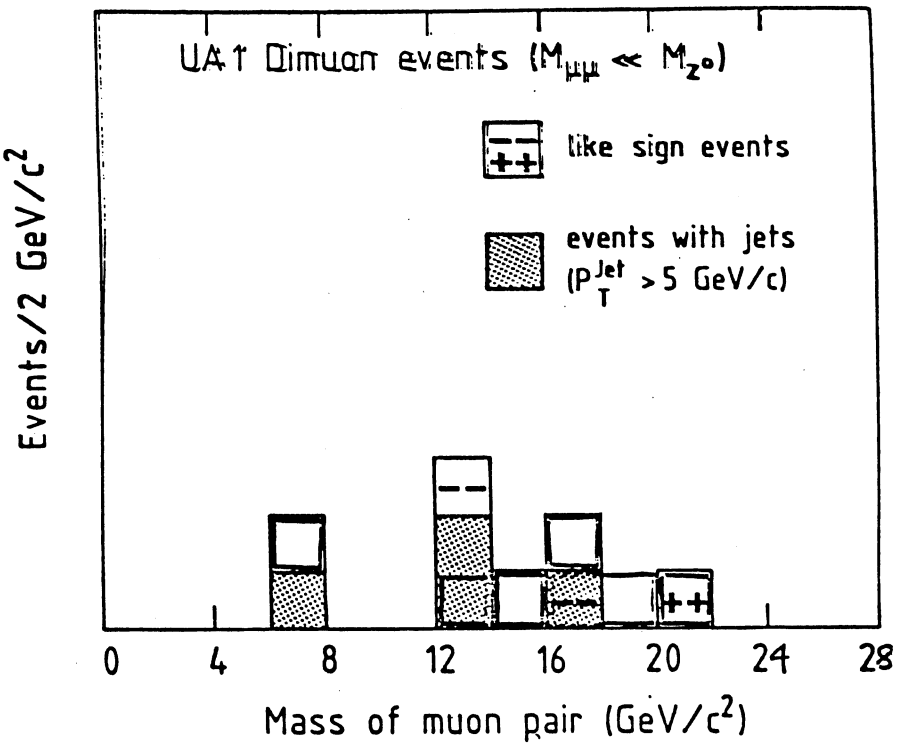

Figure 67 Mass of dimuon pairs with $P_t^{\mu} > 5$ GeV/c excluding Z events.

$$16 \leq E_T^{jet} \leq 20 \text{ GeV}$$
$$|\eta| \leq 1$$
$$\phi \geq 45^o \text{ from the horizontal.}$$

Applying branching ratios etc. gives

$$N(D^{*\pm})/N(\text{jet}) = 1.2 \pm 0.2 \pm 0.7$$

with a rather soft observed fragmentation function[85]. The result is, of course, sensitive to the branching ratio used but nevertheless implies that a very large fraction of what should be mainly gluon jets decay into charmed particles. In one sense this is bad news because it means that the observation of charm is not a distinctive signature, i.e. it does not act as a clean tag for primary heavy quark decays.

7.6 Dimuon events in UA1

From a sample of 108 nb^{-1} UA1[86] have observed 15 dimuon events with $p_t^{\mu} \geq 5$ GeV/c of which 5 are $Z \to \mu^+\mu^-(\gamma)$. Of the ten remaining events 7 have unlike sign and 3 like sign for the two muons. Furthermore they have an unusually high number of accompanying strange particles. Roughly, their characteristics are as follows:

7 $\mu^+\mu^-$	3 with jets and Λ^o or K^o
	1 without jet, with Λ^o and K^o
	3 with jets
3 $\mu^{\pm}\mu^{\pm}$	$\mu^+\mu^-$ with jets
	$\mu^+\mu^+$ without jets, with Λ^o
	$\mu^-\mu^-$ without jets, with $\bar{\Lambda}^o$.

The mass plot for the ten events is given in figure 67.

The main sources of dimuons expected are

i) Drell-Yan (~ 2 events)

ii) Heavy flavour decays (semi leptonic)

a) $p\bar{p} \to Q\bar{Q}X$; $Q \to t,b,c$

b) $p\bar{p} \to ggX$; $g \to b\bar{b}$, $c\bar{c}$

c) W and Z decays e.g. $W \to t\bar{b}$

$W \to t\bar{b}$ decays would give like sign dimuons but can easily be estimated to be much less than one event on the basis of the observed $W \to \mu\nu$ rate (14 events). Similarly, Z decays are negligible. Process a) gives unlike sign dimuons as primary decays, but like signs can be produced as a result of cascade decays. Process b) gives both like sign and unlike sign dimuons and there is already evidence of a high yield of charm decays in jets. It is therefore possible that the observed events have a number of different origins. However, it is interesting to consider $B\text{-}\bar{B}$ mixing in more detail as an origin of the like-sign pairs, particularly the ones with Λ^o and $\bar{\Lambda}^o$.

7.7 $B^o - \bar{B}^o$ mixing

$B^o - \bar{B}^o$ mixing has been studied by Ali and Jarlskog[87]. Neutral B-mesons are of two types

$$B^o_d = b\bar{d} \quad \bar{B}^o_d = \bar{b}d$$

$$B^o_s = b\bar{s} \quad \bar{B}^o_s = \bar{b}s$$

As doubly weak transitions can occur between B^o and $\bar{B}^o$ (as in $K^o, \bar{K}^o$) the mass eigenstates are non-degenerate

$$B^o_{1,2} = \frac{1}{\sqrt{2}} (B^o_d \pm \bar{B}^o_d)$$

$$B^o_{H,L} = \frac{1}{\sqrt{2}} (B^o_s \pm \bar{B}^o_s)$$

The fact that $b \to u$ transitions are strongly suppressed[88] compared to $b \to c$ transitions leads to a larger mass difference ΔM between B^o_H and B^o_L than between B^o_1 and B^o_2. Starting with an initial B^o_s, oscillation and decay occur with relative rates determined by $\Delta M/\Gamma$ where Γ is the average decay rate of B^o_H, B^o_L. In fact $\Delta M/\Gamma$ is estimated to be ~2.5 meaning that several oscillations occur during the lifetime. As the lifetime is very short all B-mesons decay in the apparatus and one integrates from $t = 0$ to $t = \infty$ to find the amount of mixing which is given by

$$r = \text{prob.}\ (B \to \bar{B}) = \text{prob.}\ (\bar{B} \to B) \sim \frac{(\Delta M/\Gamma)^2}{2 + (\Delta M/\Gamma)^2}$$

giving $r \sim 0.75$. Consequently we expect

$$\frac{B^o_s \to \ell^+ \nu X^-}{\overline{B^o_s \to \ell^- \nu X^+}} \sim 0.75$$

and similarly for $\bar{B}^o$. Hence, after allowance is made for other B meson decays Ali and Jarlskog find that

$$\frac{b\bar{b} \to \mu^\pm \mu^\pm X}{\overline{b\bar{b} \to \mu^+ \mu^- X}} \sim 0.2$$

Furthermore, the $\mu^\pm \mu^\pm$ are expected to be accompanied by Λ^o ($\bar{\Lambda}^o$) spectator hyperons, and Monte Carlo calculations indicate little jet activity within the experimental cuts[87].

Thus it is tempting to identify two of the UA1 like sign events as examples of $B\bar{B}$ mixing. However, gluons decaying into $c\bar{c}$ pairs can also give like sign dimuons as well as strange particles[89]. Furthermore the rates are of the right order of magnitude in both cases[87,89].

7.8 Conclusions on dimuon events

In conclusion, there are possibly at least two sources of dimuon events in addition to Drell-Yan, namely $b\bar{b}$ production and gg production with subsequent fragmentation into $c\bar{c}$

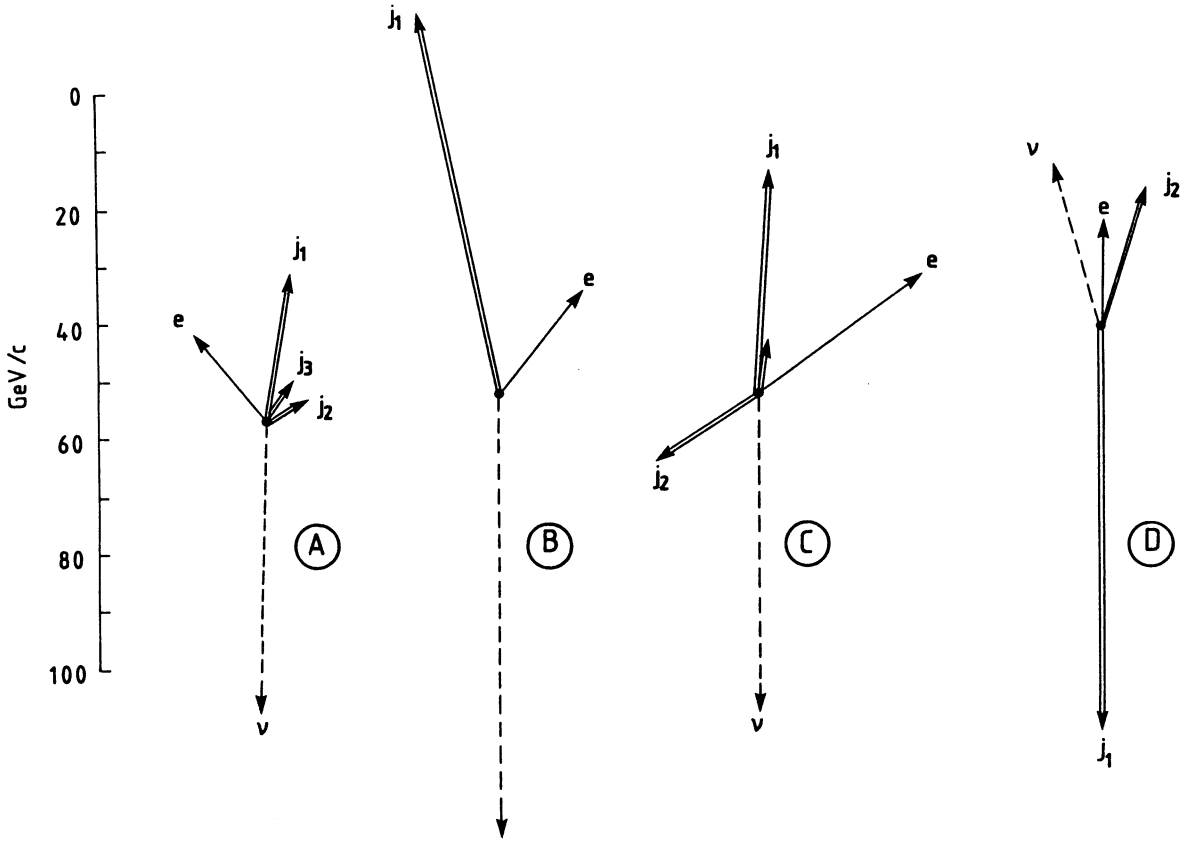

Figure 68 Topology of the four events from UA2.

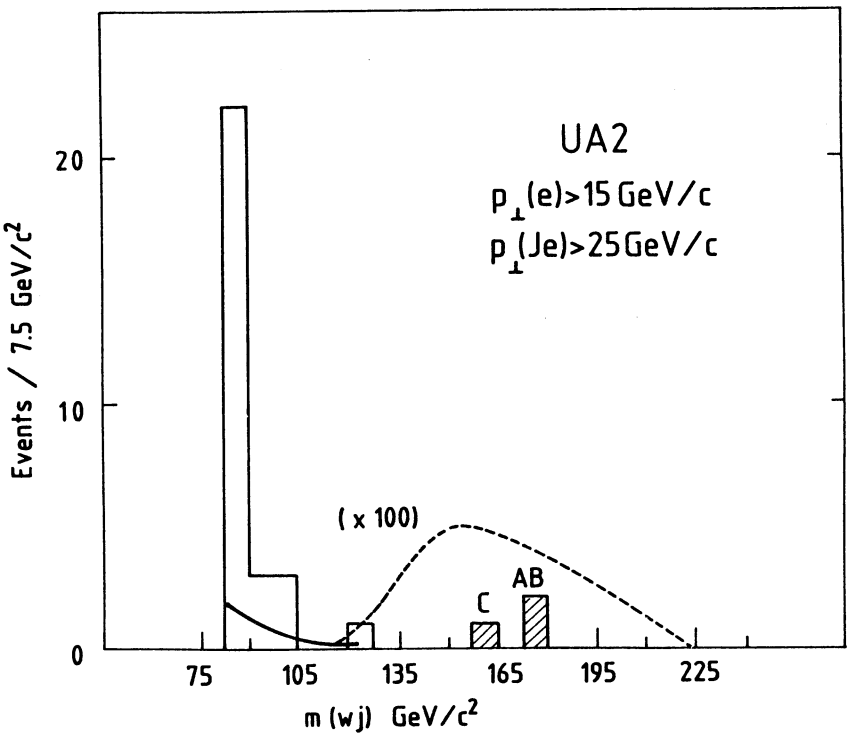

Figure 69 Mass plot for events A, B and C assuming the eν come from a W.

pairs, but the detailed features are not easily explained. Further data are clearly required. However, it is already clear that flavour tagging is not likely to be an easy way to identify primary processes. UA1 have more dimuon data with $p_t^{\mu} > 3$ GeV/c which show a similar fraction of like sign events but will not be discussed here. Such events will be an area of great interest in future runs.

7.9 High mass $e\nu$ Jet events (UA2)

UA2 have observed 4 events with the following characteristics[90]

$$p_t^{e} > 15 \text{ GeV/c}; \quad p_t^{\nu} > 25 \text{ GeV/c}; \quad E_T^{J} > 30 \text{ GeV}$$

They are shown in figure 68, plotted in the transverse plane. An estimate of the background due to misidentified "electrons" is 0.45 event. Event D could be a $q\bar{q}$ pair where one quark decays semi-leptonically. The remaining events have large transverse masses for the $e\nu$ system (assuming that the missing transverse energy is carried by a single neutrino).

Event	$M_T^{e\nu}$	
A	56±4	GeV/c^2
B	81±3	GeV/c^2
C	82±4	GeV/c^2

Furthermore, the total transverse mass of the three events peaks around 170 GeV/c^2 (figure 91), approximately twice the W mass. In fact they are all consistent with W^+W^- associated production where one W decays to jets. However, there is no known mechanism that could produce such a high rate[90]. The rate is also too high to be simply a high p_t W accompanied by a QCD recoil jet. UA1 has not detected any events of the same type. However, the statistics are low and more data are clearly needed. If confirmed, the events would be an indication of physics beyond the standard model.

7.10 Monojets and γs + missing E_T (UA1)[91]

A sample of 113 nb^{-1} was used to search for events with missing transverse energy using the following selection criteria:

$$E_T^{Jet} > 25 \text{ GeV}; \quad E_T^{(\gamma)} > 10 \text{ GeV}$$

$$E_T^{miss} > 15 \text{ GeV} \quad \underline{\text{and}} \quad > 4\sigma$$

Here E_T^{miss} is a "vector" quantity and its empirical standard deviation $\sigma = 0.7\sqrt{\sum E_T}$ where $\sum E_T$ is the scalar sum of the calorimeter transverse energies. The result of the search is:

50 W → $e\nu$
2 γ "ν"
17 J "ν"
5 2J "ν"
3 2J "ν"

The 2 γ-events and 17 single jet events are considered further here. To reduce QCD

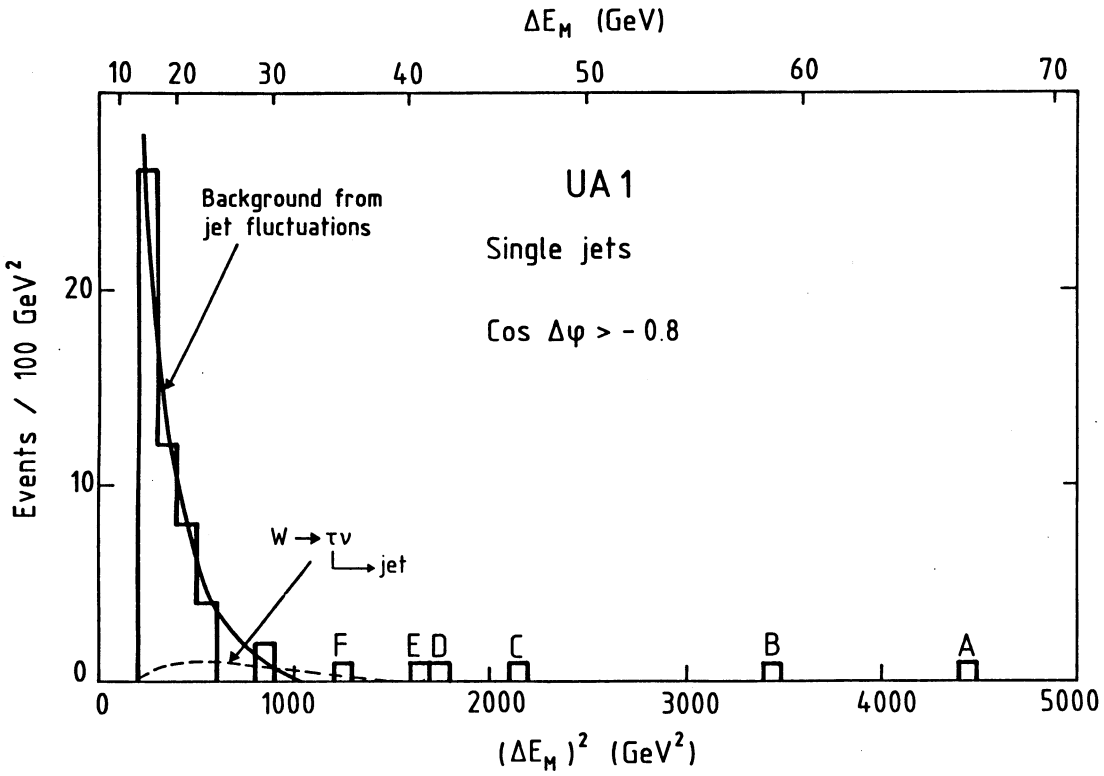

Figure 70 Distribution of missing transverse energy squared for monojet events.

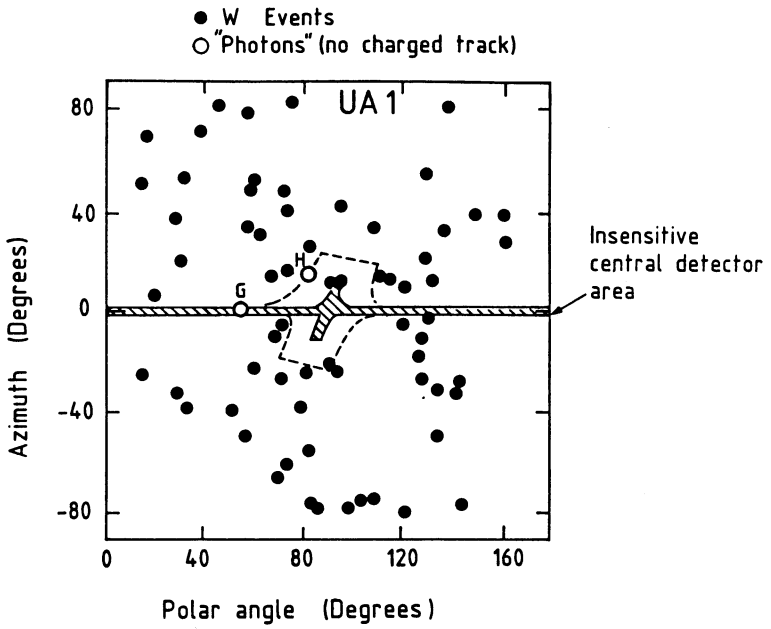

Figure 71 Electron polar vs azimuthal angle plot for W → eν events (solid circles) and the two photon candidates (open circles). The dashed line is the limit for > 20 points on a track.

background, a further cut is applied to the 17 single jet events which removes events with $\cos \Delta\phi < -0.8$, where $\Delta\phi$ is the azimuthal angle between the jet and the E_T vector of the rest of the event. Of those that remain, six have $E_T^{miss} > 30$ GeV and are labelled A, B, C, D, E, F in figures 70 and 72. Figure 70 shows the missing E_T for the six events in a plot where the cut has been reduced to 2σ. The solid curve shows the expected background from jet fluctuations and the dashed curve the calculated background from $W \to \tau\nu$ decays where the τ produces a "jet". Event F is consistent with $W \to \tau\nu$ and is not considered further. The remaining events A-E all have large missing E_T and all have 'jet-ν' masses greater than m_W. Event A is particularly spectacular in having a high energy muon in the jet. Their features are summarised in the following table.

Event	Jet E_T (GeV)	Missing p_t (GeV)	m_T(jet,p_T^{miss}) (GeV)	Charged Multiplicity	Invariant mass of charged particles (GeV)
A	25 (71 inc μ)	24 ± 4.8 (66±8 inc μ)	130 ± 16 inc μ	1	0.1
B	48	59 ± 7	106 ± 12	3	0.79 ± 0.12
C	52	46 ± 8	97 ± 17	1	Other unreconstructed tracks?
D	43	42 ± 6	85 ± 12	4	3.14 ± 0.38
E	46	41 ± 7	87 ± 14	2	Other unrecontructed tracks
F	39	34 ± 7	73 ± 14	2	0.52 ± 0.06
H	54(γ)	40 ± 4	93 ± 5	0	0

The azimuthal and polar angles of the "photons" in the 2γ-events are shown in figure 71. The 'γ' from event G falls in a region of the central detector which is insensitive to charged tracks and therefore could be an electron from W decay. The dashed curves outline regions with at least twenty points per track so event H is definitely neutral and could be due to one or more photons with missing energy. Thus we are left with $5J'\nu'$ and $1\ \gamma'\nu'$ events all with $m > m_W$. The missing E_T is plotted against the E_T of the jet or γ in figure 72. A more detailed discussion has been given by J. Rohlf[92]. A typical event is shown in Figure 73.

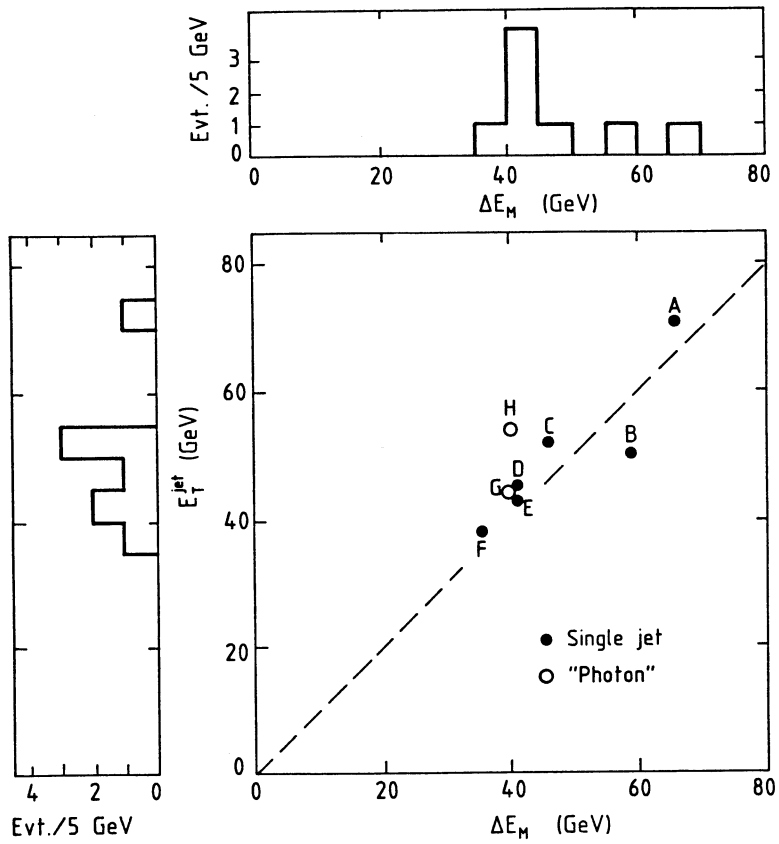

Figure 72 Scatter plot of missing E_T vs jet or photon(s) E_T from events A - H.

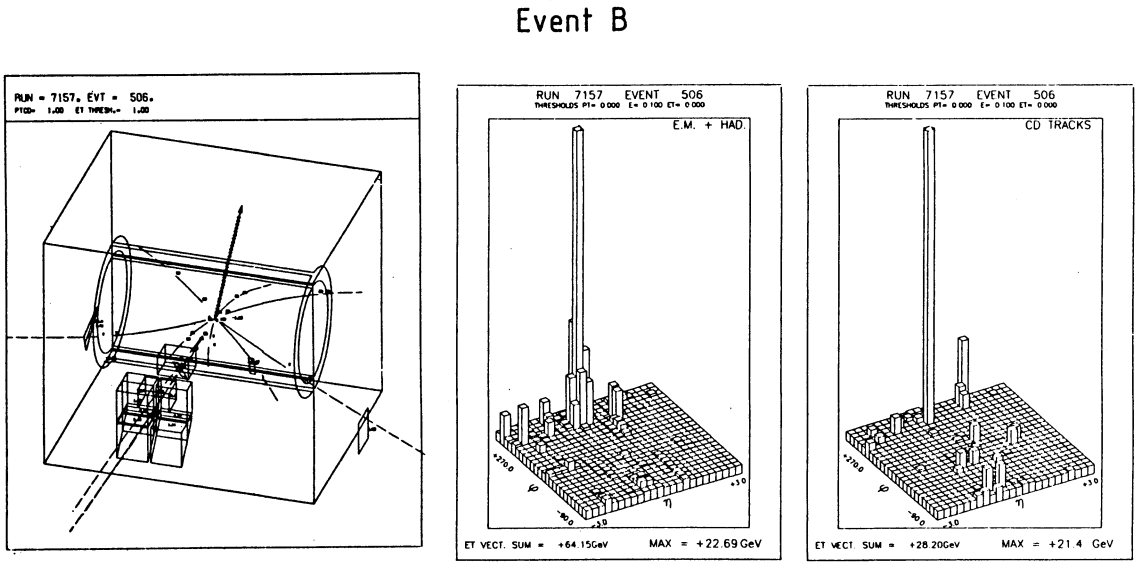

Figure 73 One of the monojet events. The arrow shows the direction of the missing transverse energy.

7.10.1 Possible interpretations of the events

Two basic interpretations have been considered for the J'ν' events:

a) Excited quarks[93]

b) Supersymmetry[94]

The first hypothesis has been considered by Kuhn and Zerwas[93] and implies composite quarks. The process is

$$p\bar{p} \to Q^*\bar{q} + X$$
$$\hookrightarrow qZ;\ Z \to \nu\bar{\nu}$$

The fact that $Z \to \nu\bar{\nu}$ is six times more probable than $Z \to e^+e^-$ could explain why no e^+e^- event has been seen. Similarly the process could explain the UA2 events as $Q^* \to qW$; $W \to e\nu$. However, one would also expect $Q^* \to q\gamma$ events. More statistics would obviously test this hypothesis. Such an explanation would require $m_{Q^*} \geq 2m_W$, similar to the masses of the UA2 events. Under this hypothesis the events are indeed consistent with a common mass of ~ 170 GeV/c^2 [92].

The explanation based on supersymmetry has been considered by a number of authors[94]. The events could be either gluino or squark decays. The basic process for gluino production is

$$p\bar{p} \to \tilde{g}\tilde{g}\ X$$
$$\hookrightarrow q\bar{q}\tilde{\gamma}$$

The gluino is assumed to decay to $q\bar{q}\tilde{\gamma}$ where the photino escapes without interaction, giving rise to the missing energy. The events have several jets but yield predominantly single jet events after the application of experimental cuts. If the 5 events are taken as an upper limit on gluino production, then $m_{\tilde{g}} \geq 40$ GeV/c^2 to give the observed cross section (0.06 nb).

The production of squarks is by

$$gg \to \tilde{q}\tilde{q}$$

$$q\bar{q} \to \tilde{q}\bar{\tilde{q}}$$

$$qg \to \tilde{q}\tilde{g}$$

In order to explain the events as squark ($\tilde{q}$) decays it is assumed that $\tilde{q} \to q\tilde{\gamma}$. This will only be the main decay mode if $m_{\tilde{g}} > m_{\tilde{q}}$. Again the five events ($\sigma \sim 0.06$ nb) are consistent with $m_{\tilde{q}} \gtrsim 40$ GeV/c^2. Furthermore, the narrowness of the jets favours this interpretation.

The type of explanation offered for the γ event is an unusual fragmentation of a jet. However, $Z \to \nu\nu\gamma$ could not be entirely ruled out. More exotic explanations for the events have also been considered[95].

7.10.2 Conclusion on UA1 monojets

The event are not explicable within the standard model. Excited quarks should have other decay modes which would be observed with more data. Supersymmetric particles would

have to have masses in the 40 GeV/c^2 region to be consistent with the observed cross sections. Squarks are favoured over gluinos by the narrowness of the jets (and absence of other jets) but this hypothesis only works if $m_{\tilde{g}} > m_{\tilde{q}}$ so that the squark decays into a quark and photino. However, the events may have a completely different origin and obviously provide a topic of great excitement for forthcoming collider runs.

7.11 Evidence for the Top Quark(UA1)

Data from the 1983 run (120 nb^{-1}) have been used to study events with an electron + jets or a muon + jets in which the lepton is isolated from the jets[95]. Such events should include candidates for $t \to \ell\nu b$ as the large t mass (> 22.5 GeV/c^2 from PETRA) would cause the three decay products to be produced with large relative transverse momenta. More specifically the decay $W \to t\bar{b}$ would give 2 jets, a lepton and missing energy with a total mass consistent with that of the W. The experimental task is to demonstrate that any such 'top' candidates are distinguishable from background due to QCD processes, e.g. $pp \to b\bar{b}X$ where the b or $\bar{b}$ decays semi-leptonically. Only the general principles of the background study will be described here. For full details the reader is referred to the published work[96]. Unlike in the W search, the full power of the apparatus proved to be needed to isolate the candidates.

7.11.1 Electron selection

Electron candidates were selected by the following cuts

i) $E_T^{em} > 12$ GeV with $E_T^h < 0.2$ GeV,

ii) $p_t > 7$ GeV/c for matching CD track,

iii) isolated i.e. the 'electron' having $> 90\%$ of the E_T in $\Delta r < 0.7$ around the track ($\Delta r = \sqrt{\Delta\phi^2 + \Delta\eta^2}$).

The search yielded 49 $W \to e\nu$ events which were used as a calibration sample for electrons and 152 'e' + jets. Of those 152 events 43 with $\gamma \to e^+e^-$ conversions were removed by detecting the second electron. Next a momentum-energy comparison $|1/p - 1/E| < 3\sigma$ and a χ^2 test on the shower profile[97] through the four layers of the electromagnetic calorimeters were applied to remove $\pi^\pm/\pi^o$ overlaps. Together with a further isolation cut, requiring $\sum p_t$(charged tracks) < 1.0 GeV/c and $\sum E_T < 1.0$ GeV in $\Delta r < 0.4$ around the electron, this reduced the sample to 19 events on which the final analysis was performed. Using as jet definition E_T(1st jet) > 8 GeV, E_T(other jets) > 7 GeV the events fall into the following classes.

e + 1 jet : 14 events
e + 2 jets : 3 events
e + 3 jets : 2 events

As the principal source of background is expected to be residual $\pi^\pm/\pi^o$ overlaps a study of the background shape was made using 'π^o' + jets events with similar selection criteria for

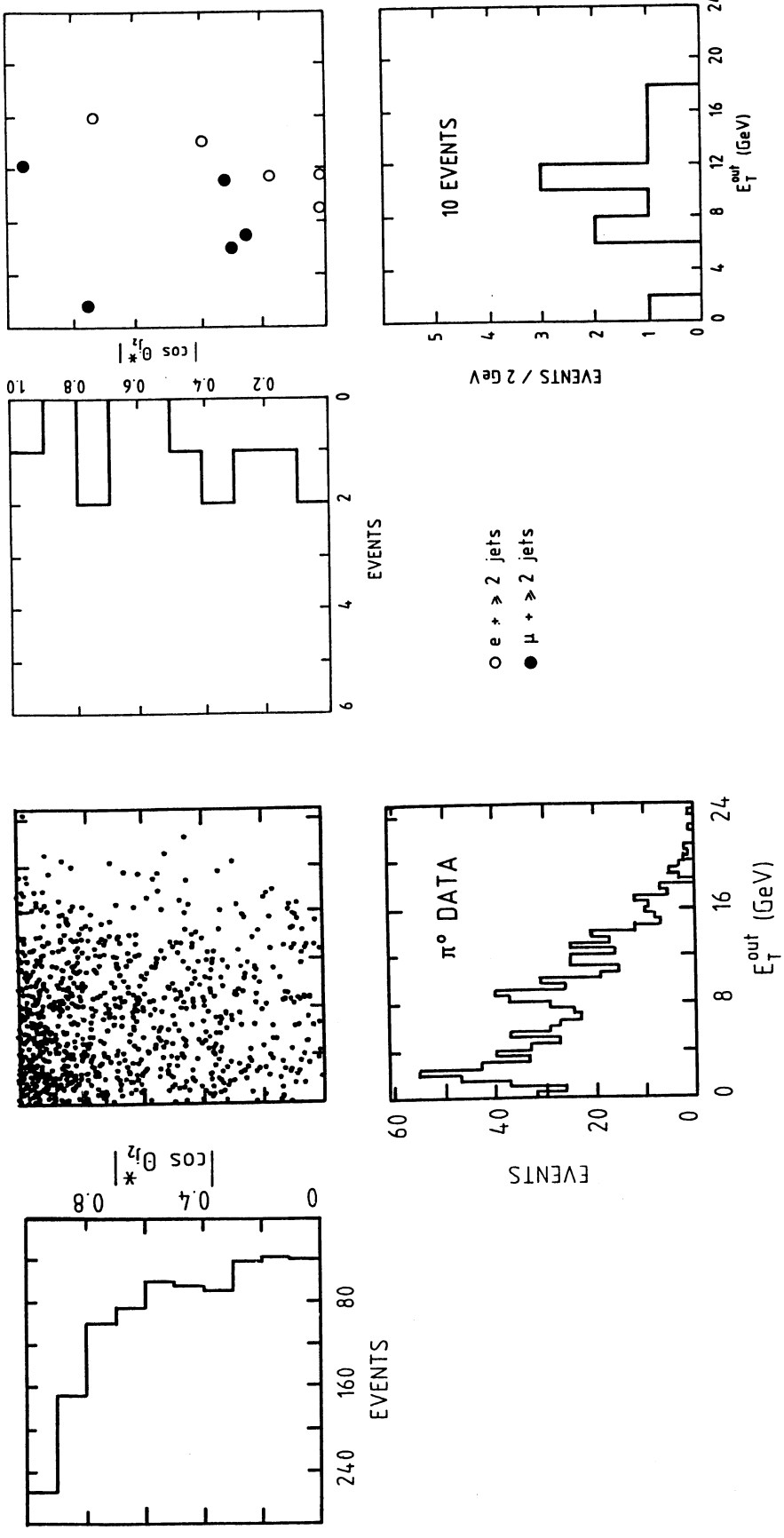

Figure 74 a) Measured shape of the QCD background from π^0 + ≥ 2 jets events.

b) Equivalent plot for the electron or muon + ≥ 2 jets events.

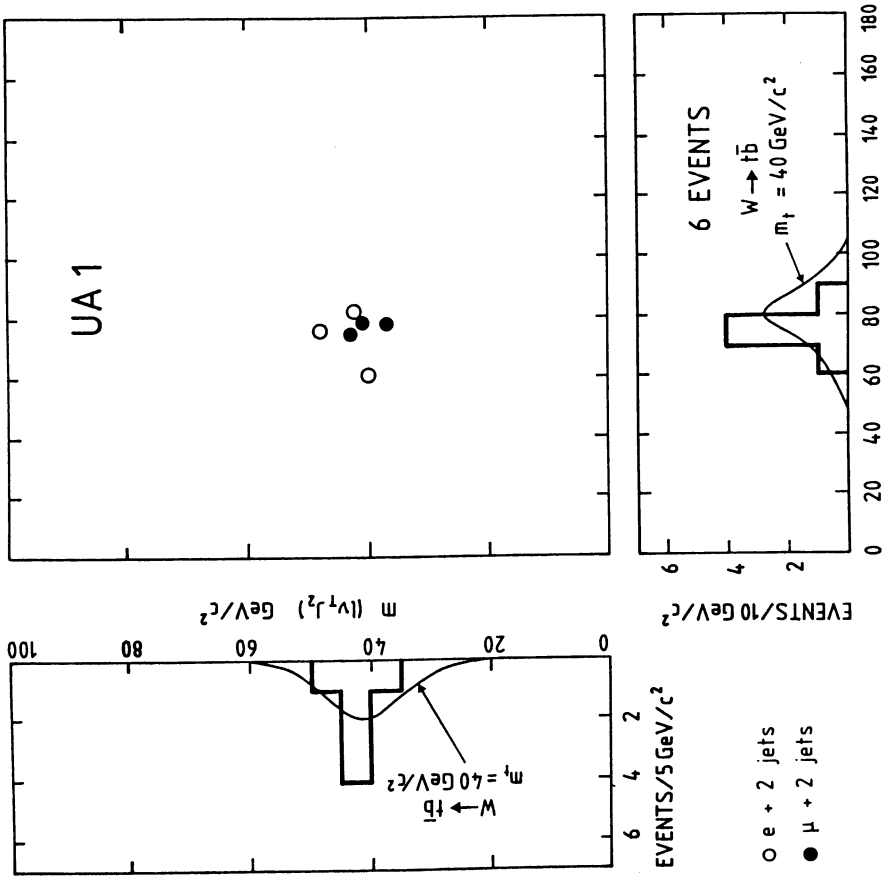

Figure 76 Four-body versus three-body mass distribution for the six W → tb candidates.

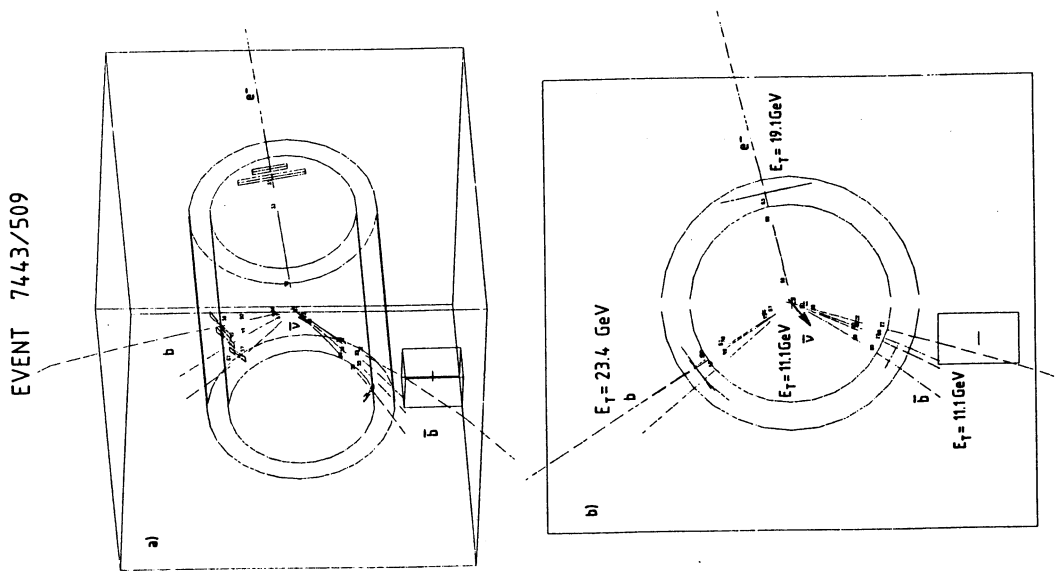

Figure 75 A typical top quark candidate.

the 'π^o'. Secondly, from the measured flux of $\pi^{\pm}$ (+ $m\pi^o$) + jets events, the probability of an overlap simulating an electron was estimated. It turns out that the 'background' events populate a two dimensional plot of E_t^{out} vs $\cos\theta^*_{J_2}$(where E_t^{out} is the transverse momentum of the electron relative to a plane containing the beam and jet$_1$, and $\cos\theta^*_{J_2}$ is the centre of mass angle of the second jet with respect to the beam direction) in quite a different way from the candidate events (Figure 74). The background peaks at cos θ^* close to ± 1, as expected for gluon bremsstrahlung, and low values of E_t^{out}. The resulting background estimate is ≤ 0.1 event in the region occupied by the electron + 2 jet events ($E_T^{out} \geq 8$ GeV, $|\cos\theta^*_{J_2}| \geq 0.73$).

7.11.2 Muon selection

The selection of muon + jets events is somewhat simpler. Using the same jet definition, events with a muon + 1 jet having $p_t^{\mu} \geq 12$ GeV/c were selected with an isolation criterion that the muon should carry $\geq 90\%$ of the p_t (charged tracks) and $\geq 80\%$ of E_T in a radius $\Delta r \leq 0.4$. The 14 $W \to \mu\nu$ events were used as a calibration sample. Twelve μ + jet events are found

μ + 1 jet : 7 events

μ + 2 jets : 4 events

μ + 3 jets : 1 events

$\pi \to \mu$ and $K \to \mu$ decay background dominates but this is calculable from the observed hadron spectrum, assuming 25% Ks and 50% πs. The resulting background estimate is 0.4 event for the μ + 2 jet events. One of them has cos $\theta^*_{J_2} = 0.93$ and is most likely background . It has therefore been removed. The background for the remaining three is estimated to be ≤ 0.1 event.

7.11.3 Consistency with the $W \to t\bar{b}$ hypothesis

The topological features of one of the 3 electron and 3 muon events with 2 jets are shown in figure 75. Figure 76 is a two-dimensional plot of the mass of $\ell\nu J_1 J_2$ versus $\ell\nu J_2$. Here the transverse momentum of the neutrino is used and the lower energy jet (J_2) is assumed to come from the t-decay. The alternative assumption produces a much broader mass peak for $\ell\nu J_1$. Corrections have been applied to the jet energies using a Monte Carlo method as described in section 5.6. The events peak at a mass consistent with the W (see curve) and give $m_t = 40 \pm 10$ GeV/c^2 assuming they come from $W \to t\bar{b}$. Furthermore the rates agree with expectation after allowance for the leptonic branching ratio of the t (~12%) and the experimental cuts [96].

7.11.4 Conclusion on top candidates

While it is not possible with the present statistics to be totally certain that the top quark has been isolated, the following remarks can be made.

i) A signal has been observed for an isolated lepton + $\geq$ 2 jets.

ii) The 2-jet events cluster around the W-mass.

iii) They are consistent with $W \to t\bar{b}$ with $t \to \ell\nu b$.

iv) If so then 30 GeV/c^2 $\leq m_t \leq$ 50 GeV/c^2.

In addition the events with a lepton + 3 jets could be examples of $t\bar{t}$ QCD production.

7.12 Prospects for observing Higgs scalars at the collider

Higgs mesons couple to heavy objects preferentially. However, the prospect for observing Higgs particles is not particularly promising unless the Higgs mass is rather low[96]. For m_H = 10 GeV, $\frac{\sigma(W + \text{Higgs})}{\sigma(W)}$ is $\sim 10^{-2}$ and the experimental signature rather difficult to interpret. Events involving Z's would be cleaner

$$\frac{\sigma(Z \to \ell^+\ell^- H)}{\sigma(Z \to \ell^+\ell^-)} \sim 10^{-2} \text{ for } m_H = 10 \text{ GeV}$$

$$\sim 10^{-4} \text{ for } m_H = 40 \text{ GeV}$$

The diagram is

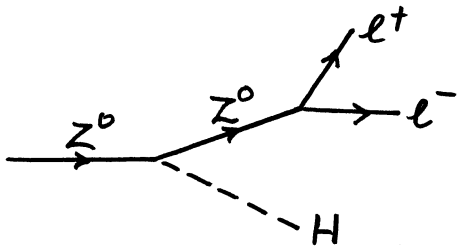

The initial Z may be virtual and the intermediate Z real, or vice versa. Given that only 10^3 $Z \to \ell^+\ell^-$ decays are expected at the upgraded collider the sensitivity is however, very low. If $m_H > 2m_b$ but $< 2m_t$ the Higgs will decay to $b\bar{b}$. A microvertex detector in UA1 could detect decay vertices of b or c in a reasonable proportion of the events: e.g. 2 vertices would be detected in 37% of events for m_H = 30 GeV/c^2 according to a Monte Carlo calculation[98]. However, we have already noted that gluon jets fragment into charmed particles at high rates which could give a high background.

8. CONCLUSIONS AND FUTURE PROSPECTS

The CERN proton-antiproton collider has proved to be an extremely rich source of physics. Not only has it fulfilled all the expectations based on the standard model of the electroweak interaction in the discovery of the W and Z particles with the predicted masses and properties and the probable discovery of the top quark, but has turned out to be an excellent testing ground for QCD as clear jet events are easily observed.

In fact, the ease with which the various processes can be isolated has exceeded even the most optimistic forecasts. It is a fitting tribute that Carlo Rubbia and Simon van der Meer have been awarded the 1984 Nobel Prize for Physics, an honour that is fully deserved for the realisation of this adventurous project. However, perhaps it will also prove to be the basis for the next major step in the study of elementary particles as there are already hints of physics beyond the standard model. The UA1 monojets and UA2 high mass electron-jet events with missing energy have no conventional explanation and may be the first signs of supersymmetry or compositeness. In addition there is a variety of other pheneomena - dimuons, radiative Z-decays, high jet multiplicity with Zs, etc. - which may also have exotic explanations.

What can we look forward to in the next few years? The collider is already scheduled to run in 1984, 1985 and 1986 with a luminosity at least comparable to the best obtained in 1983 and an increased energy of 630 GeV. In fact, 2.5 x 10^{29} $cm^{-2}s^{-1}$ has already been achieved giving 10 nb^{-1} per day. The scheduled running should therefore produce at least a five-fold increase in statistics, sufficient to confirm many of the phenomena for which there are hints. UA1 has improved muon detection and a micro-vertex detector which will help in unravelling the new physics. A special ramped collider mode, cycling up to 900 GeV, has been tested and will run in 1985 with modest luminosity (10^{26} $cm^{-2}s^{-1}$) enabling UA1 and UA5 to search for phenomena that might have a higher threshold energy such as the Centauro events.

In the longer term, the antiproton yield is to be increased by a factor of ten in 1987 by the addition of an antiproton collector ring, ACOL[99]. Both UA1 and UA2 are to have major upgrades to their calorimeters. UA2[100] will close the end regions, thus improving the missing energy determination and UA1[101] will replace the central electromagnetic calorimeters by a much more finely divided set of Uranium calorimeters. Uranium provides compensation for the different response to hadrons and electromagnetic particles through the fission process and, since it will absorb most of the hadron energy, will give a factor of two improvement in jet and missing energy resolution. The improved granularity will help the study of electrons in jets, extending the physics capability. Thus we can look forward with great excitement to 50 times the present data by 1990, approximately the time when LEP will be fully operational.

9. ACKNOWLEDGEMENTS

I should like to thank Cecilia Jarlskog and the organising committee for the opportunity to lecture at the CERN School which I have found most stimulating. I am conscious of my inability to do justice to the vast amount of theoretical work that has accompanied the collider results and am sure to have left out many important contributions. For this I apologise. In preparing my lectures I have profited particularly from the excellent review by E. Rademacher[58], from the lectures of H. Wahl[102], the summary of the recent Berne topical meeting on collider physics by J. Ellis[103] and other talks at that meeting. I have had valuable discussions with many people, particularly D. Haidt, S. Rudaz and all the members of the UA experiments who attended the school. It is a pleasure to thank Carlo Rubbia and my colleagues on the UA1 experiment for their help in providing me with much of the material including some while I was at the school. Similar thanks go to the members of the other UA experiments who sent me results. Finally, a special thankyou is due to Sharon Ellis for her patient typing of this manuscript.

References

1. The staff of the CERN proton-antiproton project, Phys. Lett., 197B (1981) 306.

2. S. Weinberg, Phys. Rev. Lett. 19 (1967) 1264; S.L. Glashow, Nucl. Phys. 22 (1961) 579; A. Salam, Proc. 8th Nobel Symposium, Aspenasgarden, Almqvist and Wiskell; Stockholm (1968) 367.

3. UA6 proposal; CERN/SPSC/80-63/P148.

4. UA1 proposal: CERN/SPSC/78-6/P92. M. Barranco Luque et al., Nucl. Inst. Meth. 176 (1980) 175. M. Calvetti et al., Nucl. Inst. Meth. 176 (1980) 255. M. Calvetti et al., IEEE Trans. Nucl. Sci. NS-30 (1983) 71. M. Corden et al., Phys. Scr. 25 (1982) 5 and 11. K. Eggert et al., Nucl. Inst. Meth. 176 (1980) 217.

5. UA2 proposal: CERN/SPSC/78-8/P93. B. Mansoulie, The UA2 apparatus at the CERN $\bar{p}p$ collider, Proc. 3rd Moriond Workshop on pp physics (1983) 609 (editions Frontieres).

6. UA3 proposal: CERN/SPSC/78-15/P96. B. Aubert et al., Phys. Lett. 120B (1983) 465.

7. UA4 proposal: CERN/SPSC/78-105/P114.

8. UA5 proposal: CERN/SPSC/78-70/P108.
UA5 collaboration, Phys. Scripta 23 (1981) 642.

9. G. Arnison et al., Phys. Lett. 121B (1982) 77.
Phys. Lett. 128B (1983) 336.

10. R. Battiston et al., Phys. Lett. 115B (1982) 333.
Phys. Lett. 117B (1982) 126.

11. G. Matthiae, XVth Symposium on Multiparticle Dynamics, June 1984, Lund, Sweden; CERN/EP 84-119.
M. Bozzo et al., Phys. Lett. 147B (1984) 385 and 392.

12. U. Amaldi et al., Phys. Lett., 66B (1977) 390.

13. M. Block and R. Cahn, Phys. Lett. 120B (1983) 229.

14. J. Baumel et al., Nucl. Phys. B198 (1982) 13.

15. L. Baksay et al., Nucl. Phys. B141 (1978) 1.

16. J. Burq et al., Phys. Lett., 109B (1982) 124.

17. A. Martin, Zeit. f. Physik C15 (1982) 185. Proc. 4th Topical Workshop on $\bar{p}p$ collider physics, Bern, 5-8 March 1984; CERN 84-09.

18. M. Froissart, Phys. Rev. 123 (1961) 1053.

19. G. Matthiae, Proc. Int. High Energy Physics Conf., Brighton, 1983, p314.
P. Kroll ibid. p295. (See also refs. 11, 17).

20. R. Battiston et al., Phys. Lett. 136B (1984) 217.

21. M. Albrow et al., Nucl. Phys. B108 (1976) 1.

22. A. B. Kaidalov et al., Phys. Lett. 45B (1973) 493.

23. G. Arnison et al., Phys. Lett. 123B (1983) 108.

24. K. Alpgard et al., Phys. Lett., 107B (1981).

25. C. J. Alner et al., Phys. Lett. 138B (1984) 304.

26. R. P. Feynman, Phys. Rev. Letters 23 (1969) 1415.

27. G. Arnison et al., Phys. Lett. 118B (1982) 167.

28. Z. Koba, H. B. Nielsen and P. Olesen, Nucl. Phys. B40 (1972) 117.

29. K. Alpgard et al., Phys. Lett. 123B (1983) 361.

30. A. B. Kaidalov, Phys. Lett, 116B (1982) 459.
A. B. Kaidalov, and K. A. Ter-Martirosyan, Phys. Lett. 117B (1982) 249.
P. Carruthers and C. C. Shih, Los Alamos preprint. LA-UR-83-1231.
S. Barshay, Phys. Lett. 116B (1982) 193.
L. S. Liu and T. Meng, Phys. Rev. D27 (1983) 2640.
G. Pancheri and Y. Srivastava, Frascati report LNF 83-25.
G. Pancheri, 1984 Lund Symposium on Multiparticle Dynamics, CERN/EP 84-96.

31. G. M. G. Lattes et al., Physics Reports, Vol. 65, No. 3 (1980).

32. L. Van Hove, Phys. Lett. 118B (1982) 138 and CERN TH3924.

33. P. Carlson, 4th Topical Workshop on $p\bar{p}$ collider physics, Bern, 5-8 March, 1984; CERN 84-09.

34. A. Capella and A. Krzywicki, Orsay preprint LPTHE 83/12.

35. M. Banner et al., Phys. Lett. 115B (1982) 59.

36. K. Alpgard et al., Phys. Lett. 115B (1982) 65.
G. J. Alner et al., Phys. Lett. 122B (1983) 189.

37. G. Arnison et al., Phys. Lett. 122B (L983) 189.

38. K. Alpgard et al., Phys. Lett. 115B (1982) 71.

39. G. Arnison et al., Phys. Lett. 123B (1983) 115.

40. G. Arnison et al., Phys. Lett. 132B (1983) 214.

41. G. Arnison et al., Phys. Lett. 132B (1983) 223.

42. G. Arnison et al., Phys. Lett. 136B (1984) 294.

43. M. Banner et al., Phys. Lett. 118B (1982) 203.

44. P. Bagnaia et al., Phys. Lett. 138B (1984) 430.

45. P. Bagnaia et al., Phys. Lett. 144B (1984) 283.

46. P. Bagnaia et al., Phys. Lett. 144B (1984) 291.
Z. Phys., C20 (1983) 117.

47. F. E. Paige and S. D. Protopopescu, ISAJET, BNL 31987.

48. see ref. 40.

49. R. Brandelik et al., Phys. Lett. 114B (1982) 65.

50. B. Webber, CERN TH-3569 (1983).

51. Z. Kunszt and E. Pietarinen, CERN TH-3584 (1983).

52. B. Combridge et al., Phys. Lett. 70B (1977) 234.

53. B. Combridge and C. Maxwell preprint RL-83-095.
G. Cohen-Tannoudji et al., preprint sPh.T/70 (1982).
F. Halzen and P. Hoyer, Phys. Lett. 130B (1983) 326.

54. H. Abramowicz et al., Z. Phys. C12 (1982) 289.

55. see reference 51.

56. C. Jarlskog, Lectures at ths school.

57. D. Haidt, lectures at this school.

58. E. Rademacher, CERN EP/84-41 to be published in Progress in Particle and Nuclear Physics.

59. E. Williams and P. Olsen, Phys. Rev. Lett. 42 (1979) 1575.

60. J. E. Kim et al., Res. Mod. Phys. 53 (1981) 211.

61. For a review see W. J. Marciano, Proc. 1983 Int. Symp. on Lepton and Photon interactions at High Energies, Cornell, p80.
Recent calculations have been done by:-
A. Sirlin and W. J. Marciano, Nucl. Phys. B189 (1981) 442.
C. Llewwllyn Smith and J. Wheater, Phys. Lett. 105B (1981) 486.

62. W. J. Marciano and Z. Parsa, Proc. 1982 DPF. Summer Study on Elementary Particle Physics and Future Facilities, Snowmass, 1982 (AIP, New York, 1983) p155.

63. I. R. Kenyon, Rep. Prog. Phys. 45 (1982) 1261.

64. F. Paige, BNL-27066 (1979).

65. S. Pakvasa et al., Phys. Rev. D20 (1979) 2862.
P. Aurenche and J. Lindfors, Nucl. Phys. B185 (1981) 274 and 301.

66. J. Rohlf, UA1 technical note TN83-07.

67. G. Arnison et al., Phys. Lett. 122B (1983) 103.
Phys. Lett. 129B (1983) 273.

68. G. Arnison et al., Phys. Lett. 134B (1984) 469.

69. M. Banner et al., Phys. Lett. 122B (1983) 476.
P. Bagnaia et al., CERN-EP/84-39.
Submitted to Z. Phys. C.

70. G. Arnison et al., Phys. Lett. 126B (1983) 398.

71. P. Bagnaia et al., Phys. Lett. 129B (1983) 130. (see also ref. 69).

72. CHARM II experiment at the CERN SPS, WA79.

73. G. Altarelli et al., CERN TH-3851 (1984).
F. Halzen and D. M. Scott, Phys. Lett. 87B (1978) 318.
P. Chiappetta and M. Greco, Frascati report LNF-83/44 Rev. (1983).
A. Nakamura, G. Pancheri and Y. Srivastava, Frascati report LNF-83/43(R) (1983).
see also ref. 65.

74. S. Geer, UA1 $p\bar{p}$ note 78 (1984).

75. G. Arnison et al., Phys. Lett. 147B (1984) 241.

76. V. Barger, H. Baer and K. Hagiwara, Wisconsin preprint MAD/PH/176.

77. G. Sterman and S. Weinberg, Phys. Rev. Lett. 39 (1977) 1436.

78. F. A. Berends et al., CERN-EP/84-117 submitted to Z. Phys. C.

79. G. Arnison et al., Phys. Lett. 135B (1984) 250.

80. P. Bagnaia et al., CERN-EP/84-39, Submitted to Z. Phys. C.

81 U. Baur, H. Fritsch and H. Faissner, Phys. Lett. 135B (1984) 313.
M. Leurer, H. Harari and R. Barbieri, Phys. Lett. 141B (1984) 455.
B. Holdom, Phys. Lett. 143B (1984) 241.
M. Matsuda and T. Matsuoka, Phys. Lett. 144B (1984) 443.
M. Leurer, Phys. Lett. 144B (1984) 273.
P.D.B. Collins and N.A. Speirs, Phys. Lett. 144B (1984) 275.
V. Visnjic, Phys. Lett. 143B (1984) 158.
D. Dusedau et al., Phys. Lett. 145B (1984) 292,
and others.

82. N. Cabibbo, L. Maiani and Y. Srivastava, Phys. Lett. 139B (1984) 459.
K. Enqvist and J. Maalampi, Phys. Lett. 135B (1984) 329.

83. G. Gounaris, R. Kogerler and D. Schildnicht, Phys. lett. 137B (1984) 261.
A. Barroso, F. Boudjema, J. Cole and N. Dombey, Sussex University preprint, 1984.
Y. Tomozawa, Phys. Lett. 139B (1984) 455.
F. M. Renard, Phys. Lett. 139B (1984) 449,
Nucl. Phys. B186 (1982) 93.

84. S.L. Wu, DESY 84-028, To be published in Physics Reports.

85. G. Arnison et al., Phys. Lett. 147B (1984) 222.

86. G. Arnison, to be published in Phys. Lett.

87. A. Ali and C. Jarlskog, Phys. Lett. 144B (1982) 266.
Other relevant papers are by:
E.W.N. Glover, F. Halzen and A.D. Martin, Durham preprint, DTP/84/2.
F. Halzen et al., Wisconsin preprint, MAD/PH/171
Durham preprint, DTP/84/8.
V. Barger and R.J.N. Phillips, Wisconsin preprint, MAD/PH/155.

88. J. Lee Franzini, Europhysics Conf. on Flavour Mixing in Weak Interactions, Erice, March 1984.

89. F. Halzen and F. Herzog, Wisconsin preprint MAD/PH/985.
K. Hagiwara and S. Jacobs, Wisconsin preprint MAD/PH/192.

90. P. Bagnaia et al., Phys. Lett. 139B (1984) 105.

91. G. Arnison et al., Phys. Lett. 139B (1984) 115.

92. J. Rohlf, Proc. 1984 Int. Conf. on High Energy Physics, Leipzig, CERN-EP/84-126.

93. J. H. Kuhn and P.H. Zerwas, Aachen preprint PITHA 84/14.

94. J. Ellis and H. Kowalski, Phys. Lett 142B (1984) 441.
H.E. Haber and G.L. Kane, Phys. Lett. 142B (1984) 212.
J.H. Kuhn and S. Ono, Phys. Lett. 142B (1984) 436.
M.J. Herrero et al., Phys. Lett. 145B (1984) 430. Phys. Lett. 132B (1983) 199.
V. Barger, K. Hagiwara and W.Y. Keung, Phys. Lett. 145B (1984) 147.
E. Reya and D.P. Roy, Phys. Rev. Lett. 53 (1984) 1309.
J. Ellis and M. Sher, CERN-TH 3968/84.

95. S.L. Glashow, Phys. Lett. 143B (1984) 130.
H. Georgi and S.L. Glashow, Phys. Lett. 143B (1984) 155.

96. G. Arnison et al., CERN-EP/84-134, to be published in Physics Letters.

97. E. Eisenhandler et al., UA1 technical note, TN 84-64.

98. D. Dibitonto, R. Kinnunen and M. Mohammadi, UA1/TN 83-70.

99. Design study of an Antiproton Collector for the Antiproton Accumulator, edited by E.J.N. Wilson, CERN 83-10.

100. Proposal to improve the performance of the UA2 detector, CERN/SPSC 84-30, SPSC/P93 Add. 2.

101. Technical report on the design of a new combined electromagnetic/hadronic calorimeter for UA1, CERN/SPSC 84-72, SPSC/P92 Add. 5.

102. H. Wahl, Acta Physica Austriaca, Suppl. XXV, 399-487 (1983).

103. J. Ellis, Proc. 4th Topical Workshop on $p\bar{p}$ collider physics, Bern, 1984; CERN EP 84-09.